INSTITUTO TECNOLÓGICO Y DE ESTUDIOS
SUPERIORES DE MONTERREY

DEPARTMENT OF CHEMISTRY

ab initio BASED GRAND CANONICAL MONTE-CARLO SIMULATIONS OF CH_4 UPTAKE IN COVALENT ORGANIC FRAMEWORKS (COFs)

BY

JOSÉ LUIS MENDOZA-CORTÉS

SUBMITTED TO THE DEPARTMENT OF CHEMISTRY IN PART
FULLFILMENT OF THE REQUIREMENTS FOR THE
B. S. DEGREE IN CHEMISTRY

MONTERREY, N.L. MAY 2008

ab initio BASED GRAND CANONICAL MONTE-CARLO SIMULATIONS OF CH_4 UPTAKE IN COVALENT ORGANIC FRAMEWORKS (COFs)

BY

JOSÉ LUIS MENDOZA-CORTÉS

IT HAS BEEN APPROVED
MAY 2008

EVALUATION COMMITTEE:

Dr. William A. Goddard, *Advisor* California Institute of Technology	Dr. Omar M. Yaghi, *Advisor* University of California,Los Angeles
Dr. Marcelo Videa Vargas, *Advisor* Tecnolólogico de Monterrey	Dr. Hugo Alarcón, *Committee* Tecnolólogico de Monterrey
M.S. María A. de la Fuente, *Committee* Tecnolólogico de Monterrey	Dr. Bernard J. Micheli, *Committee* Tecnolólogico de Monterrey

ACCEPTED:

Dr. Marcelo Videa Vargas
Head, B. S. in Chemistry

Dr.Omar Yague Murillo
Chair of Chemistry Department

ABSTRACT

Alternatives routes towards new energies sources have become a main stream research worldwide. Methane has the potential to become a future fuel, however there have been longstanding problems related to transport and storage making it not an economically viable path. Attempts to overcome these issues include conversion to methanol, better compression techniques and sorption into porous materials. The latter is of special interest because of the recent discovering of new class of materials called Covalent Organic Frameworks (COF) that are: tailored materials, highly crystalline, have a high surface area ($\geq$2000 m^2/g) with a high pore volume and are made of just light atoms (C, Si, B,O and H). These properties allowed COFs to have the lowest crystalline densities among solid state materials with promising properties for storage. In order to investigate CH_4 sorption phenomena in COF an ab initio study was performed. Accurate second order Møller–Plesset perturbation theory (MP2) calculations were executed using doubly–polarized valence quadruple–ζ (QZVPP) basis sets in order to develop the correct force fields (FFs) between CH_4 and COF structure as well as CH_4 and CH_4. With the developed FFs, statistical mechanics concepts were implemented in a Grand Canonical Monte Carlo algorithm to simulate methane sorption in COFs. The approach was also tested comparing the densities of methane obtained by simulation with experimental ones at various pressures. Also experimental data for COF-5 and COF-8 were well reproduced with this theoretical approach. From this validation the method was extended to predict methane uptake in COF-1, COF-6, COF-8, COF-10, COF-102, COF-103, COF-105, COF-108 and COF-300. COF-1 is predicted to reach Department of Energy of United States of America target for methane storage in porous solids of 180 v(STP)/v. Using reticular chemistry new hypothetical structures are proposed to be synthesized, which are: COF-28, COF-300 and COF350.

ACKNOWLEDGMENTS

To every teacher, for showing me the Socratic though.

Thanks to Professor Omar M. Yaghi for believing in this project and for believing in me, a former student.

Thanks to Professor Goddard for supporting this idea and for being so enthusiastic about it.

Thanks to Dr. Han (CALTECH) and Dr. Furukawa (UCLA) for helping me with discussions.

To Professor Javier Rivas for supporting this work in an indirect way trough the Xorge A. Dominguez Fellowship. Also to every contributor to this fund.

My special thanks to Consejo Nacional de Ciencia y Tecnología (CONACyT) for supporting me during my entire career trough a scholarship.

Thanks to Snyder Foundation for a summer internship at University of Illinois at Urbana-Champaign in 2005

I am thankful to Roberto Rocca Foundation for its scholarship.

My exceptional thanks to Fraternidad Ricardo Guajardo for its scholarship, without I would not be able to live in Monterrey. Thank you for the housing, work and food.

Special thanks to scholarship department from ITESM for helping during my entire career.

Thanks to Philanthropic scholarship from ITESM for two years of support.

Thanks to Professor Becerril for allowing having my first contact with this fabulous subject called chemistry.

Thanks to the people of México for paying with their taxes for my excellent education.

Most of all, thanks to my Mom for being an example and teaching me all what I know about life.

DEDICATORY

To Azucena Artemisa Cortés Gaspar, my Mother

For giving me her genes and her courage to go for my goals

Thanks mom for guiding me in this so interesting path called life

Contents

List of Tables

List of Figures

Chapter 1

Introduction

The synthesis of porous solids has evolved into one of the most active area of research in chemistry and materials science because of the high performance applications, such as absorbents [1], catalysts [2], separator of gas mixtures [3], in which these materials play a key role. The best example is the use of zeolites for the cracking oil in the petrochemical industry. The new microporous and mesoporous materials have been successfully synthesized by solvent-surfactant method [4] solvo-thermal method [5] and by solvent diffusion [6]. However with current synthetic approaches it remains difficult, mostly impossible, to predict the crystal structure of the resulting crystalline solids [7]. The syntheses of porous solids with a predetermined crystalline structure are difficult due to the large number of possible periodic structures. A proposed solution to overcome this problem is the Reticular Chemistry where the use of secondary building units is employed to direct the assembly of ordered frameworks [8]. This approach has lead to the discovery of new families of materials which have been called Metal-Organic Frameworks (MOF), Covalent Organic Frameworks (COF) and Zeolitic Imadizolate Frameworks (ZIF). These materials are very thermally stable ($\geq$ 700 K), with unusual surface areas of 2500 m^2/g or larger [9], and highly symmetrical. A method that allows the prediction of the most probable crystal to be formed would allow scientists to design their target compound with specifically desired properties. The sorption properties are the most desirable characteristics to predict since the interaction of the structure with the gas or liquid determines applications such as separation, adsorption and catalyst activity [10].

The design of a general method from first principles where periodical structures and their interaction with methane are predicted, is the main objective of this work. Methane has been selected because it has the potential to become an essential fuel for the coming years, however there have been longstanding problems related to transport and storage making this route not economically viable. Attempts to overcome these issues include conversion to methanol, better compression techniques and sorption into porous materials. The latter is of special interest because of the very recent discovering of new class of materials called Covalent Organic Frameworks (COF) that are: tailored materials, highly crystalline, have a high surface area (m^2/g) with a high

pore volume and are made of just light atoms (C, Si, B,O and H). These properties allowed COFs to have the lowest crystalline densities among solid state materials and promising properties for storage. Using modern computational methods: ab initio (Second order Møller–Plesset perturbation theory, MP2), Density Functional Theory (DFT) and Molecular Mechanics for calculating the energy of the frameworks combined with propositions of theoretical principles of reticular chemistry will be discussed in the present effort. The trends observed will be analyzed and tested and the prediction of new structures will be attempted.

In order to investigate CH_4 sorption phenomena in COF an ab initio study was first performed. Accurate MP2 were performed using QZVPP basis set in order to develop the correct force fields (FFs) between CH_4 and COF structure as well as CH_4 and CH_4. With the developed FFs, a Grand Canonical Monte Carlo was used to simulate the methane adsorption in COFs. Stabilization studies were performed as well. The FFs was also tested comparing the densities of methane obtained by simulation with experimental ones at various pressures. Also methane uptake was performed experimentally in the cleanest COFs synthesized until now. The agreement found was exceptional. Quantum mechanics coupled to statistical mechanics, Reticular Chemistry and Sorption theories were used to model CH_4 uptake in several COF structures. In the following sections a meticulous description of methodology, results and prediction will be presented

1.1 Porous solids

Porous solids are a very interesting family of materials because of their capability to interact selectively with atoms, molecules and ions not only at their surfaces, but also through the bulk of the material. The distribution of size, shapes, volumes and chemical environment of the accesible spaces in porous materials are directly related to their properties to develop a desired function for a particular application. Porous materials are classified according to their size as: microporous (pore size from 0 to 20 nm), mesoporous (pore size from 20 to 50 nm) and macroporous (pore size above 50 nm). The importance of homogeneous porous makes important to create periodicity within the pore size, shape and volume. Ultimately these characteristics will determine specific applications. The most common materials with uniform micropores are zeolites.

1.2 Zeolites

Zeolites can discriminate between molecules on the basis of their size by selectively adsorbing the molecules that can fit in their uniform porous and avoid bigger molecules which pass through the material. In this case porous are of the same size, shapes,

volumes and chemical environment are crucial to the quality of the application. The most important applications of zeolites include ion exchange, separations, catalysis and as molecular sieves [11]. Zeolites are widely used as catalysts in industry, being extremely successful as catalyst for the oil refining, petrochemistry, and organic synthesis in the production of fine chemicals. The reason of this success due to the following features [12]: 1) They have a high surface area (1000 m2/g) and adsorption capacity. 2) The adsorption properties of zeolites can be modified and controlled changing from hydrophobic to hydrophilic type materials. 3) Active sites can be generated inside the framework and their strength and concentration can be designed for particular applications. 4) The well characterized channels and pores make the guest molecules to interact in a homogeneous fashion through all the framework; this generates a constant electric field and a specific confinement that it is responsible for tailored applications. 5) Finally but not less important is the fact that their periodic channels are responsible for shape selectivity, for instance when a catalytic process is being done, undesired side reactions are not possible because of this selection process. Then it is accepted that these specific and outstanding applications are due to their permanent porosity and the homogeneity of their pores.

These are some of the reasons why new materials with permanent porosity and highly crystalline are searched by materials scientist and chemists. Because of these characteristic features a general methodology to design the desired material is of remarkable importance. Part of our proposed solution to make predictions is the use of the Reticular Chemistry to develop periodical porous structures through one successfully family called Covalent Organic Frameworks.

1.3 Reticular Chemistry

Reticular Chemistry is defined as the construction of extended molecular structures directed by Secondary Building Units (SBU) in a predetermined structure. The SBU can be organic (molecules), inorganic (clusters) or hybrids (organic-inorganic). In Figure 1.1 some examples of SBU can be seen. The success of the application of this units has yield to build many extended solids and discrete polyhedra [8].

The main principle behind this theory is that using SBUs in the nodes of the most probable extended networks the most stable structure will be formed, providing a methodology for what is called rational design. This process skips the laborious simulation of finding the crystal structure from starting materials. So all the predictability remains in the calculations of the lattice energies and if two or more structures are possible then the lattice energy of each will determine the most thermodynamically favorable. Furthermore kinetic products can be found and polymorphs can be predicted based on their relative energy with respect to the most stable framework. The Figure 1.1 shows the concept of SBU, which can be found in inorganic and organic compounds. Some organics, inorganic or hybrids molecules are suitable

to be abstracted to a geometrical form, where the point of extension is a functional directing group. The molecules usually have to be rigid so the geometry does not change during the process of growing the extended structure and the final state can be *predicted*. The application of this approach has lead to the discovery of new families that are permanent porous and crystalline, among these families are Metal Organic Frameworks (MOF), Metal-Organic Polyhedral (MOP), Covalent Organic Frameworks (COF) and Zeolitic Imidazolate Frameworks (ZIF).

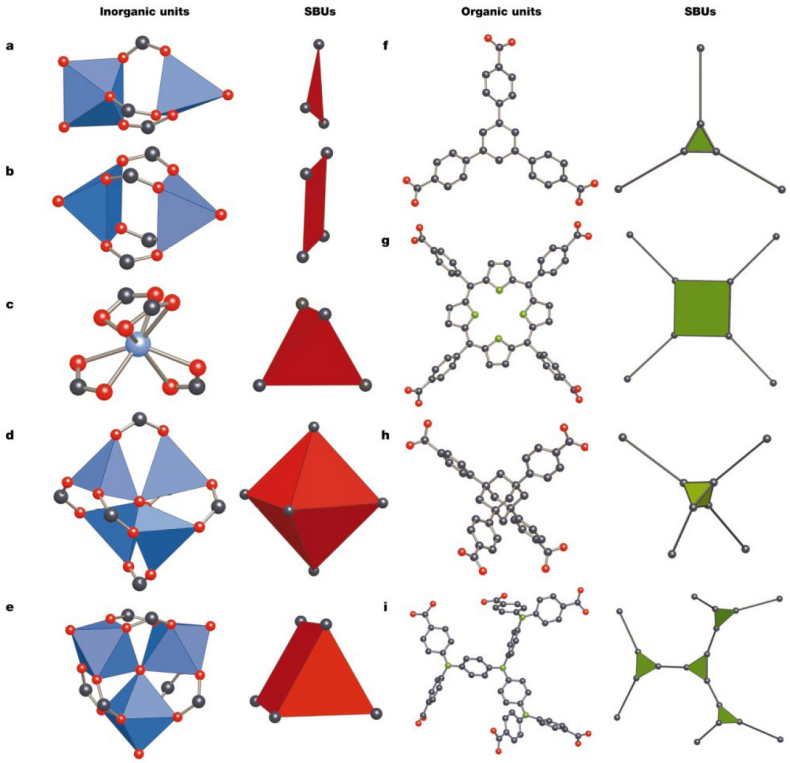

Figure 1.1: Secondary Building Unit, adapted from [8]

1.4 Covalent Organic Frameworks

In order to understand the development of the so called COFs it is important to understand graphite structure and properties. Graphite is a material formed just of C atoms, every atom bonded to three other C atoms, every atom with a sp^2 hybridization. Graphite is called a quasi-crystalline material, even though that the term locally crystalline is better applied. Graphite gives a powder X-Ray diffraction (PXRD) that resembles a bi-dimensional structure that has periodicity (crystallinity) with alternates layers ABABAB... where every layer is made of millions of hexagonal rings joined with C-C covalent bonds (Figure 1.2. This allotropic form of Carbon is an absorbent but it is not porous, this is because the gases are stored between layers. The layers are joined by π-σ attraction rather than a π-π electronic interaction which

leads to favorable interactions [13], thus in graphite there are not pores. Graphite is usually idealized as having the structures shown in 1.2. However, this structure is locally valid, which means that this graphite structure is a good description at microscopic level. The best surface areas achieved for graphitic porous carbon are $\approx$ 2400 m^2/g

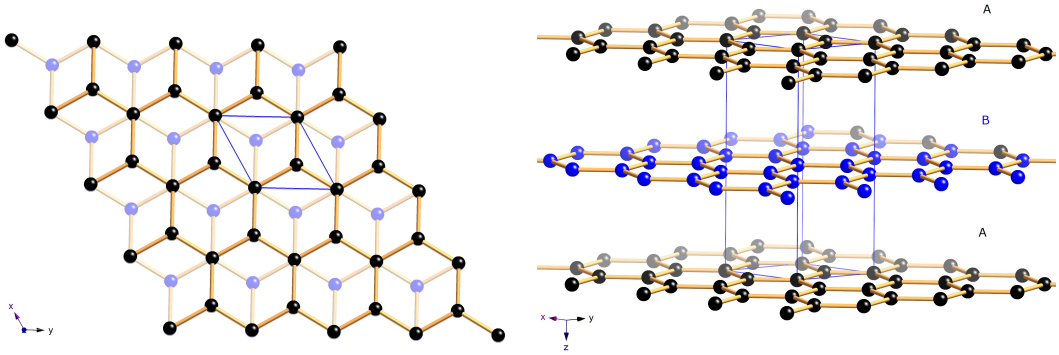

(a) Graphite structure (b) ABABABA layers of graphite

Figure 1.2: Ideal Graphite Structure

There have been numerous attempts to imitate this crystalline structure using light atoms such as C, B, O, N and H. Also these endeavors were oriented to get real porous materials where molecules can be placed. The most representative example is the family polymers of intrinsic porosity (PIM). These materials used the well know chemistry of polymers to attain 3D dimensional structure that are porous and almost crystalline. PIM synthesized so far have porosity in the structure but they are not crystalline even at the microscopic level. The accepted structures resemble those shown in Figure 1.3. It can be inferred that PIM are not suitable to be characterized nor with PXRD nor single crystal X-Ray. Then structures shown in Figure 1.3 are arguable but they are acceptable in some sense, because the sorption studies and physical properties that a macromolecule is presented. Physical properties used to characterized these materials are density, hardness, melting point and the results do not say anything about the structures. This is the main downside of PIM: the unknown structure, even tough their surface areas are unquestionable ($\approx$ 1000 m^2/g).

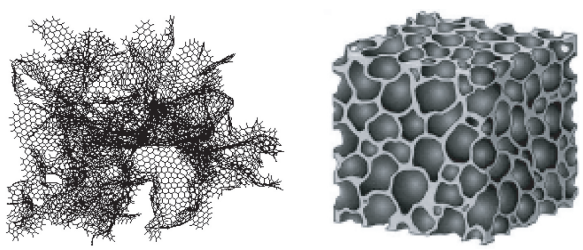

(a) 2D-PIM (b) 3D-PIM

Figure 1.3: Ideal structures of known PIM

The most successful approach to attain permanent porous materials with known chemical structures and made of light elements created the Covalent Organic Frameworks (COF). This approach attacks this problem generating the thermodynamically most stable structure trough formation of reversible covalent bonds. The microscopy reversibility of the crystallization process was the key for synthesizing the first members of these materials. These are called COF-1 and COF-5 (Figure 1.4)which are made entirely of light elements (H, B, C, N and O). COF-1 and COF-5 are 2D structures (the structure is repeated periodically in two directions) with homogeneous pore size of 0.7 to 2.7 nm and they are thermally stable (up to 600 °C). Furthermore these materials have permanent porosity with an exceptional BET surface area of 711 m^2/g(COF-1) and 1590 m^2/g (COF-5)[14]. Another important characteristic of this materials is that they were synthesized under mild conditions (120-150 °C). The main reason of this crystallization was the use of *dynamic covalent chemistry* were the reversibility of bond formation is crucial to form the most stable thermodynamic product [15].

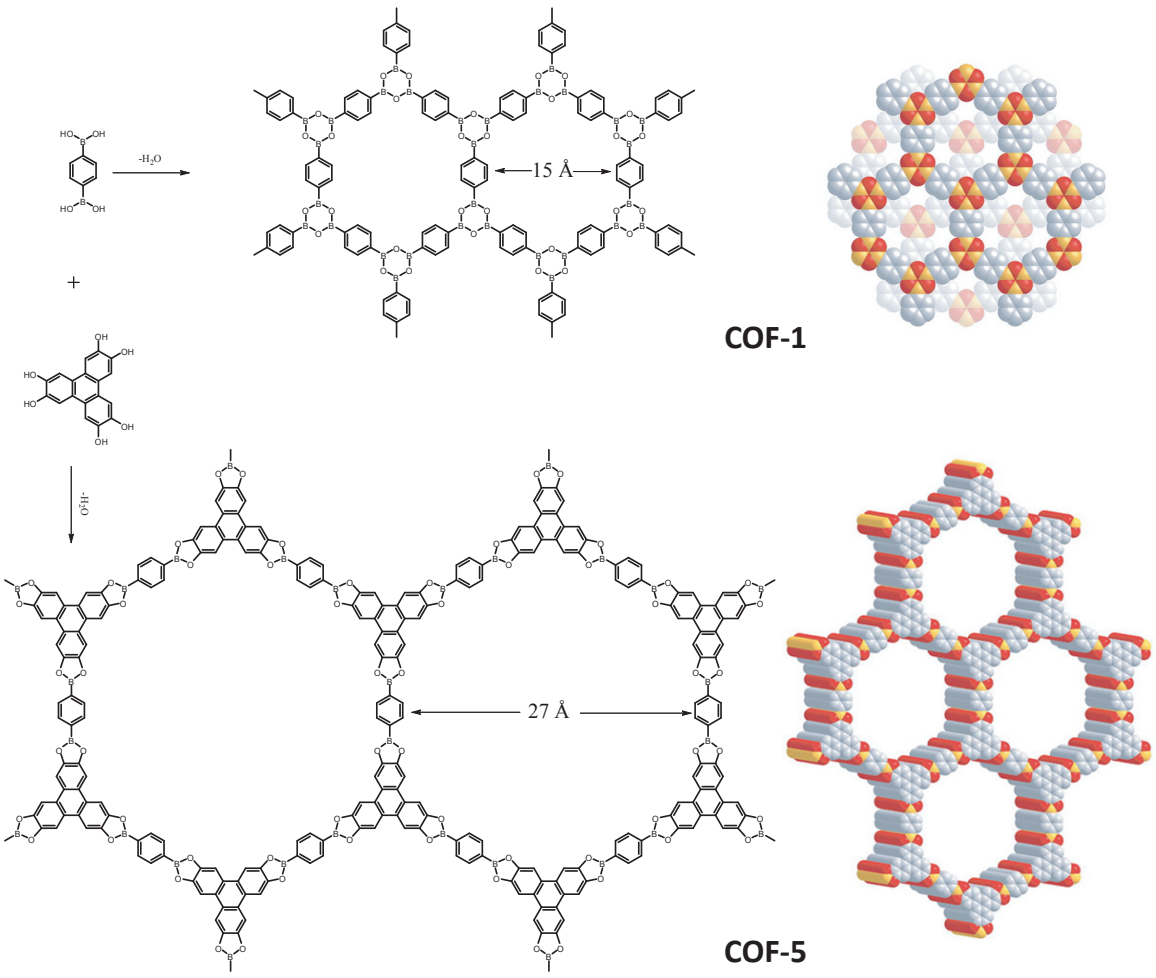

Figure 1.4: 2D-COFs, adapted from [14]

A similar approach was used to synthesize 3D structures joined by the thermo-

dynamic strength of covalent bonds. The number of possible structures that may result from linking specific building-unit geometries into 3D extended structures is essentially infinite and it complicates their synthesis by design. However these complications can be overcame by judiciously choosing the building blocks and using reversible condensation reactions [16]. In principle, there are an infinite number of possible nets that may result from linking tetrahedra with triangles. However, in this work it was shown again that most symmetric nets are the most likely to result in an unbiased system and that those with just one kind of link will be preferred and are thus the best to target [8]. In linking tetrahedral and triangular building blocks, there are only two known nets meeting the above criteria designated by the symbols **ctn** (Figure 1.5) and **bor** (Figure 1.6)[17].

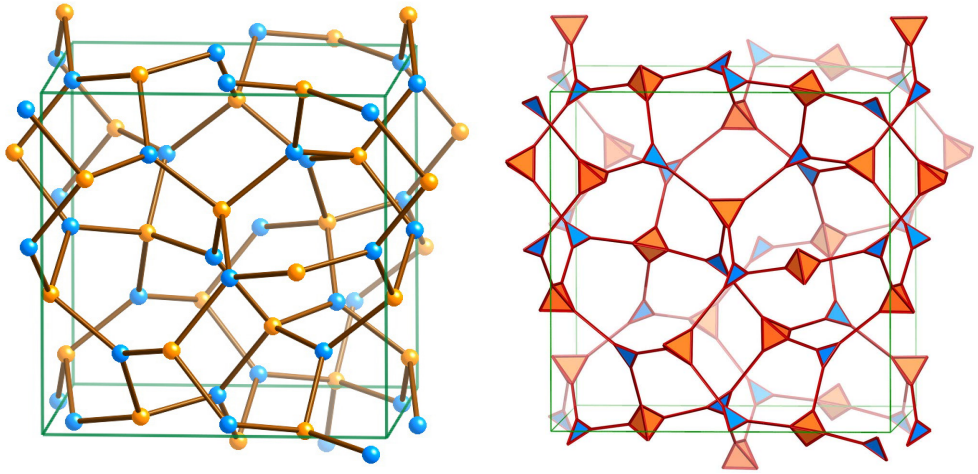

(a) ctn net (b) ctn augmented

Figure 1.5: **ctn**

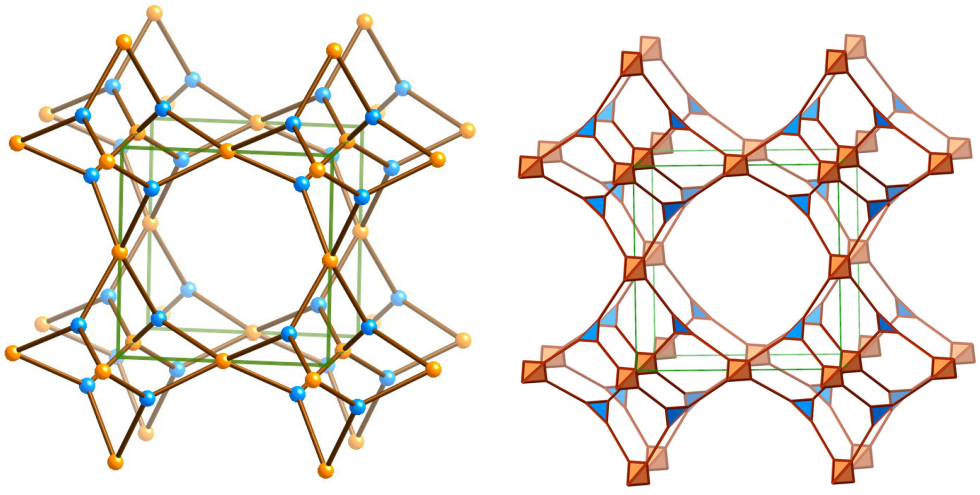

(a) bor net (b) bor augmented

Figure 1.6: **bor**

The nodes of the nets were thus replaced by the molecular building units with tetrahedral and triangular shapes. The use of rigid, planar triangular chemical units, such as B_3O_3 rings, requires that rotational freedom exist at the tetrahedral nodes for the 3D structures **ctn** and **bor** to form. Modelling was used to build the "blueprints" for synthesis of COFs based on **ctn** and **bor** nets by fitting molecular building blocks on the tetrahedral nodes and by fitting the triangular unit and the B_3O_3 ring on the triangular nodes of these nets adhering to their respective cubic space group symmetries: $I\bar{4}3d$ **ctn** and $P\bar{4}3m$ **bor**. These nets can be represented in a tilling fashion, using Delaney symbols, they are shown graphically in Figure 1.10. Energy minimization by means of force-field calculations was performed to produce the models in which all bond lengths and angles were found to have chemically reasonable values.

The new materials built with this reasoning were the first 3D-Covalent Organic Frameworks. These materials have been named COF-102 (Figure 1.11), COF-103 (Figure 1.11), COF-105 (Figure 1.12) and COF-108 (Figure 1.13), of which, COF-103 and COF-105 were synthesized by the author of this thesis. They have high thermal stability (400 to 500 °C), COF-102 exhibits a BET surface area of 3472 m^2/g and COF-103 a BET surface area of 4210 m^2/g; the highest know for a porous, crystalline solid linked by covalent bonds. Also COF-108 has the lowest density of any crystalline materials, 0.17 g/cm^3. In the COFs with **ctn** topology, the center of the largest cavity in COF-102, COF-103, and COF-105 is 5.66, 5.98, and 10.37 Å, respectively, from the nearest atoms (H). If we allow for a van der Waals radius of 1.2 Å for H, spheres of diameter 8.9, 9.6, and 18.3 Å, respectively, are available in these three COFs [16]. However, the pores in these materials are far from spherical, and we expect the effective pore size to be somewhat larger. COF-108 has two cavities, and the atoms closest to the center are C atoms at 9.34 and 15.46 Å. If we allow for a van der Waals radius of 1.7 Åfor C, these cavities can accommodate spheres of 15.2 and 29.6 Å, respectively. The extraordinary low densities COFs are summarized in Table 1.1. The extremely low values of COFs are obvious if they are compared to diamond.

Table 1.1: Densities of COFs

Compound	Density / (g/cm^3)
COF-1	0.91
COF-5	0.58
MOF-5	0.59
COF-102	0.41
COF-103	0.38
COF-105	0.18
COF-108	0.17
MOF-177	0.42
Diamond	3.50

1.5 Tillings

Data for tilings are for the so-called *natural* tilings. The D-symbols are what were originally called Delaney symbols by Dress and Delaney-Dress symbols by subsequent workers. Regular nets are defined independently of tilings but are the only structures with natural tilings that have one kind of vertex, edge, face and tile [18].

The four main topologies that are used in the present work are: Boron nitride (**bnn**), Graphite (**gra**), Carbon nitride (**ctn**), Boracite (**ctn**). The main characteristics of these topologies are presented in Table 1.2. COF-1 has **gra** topology. COF-5, COF-6, COF-8, COF-10 and COF-28 have **bnn** topology (See Figure 1.7). COF-102, COF-103, COF-105 and COF-350 have **ctn** topology. COF-108 and COF-300 have **bor** topology.

Table 1.2: Topologies used

Topology	tiling	vertices	edges	faces	tiles	D-symbol
bnn	[4^6.6^2]	1	2	2	1	3
gra	[6^4]	2	2	2	1	8
ctn	[8^3] (SD: (3[8^4] + 4[8^3])	2	1	2	2	40
bor	[6^4] + [6^4.8^6]	2	1	2	2	8

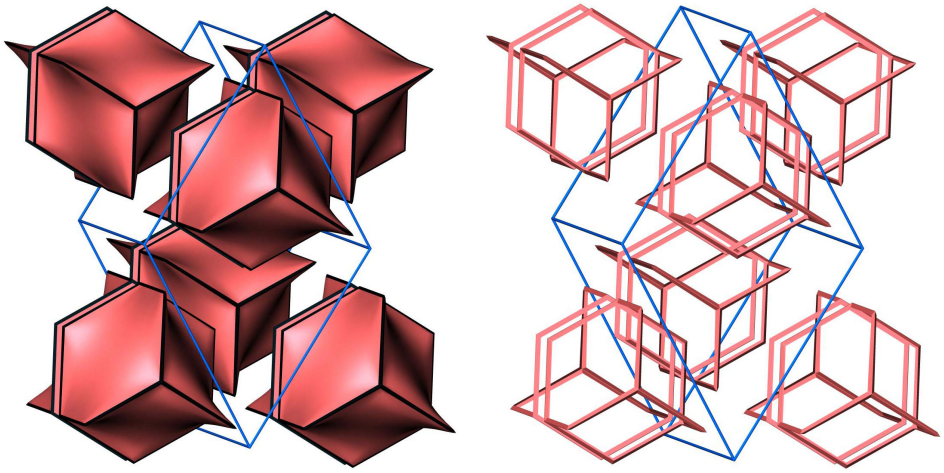

(a) Faced Tillings **gra** (b) Tillings **gra**

Figure 1.7: **gra**

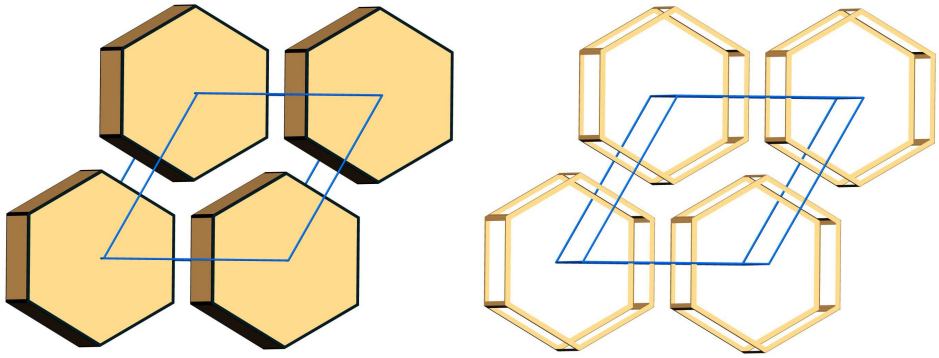

(a) Faced Tillings **bnn** (b) Tillings **bnn**

Figure 1.8: **bnn**

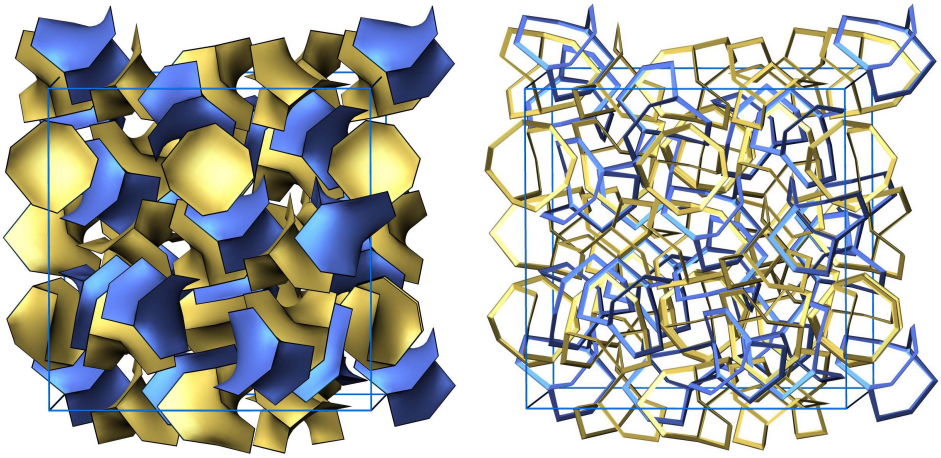

(a) Faced Tillings **ctn** (b) Tillings **ctn**

Figure 1.9: **ctn**

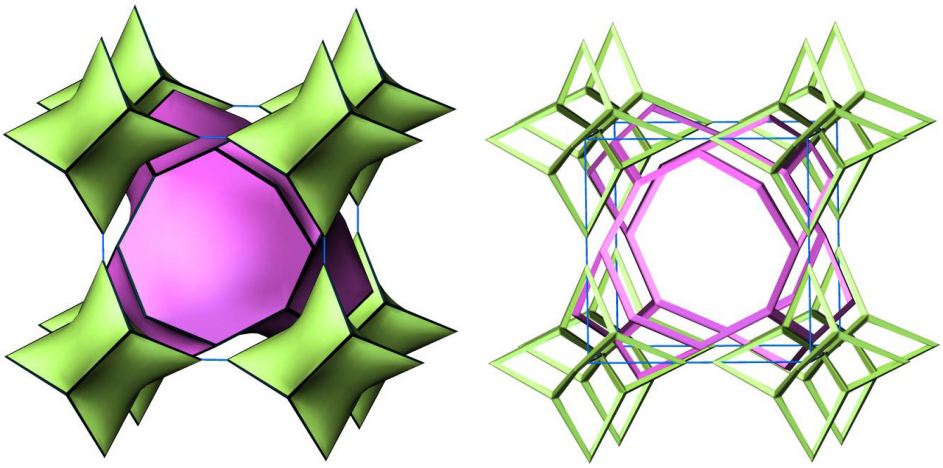

(a) Faced Tillings **bor** (b) Tillings **bor**

Figure 1.10: **bor**

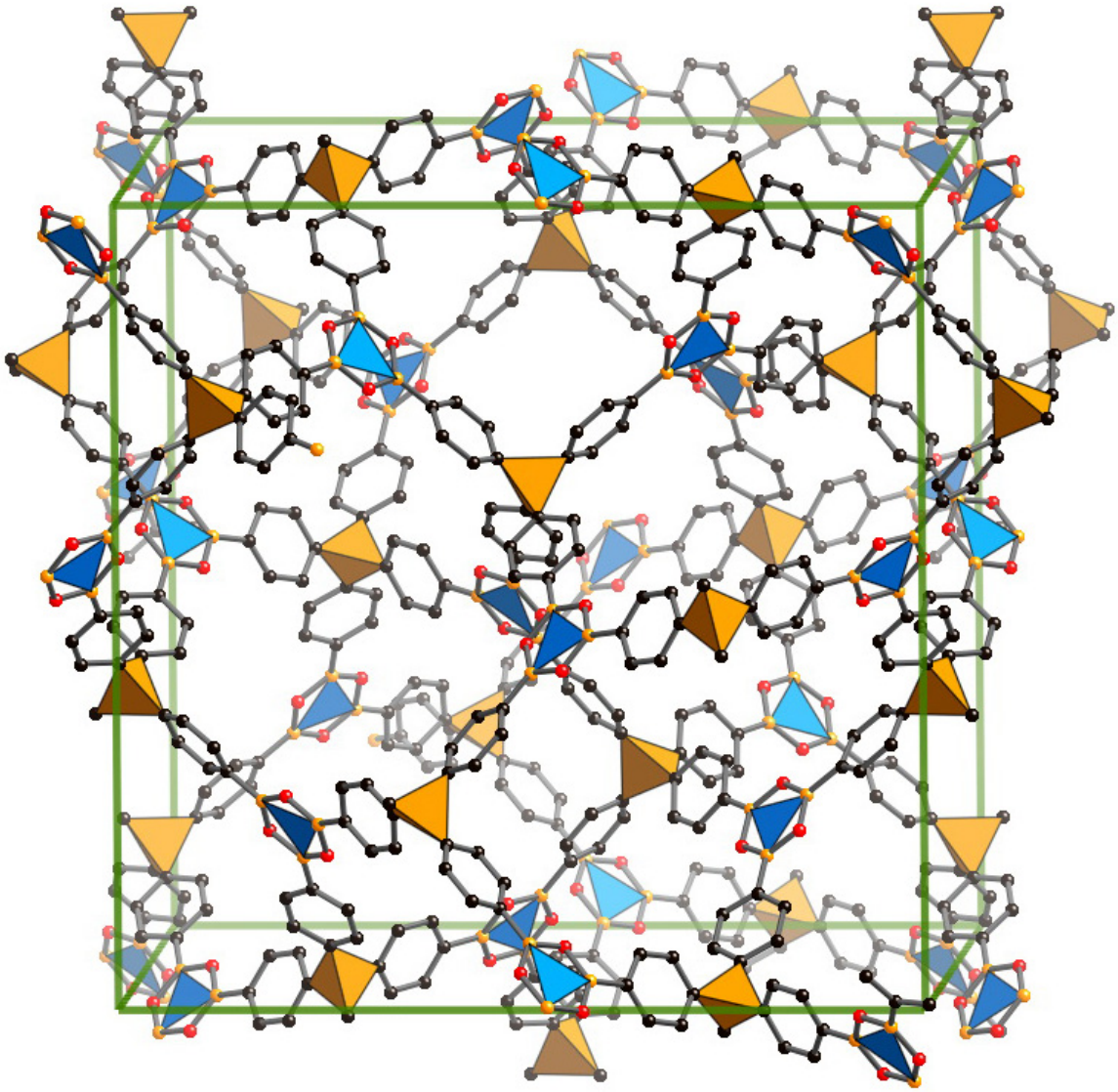

Figure 1.11: COF-102 and COF103

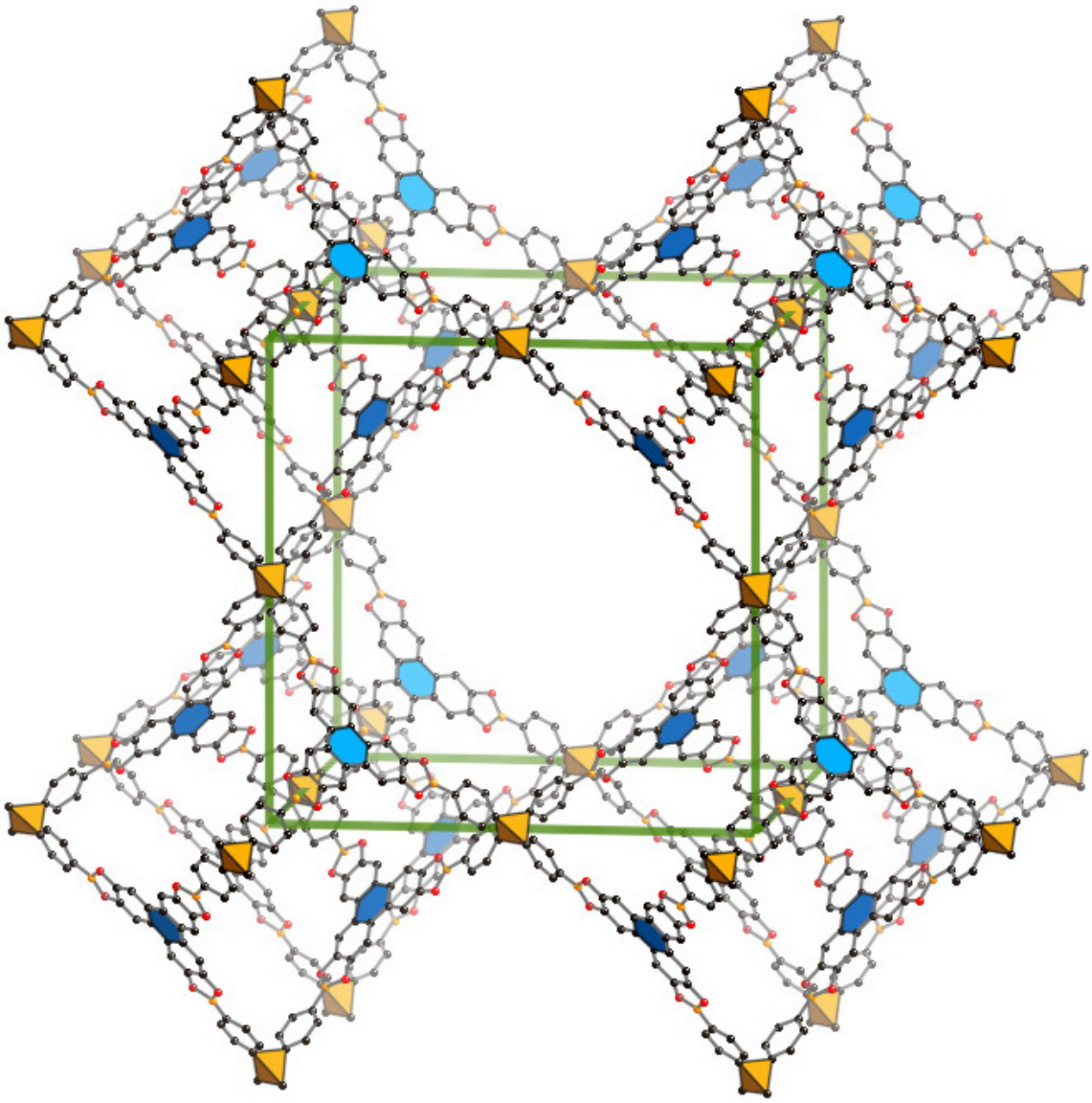

Figure 1.12: COF-105

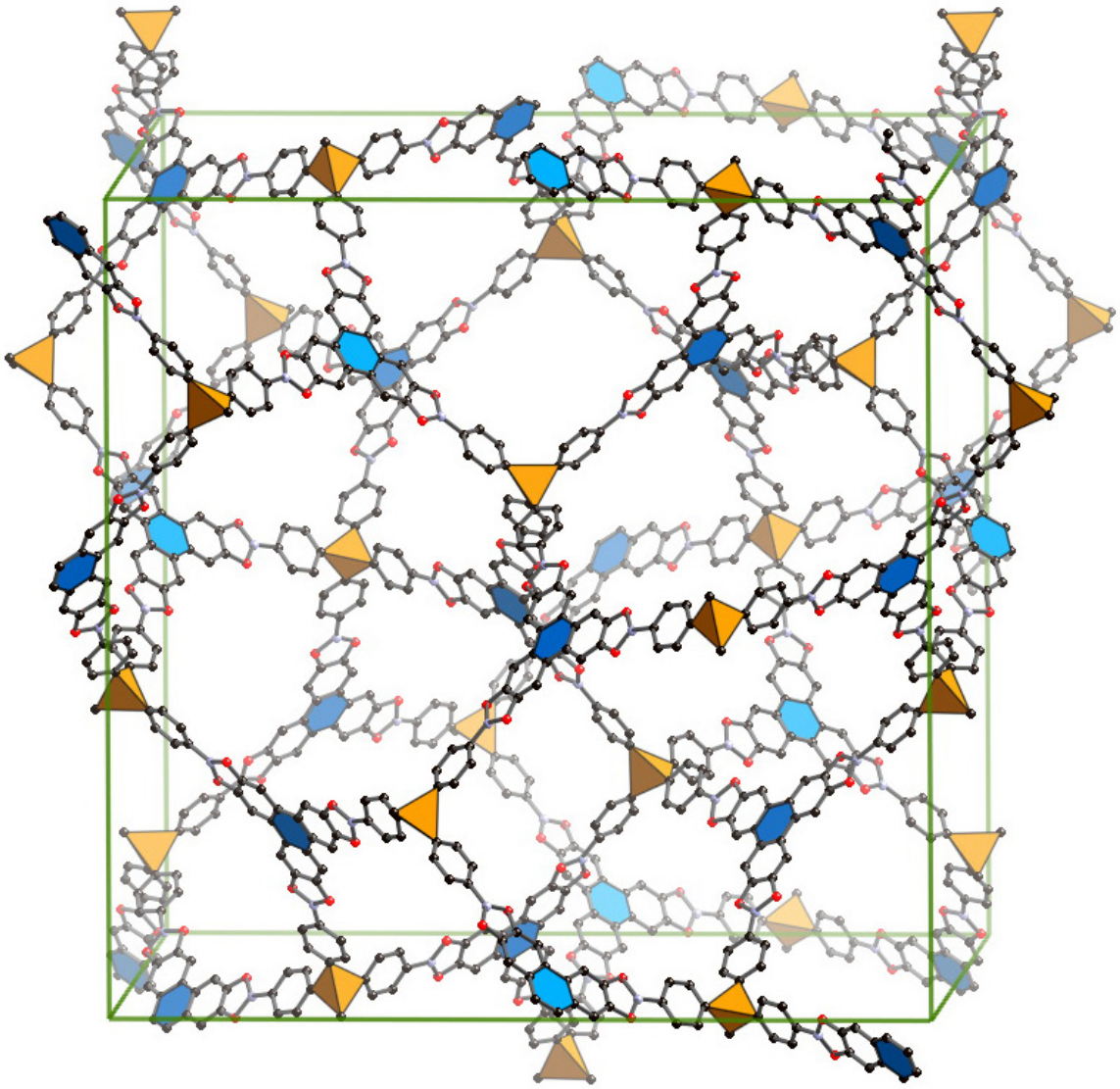

Figure 1.13: COF-108

Chapter 2

Methodology

Our coupling of quantum mechanics and statistical mechanics gives result in excellent agreement with experiments. In the following lines the essentials of our theoretical calculations is presented.

2.1 Quantum Mechanics

Resolution of the identity (**RI**) second order Møller–Plesset perturbation theory (RI-MP2) calculations (**RI-MP2**) [25][26] were implemented in the TURBOMOLE program [24]. All the geometries were optimized with the RI-MP2/QZVPP level of theory with frozen cores. Where QZVPP stands for the doubly-polarized valence quadruple–ζ basis sets [23]. Then single point energies were calculated using RI-MP2 with the quadruple zeta QZVPP basis set. The appropiate optimized auxiliary basis sets were assigned for all the calculations[23].

Second order Møller–Plesset Perturbation Theory (MP2) corrects errors introduced by the mean–field ansatz of the Hartree–Fock (HF) theory, the perturbation operator is just the difference of the exact and the HF Hamiltonian. In this approach the MP2 energy is [24]:

$$E_{MP2} = \frac{1}{4} \sum_{iajb} \left[t_{ij}^{ab} \langle ij \| ab \rangle \right] \tag{2.1}$$

with the t–amplitudes

$$t_{ij}^{ab} = \frac{\langle ij \| ab \rangle}{\epsilon_i + \epsilon_j - \epsilon_a - \epsilon_b} \tag{2.2}$$

i and j denote occupied, a and b virtual orbitals, ϵ_p are the corresponding or-

bital energies, $\langle ij\|ab\rangle = \langle ij|ab\rangle - \langle ij|ba\rangle$ are four center two electron integrals in a commonly used notation.

MP2 gradients (necessary for optimisation of structure parameters at the MP2 level) are calculated as analytical derivatives of the MP2 energy with respect to nuclear coordinates; calulation of these derivatives also yields the first order perturbed wave function, expressed as "MP2 density matrix", in analogy to the HF density matrix. MP2 corrections of properties like electric moments or atomic populations are obtained in the same way as for the HF level, the HF density matrix is just replaced by the MP2 density matrix.

2.2 Basis Set Superposition Error(BSSE) correction with the counterpoise(CP) Method

The Basis Set Superposition Error BSSE was corrected using the Countepoise Method CP [20] for each of model 3.1. The CP method calculates each of the units with the basis functions of the other (but without the nuclei or electrons), using the so called *ghost orbitals* [21]. The CP method in the current systems can be stated as:

$$E^{CP}_{interaction} = E_{super} - \sum_{i=1}^{n} E_{m^i_{opt}} + \sum_{i=1}^{n} (E_{m^i_f} - E_{m^{i*}_f}) \tag{2.3}$$

Where the E_{m^s} represent the energies of the individual monomers. The subscripts *opt* and f denote the individually optimized monomers and those frozen in their supermolecular geometries and the asterisk $(*)$ denotes monomers calculated with ghost orbitals.

2.3 Morse Type Potential

The general formula to obtained the Force Field Parameters is:

$$\boldsymbol{U}^{Morse}_{ij}(r_{ij}) = D\left\{e^{\alpha(1-\frac{r_{ij}}{r_0})} - 2e^{-\frac{\alpha}{2}(1-\frac{r_{ij}}{r_0})}\right\} \tag{2.4}$$

Where:

- D = Well depth
- r_0 = Equilibrium bond distance

- α = Force Constant

Where r_{ij} is the distance between the atoms, r_0 is the equilibrium bond distance, D De is the well depth (defined relative the dissociated atoms), and a controls the 'width' of the potential. The dissociation energy of the bond can be calculated by subtracting the zero point energy E_0 from the depth of the well. The force constant of the bond can be found by taking the second derivative of the potential energy function, from which it can be shown that the parameter, α, is

$$a = \sqrt{\frac{K_f}{2 \cdot D}} \tag{2.5}$$

where:

- K_f is the force constant at the minimum of the well

2.4 Statistical Mechanics: Grand Canonical Monte Carlo

In the Grand Canonical ensemble the independent variables are: chemical potential (μ), volume (V) and temperature (T). Here the volume belongs to the cavity of the porous material. First some molecules are placed in the cavity fo the structure, each atoms has a position vector associate with it in a coordinate system. Four events are taking into account in the simulation: translation, rotation, creation and anhilation. The code implemented is based in a standard algorithm [27][28].

In a translation event, the new components of the position vector, **R** are given by:

$$\begin{aligned} R_x^{new} &= R_x^{old} + \delta u \\ R_y^{new} &= R_y^{old} + \delta v \\ R_z^{new} &= R_z^{old} + \delta w \end{aligned}$$

where u, v and w are random numbers localized between - 1 and 1, and δ is a constant.

The new orientation vector (event), **O**, is determined by:

$$\begin{aligned} O_x^{new} &= \frac{l}{2}\frac{u}{r} \\ O_y^{new} &= \frac{l}{2}\frac{v}{r} \\ O_z^{new} &= \frac{l}{2}\frac{w}{r} \end{aligned}$$

and,

$$r = \sqrt{u^2 + v^2 + w^2}$$

Where u, v and w are random numbers localized between - 1 and 1, and l is the bondlength. A decision is taken in order to accept or refuse the new configuration based on the probability, P_{move}

$$P_{move} = min[\exp(-\Delta U/kT); 1] \tag{2.6}$$

where

$$\Delta U = U_{new} - U_{old} \tag{2.7}$$

The second part of the simulation process of the GCMC is to add or remove a molecule [27][28]. These two events are generated at random with equal probability.

If the event addition is generated then the next step is the random generation of the position and the orientation of new molecule(s). The potential of this new configuration is calculated and it is accepted or refejected based on, P_{add}:

$$P_{add} = min\left[\frac{1}{N+1}\frac{PV}{kT}\exp(-\Delta U/kT); 1\right] \tag{2.8}$$

Here N is the number of molecules before the addition event is taken place, P is the pressure of the bulk gas, and V is the volume of the porous material cavity.

If the event annihilation is generated then the next step is deletion of a randomly chosen molecule of the gas phase. Once again the potential of the new configuration is calculated, and the event is accepted or rejected based on P_{anh}:

$$P_{anh} = min\left[\frac{NkT}{PV}\exp(-\Delta U/kT); 1\right] \tag{2.9}$$

Where N is the number of molecules before the subtraction. If the annihilation event is accepted, then the substraction is made permanent. If the subtraction is rejected, then the deleted molecule is returned to its old position.

Chapter 3

Quantum Mechanical calculations

3.1 CH_4–CH_4 interaction

In order to calculate the properties of the intereactions in CH_4–CH_4 four symmetries were studied. These symetries were found to be the most stable.

- ***C*$_{3v}$** 3.1.1
- ***C*$_{3v}$*-2*** 3.1.2
- ***D*$_{3d}$** 3.1.3
- ***D*$_{3h}$** 3.1.4

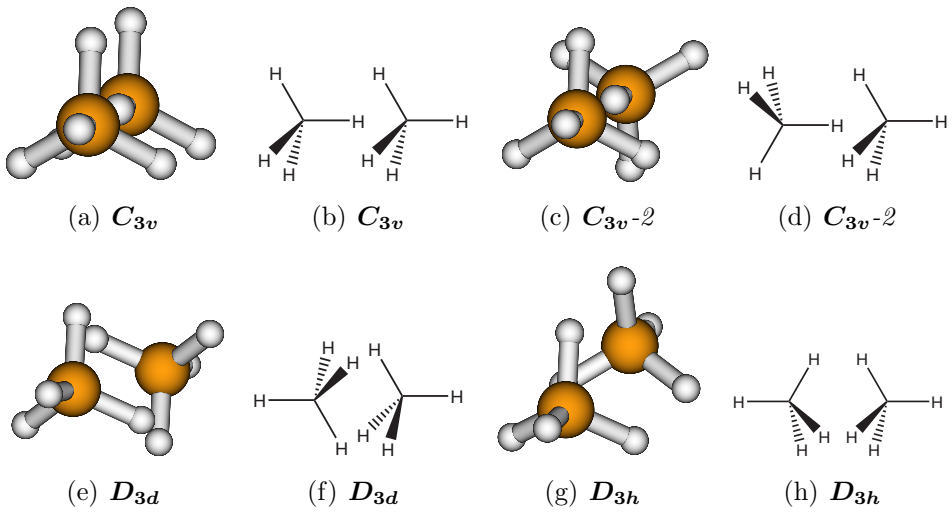

(a) ***C*$_{3v}$** (b) ***C*$_{3v}$** (c) ***C*$_{3v}$*-2*** (d) ***C*$_{3v}$*-2***

(e) ***D*$_{3d}$** (f) ***D*$_{3d}$** (g) ***D*$_{3h}$** (h) ***D*$_{3h}$**

Figure 3.1: The structures used to calculate the CH_4–CH_4 interaction

3.1.1 CH_4–CH_4 interaction with C_{3v} symmetry

For each structure the **IR-MP2** calculation method was applied, then the BSSE was corrected using the CP method 2.1. The structure used to perform this calculation is shown in Figure 3.2. The data is plotted in the Figure 3.3. The values obtained after normalization are shown in the Table 3.1

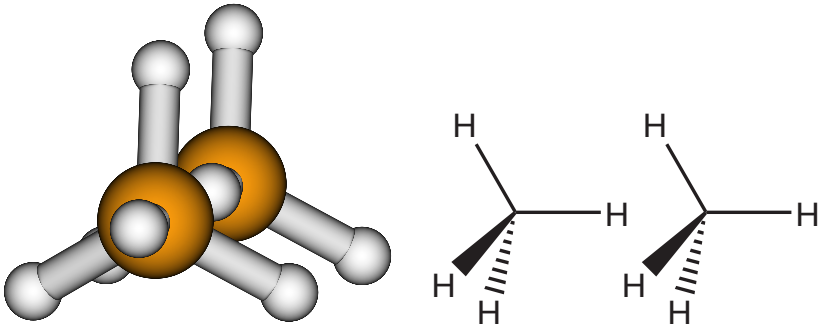

(a) $\boldsymbol{C_{3v}}$ (b) $\boldsymbol{C_{3v}}$

Figure 3.2: CH_4–CH_4 interaction with $\boldsymbol{C_{3v}}$ symmetry

Table 3.1: Energies of CH_4–CH_4 $\boldsymbol{C_{3v}}$ symmetry

$\mathbf{C\text{-}C}_{\text{Distance}}/(\text{Å})$	$\mathbf{E}_{\text{Not corrected}}/(\text{Kcal/mol})$	$\mathbf{E}^{\text{CP}}_{\text{corrected}}/(\text{Kcal/mol})$
3.600000	0.53052843752812	0.57452007530446
3.800000	0.12882247671223	0.15081558038946
3.900000	0.04618721470615	0.05936093416312
4.000000	0.00862165887520	0.01447516312328
4.100000	0.00000000000000	0.00000000000000
4.200000	0.00924154558015	0.00471468137766
4.300000	0.02887245606689	0.02070262826237
4.400000	0.05395980684989	0.03572982178230
4.600000	0.10885781235993	0.09366763825165
4.800842	0.15700086912693	0.13878895777816
5.000000	0.20364237214380	0.18311462418569
5.200000	0.23849908379634	0.21490236389218
5.400000	0.26582729653455	0.24225837323320
5.600000	0.28709140617866	0.26241575058521
5.800000	0.30362645714195	0.27795139414957
6.000000	0.31653475495841	0.29003040352109
6.600000	0.34098701408220	0.31258080817497

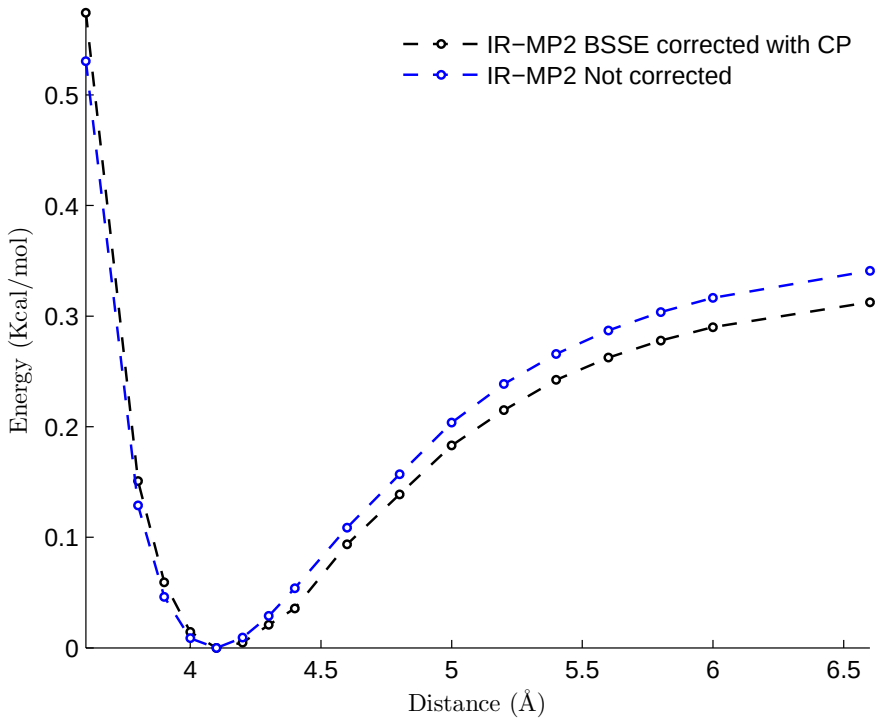

Figure 3.3: Energies of CH_4–CH_4 $\boldsymbol{C_{3v}}$ symmetry

3.1.2 CH_4–CH_4 interaction with C_{3v}-*2* symmetry

For each structure the **IR-MP2** calculation method was applied, then the BSSE was corrected using the *C*P method 2.1. The structure used to perform this calculation is shown in Figure 3.4. The data is plotted in the Figure 3.5. The values obtained after normalization are shown in the Table 3.2

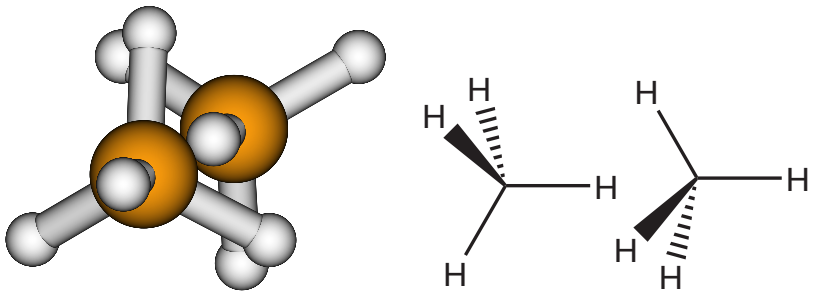

(a) $\boldsymbol{C_{3v}}$-*2* (b) $\boldsymbol{C_{3v}}$-*2*

Figure 3.4: CH_4–CH_4 interaction with $\boldsymbol{C_{3v}}$-*2* symmetry

Table 3.2: Energies of CH_4–CH_4 $\boldsymbol{C_{3v}}$-2 symmetry

$\mathbf{C\text{-}C}_{\text{Distance}}/(\text{Å})$	$\mathbf{E}_{\text{Not corrected}}/(\text{Kcal/mol})$	$\mathbf{E}^{\text{CP}}_{\text{corrected}}/(\text{Kcal/mol})$
3.60000	0.53308463159920	0.57653268839931
3.80000	0.13014945530449	0.15175314436056
3.90000	0.04697433637921	0.05995474005613
4.00000	0.00896703069157	0.01473596737560
4.10000	0.00000000000000	0.00000000000000
4.20000	0.00898250092723	0.00446525676671
4.30000	0.02842308270920	0.02042414181415
4.40000	0.05337507829972	0.04263228572381
4.60000	0.10812208564312	0.09737929306721
4.81432	0.16287032817490	0.14500179945389
5.00000	0.20288010723743	0.18298343874267
5.20000	0.23777839252580	0.21618862164542
5.40000	0.26518285983912	0.24229252143414
5.60000	0.28651729528065	0.26413388263245
5.80000	0.30312104040058	0.27824410612448
6.00000	0.31609139708598	0.29038685452179
6.60000	0.31609139708598	0.29038310358374

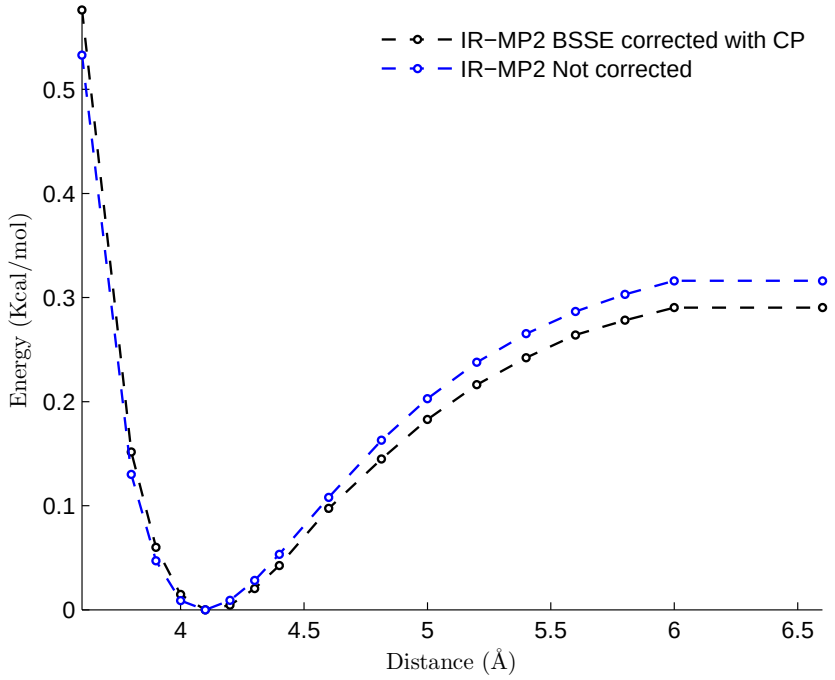

Figure 3.5: Energies of CH_4–CH_4 $\boldsymbol{C_{3v}}$-*2* symmetry

3.1.3 CH_4–CH_4 interaction with D_{3d} symmetry

For each structure the **IR-MP2** calculation method was applied, then the BSSE was corrected using the CP method 2.1. The structure used to perform this calculation is shown in Figure 3.6. The data is plotted in the Figure 3.7. The values obtained after normalization are shown in the Table 3.3

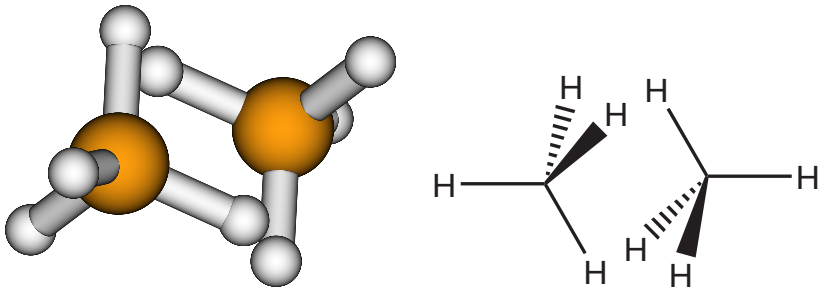

(a) $\boldsymbol{D_{3d}}$ (b) $\boldsymbol{D_{3d}}$

Figure 3.6: CH_4–CH_4 interaction with $\boldsymbol{D_{3d}}$ symmetry

Table 3.3: Energies of CH_4–CH_4 $\boldsymbol{D_{3d}}$ symmetry

C-C$_{\text{Distance}}$/(Å)	**E**$_{\text{Not corrected}}$/(Kcal/mol)	**E**$^{\text{CP}}_{\text{corrected}}$/(Kcal/mol)
2.60000	10.79096661054060	11.00357384236850
2.80000	4.74576235674613	4.75274577266464
3.00000	1.88507942527212	1.97681289587490
3.20000	0.62758728802874	0.67809388630849
3.40000	0.14020055909350	0.16423061175738
3.50000	0.04441514669452	0.05920572180912
3.60000	0.00439672984066	0.01138014575918
3.70000	0.00000000000000	0.00000000000000
3.80000	0.00439672978246	0.01137952346471
3.90000	0.04699998182332	0.03469090576255
3.98774	0.07799901218823	0.06109160034248
4.20000	0.15613792458316	0.13034775814595
4.40000	0.22139135053294	0.19052781974460
4.60000	0.27423634244042	0.24055903332555
4.80000	0.31574658382306	0.28028177196757
5.00000	0.34815807580890	0.31114023361079
5.20000	0.37347573599254	0.33488972045234
6.00000	0.43026045148145	0.38642259118205

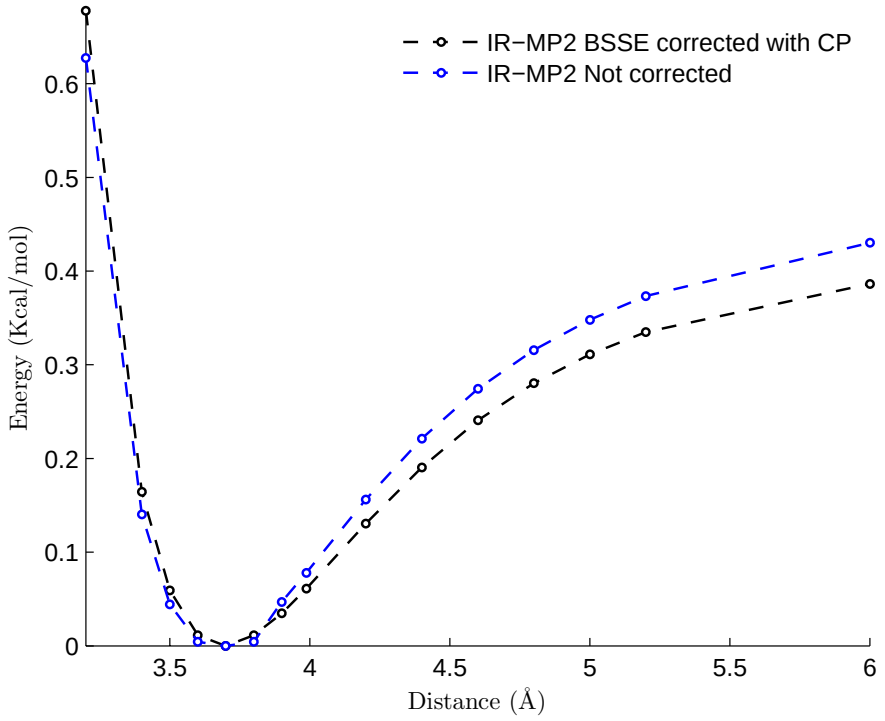

Figure 3.7: Energies of CH_4–CH_4 $\boldsymbol{D_{3d}}$ symmetry

3.1.4 CH_4–CH_4 interaction with D_{3h} symmetry

For each structure the **IR-MP2** calculation method was applied, then the BSSE was corrected using the CP method 2.1. The structure used to perform this calculation is shown in Figure 3.8. The data is plotted in the Figure 3.9. The values obtained after normalization are shown in the Table 3.4

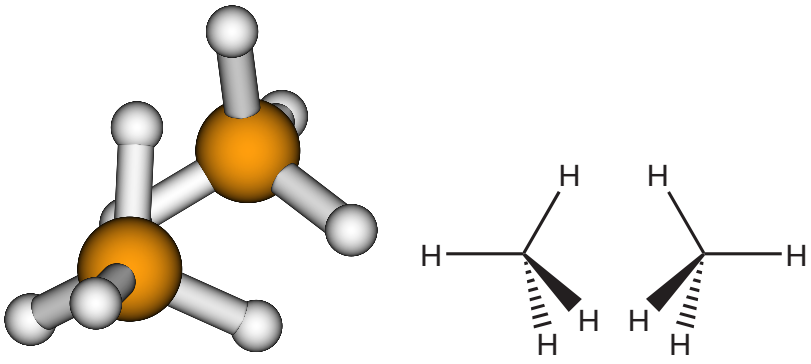

(a) $\boldsymbol{D_{3h}}$ (b) $\boldsymbol{D_{3h}}$

Figure 3.8: CH_4–CH_4 interaction with $\boldsymbol{D_{3h}}$ symmetry

Table 3.4: Energies of CH_4–CH_4 $\boldsymbol{D_{3h}}$ symmetry

C-C$_{\text{Distance}}$/(Å)	**E**$_{\text{Not corrected}}$/(Kcal/mol)	**E**$^{\text{CP}}_{\text{corrected}}$/(Kcal/mol)
2.40000	26.39133804863380	26.64950425412830
2.60000	12.40810450514980	12.58714311221770
2.80000	5.50813792921690	5.63128489050359
3.00000	2.23989803280710	2.33107906741134
3.20000	0.78556056413072	0.83328423239800
3.40000	0.20299195233383	0.23175237030227
3.60000	0.01867128079903	0.02759567247267
3.75821	0.00000000000000	0.00000000000000
4.00000	0.05456402576965	0.04345240426483
4.20000	0.11951088169008	0.10169480165496
4.40000	0.17988647555467	0.15783616805857
4.60000	0.22995386324328	0.20542978340382
4.80000	0.26979053125979	0.24357373763633
5.00000	0.30109060490941	0.27334642210190
5.80000	0.30108691564965	0.27334274721216

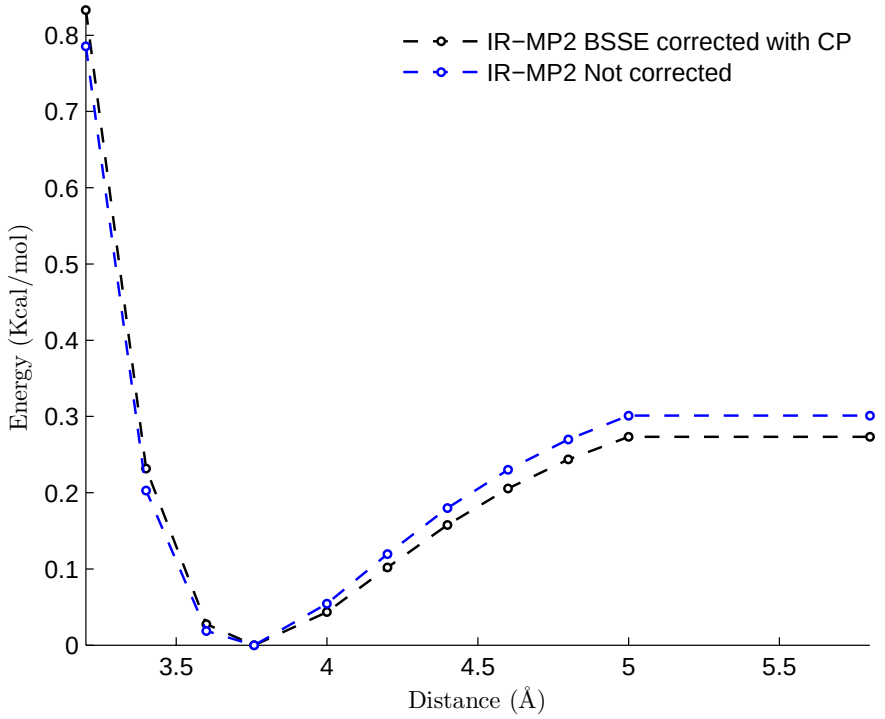

Figure 3.9: Energies of CH_4–CH_4 $\boldsymbol{D_{3h}}$ symmetry

3.1.5 Fitting Quantum Mechanics to a Force Field

The MP2 results were fitted into a Force Field with a Morse Type Potential equation 2.4. The four geometries (see Figure 3.1) were used to obtain the best fitting for these configurations. The parameters obtained are shown in Table 3.5. Energies of the Force Field against Quantum Mechanics results are shown in Figure 3.11 and in Figure 3.10

Table 3.5: Parameters from Fitting equation 2.4 in CH_4–CH_4

Term	**D**/(Kcal/mol)	$\mathbf{r_0}$/(Å)	$\boldsymbol{\alpha}$
C_{CH_4}—C_{CH_4}	0.07672	3.92295	12.6913
H_{CH_4}—H_{CH_4}	0.00321	3.1266	11.4255
C_{CH_4}—H_{CH_4}	0.05212	3.45922	11.01982

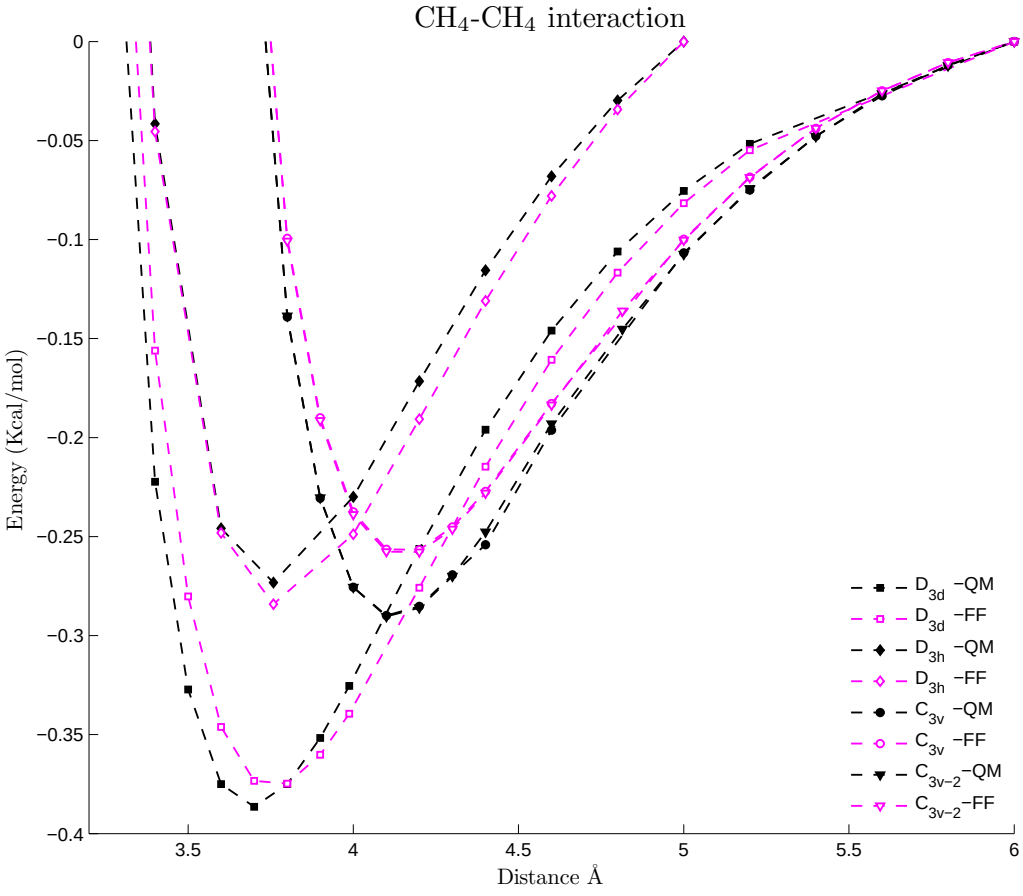

Figure 3.10: Force Field against MP2 results

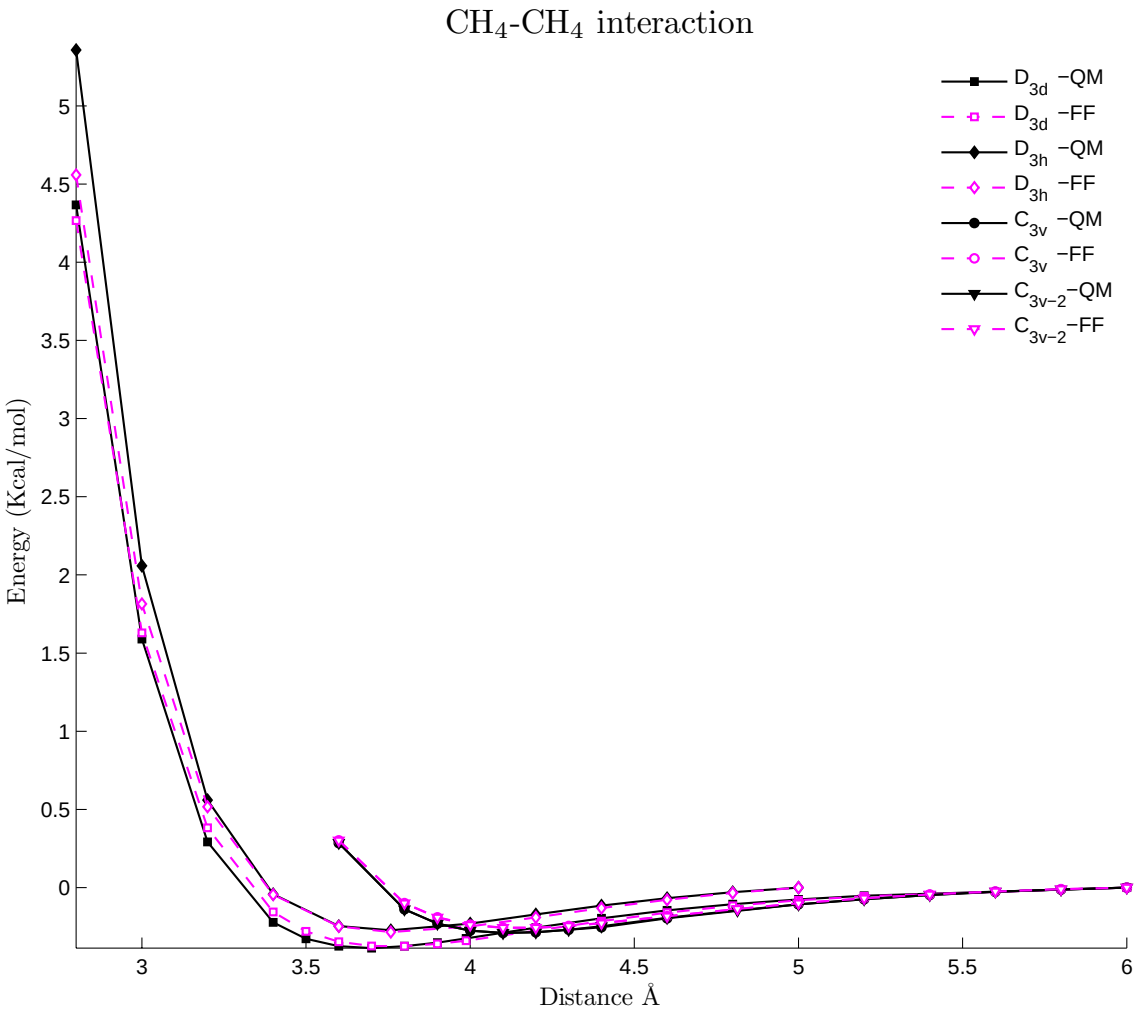

Figure 3.11: Force Field against MP2 results

3.2 C_6H_6–CH_4 interaction

In order to calculate the properties of the intereactions in C_6H_6–CH_4 ANTI system four symmetries were studied. These symetries were found to be the most stable. These are shown in the Figure 3.12.

- ANTI C_{3v}-*1* 3.2.1
- SYN C_{3v}-*2* 3.2.3
- ANTI2 C_{3v}-*3* 3.2.2
- SYN2 C_{3v}-*4* 3.2.4

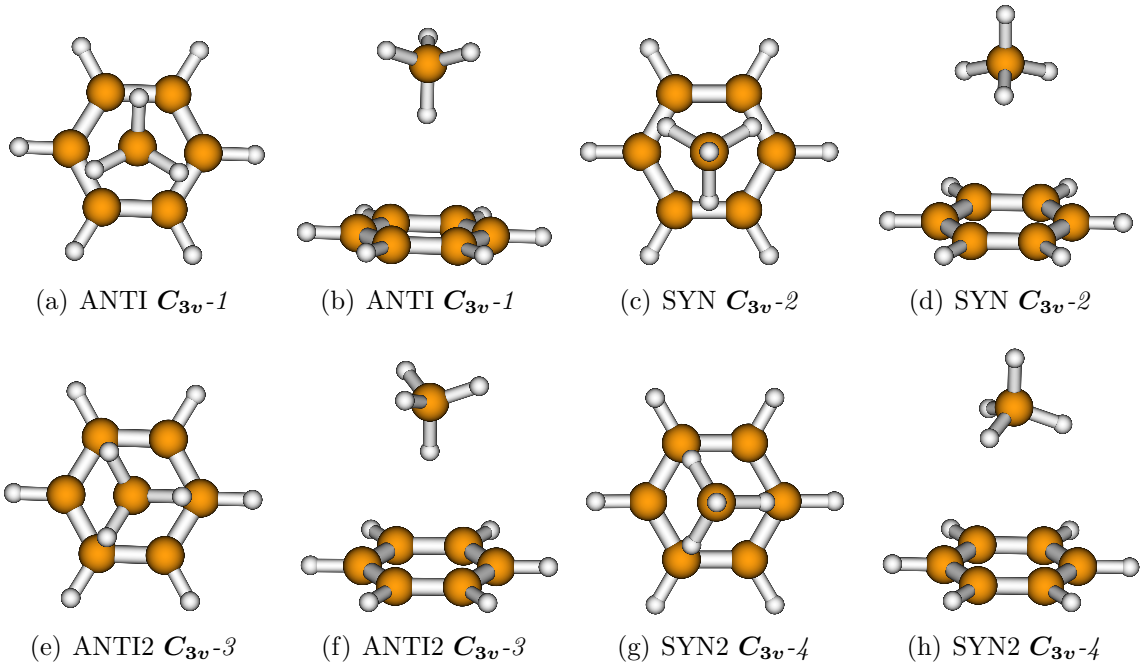

(a) ANTI C_{3v}-*1* (b) ANTI C_{3v}-*1* (c) SYN C_{3v}-*2* (d) SYN C_{3v}-*2*

(e) ANTI2 C_{3v}-*3* (f) ANTI2 C_{3v}-*3* (g) SYN2 C_{3v}-*4* (h) SYN2 C_{3v}-*4*

Figure 3.12: The structures used for calculations of C_6H_6–CH_4 interaction

3.2.1 C_6H_6–CH_4-ANTI with C_{3v}-*1* symmetry

For each structure the **IR-MP2** calculation method was applied, then the BSSE was corrected using the CP method 2.1. The structure used to perform this calculation is shown in Figure 3.13. The data is plotted in the Figure 3.14. The values obtained after normalization are shown in the Table 3.6

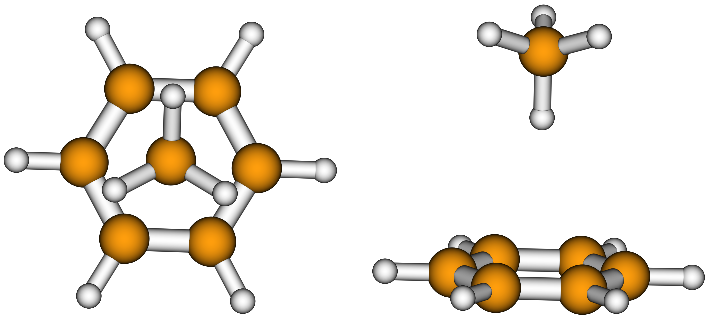

(a) $\boldsymbol{C_{3v}}$-*1* (b) $\boldsymbol{C_{3v}}$-*1*

Figure 3.13: C_6H_6–CH_4 interaction with $\boldsymbol{C_{3v}}$-*1* symmetry

Table 3.6: Energies of C_6H_6–CH_4 $\boldsymbol{C_{3v}}$-*1* symmetry

C-C$_{\text{Distance}}$/(Å)	**E**$_{\text{Not corrected}}$/(Kcal/mol)	**E**$^{\text{CP}}_{\text{corrected}}$/(Kcal/mol)
2.200000	65.41944843778040	69.04132942792060
2.400000	37.14914698724170	38.05390966778940
2.600000	19.78083402058100	20.44978708497370
2.800000	9.70919453201350	10.19167357872720
3.000000	4.24275426892563	4.56961993665027
3.200000	1.52556222848943	1.72465185977126
3.400000	0.35913451263332	0.45888249640120
3.656600	0.00000000000000	0.00000000000000
3.800000	0.06414578374824	0.02274899596159
4.000000	0.27968139640871	0.19426264359936
4.200000	0.53902050928446	0.42217713663194
4.400000	0.78616508760024	0.64747532575348
4.600000	1.00010783263133	0.84592589460954
4.800000	1.17644872688106	1.01162165897040
5.800000	1.64630491318530	1.45170530909672

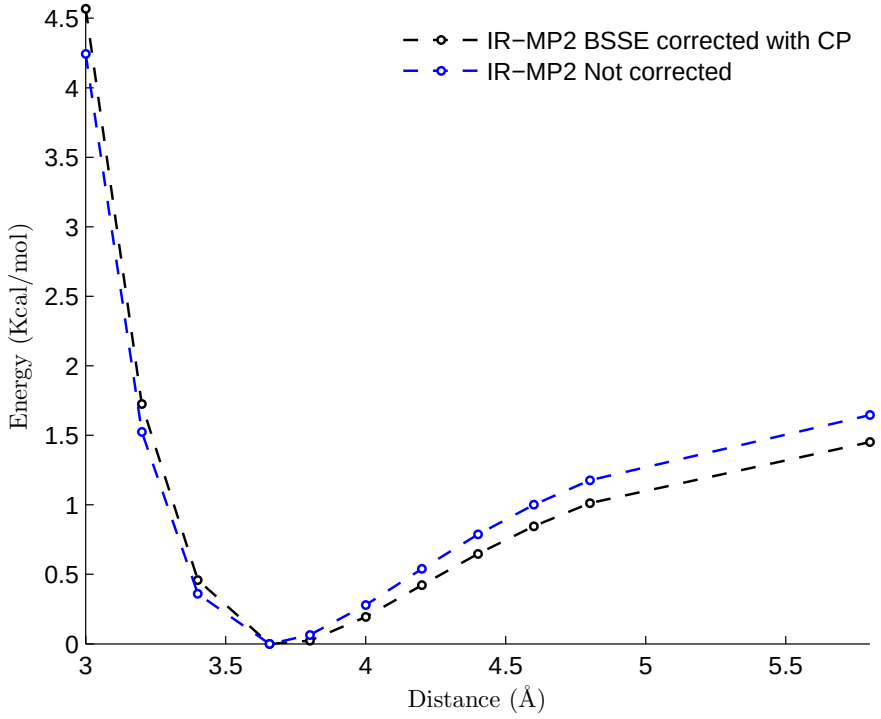

Figure 3.14: Energies of C_6H_6–CH_4 ***C*$_{3v}$-*1*** symmetry

3.2.2 C_6H_6–CH_4-SYN with C_{3v}-*2* symmetry

For each structure the **IR-MP2** calculation method was applied, then the BSSE was corrected using the *C*P method 2.1. The structure used to perform this calculation is shown in Figure 3.15. The data is plotted in the Figure 3.16. The values obtained after normalization are shown in the Table 3.7

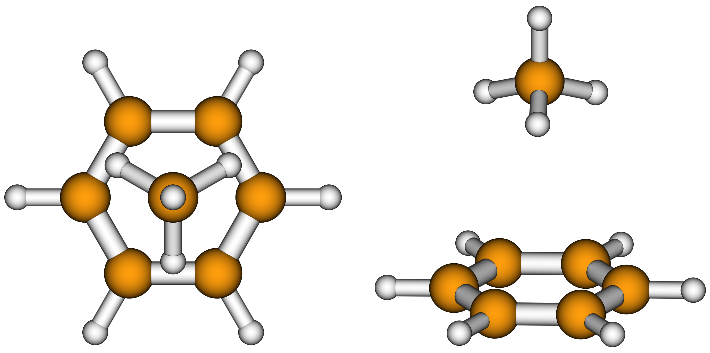

(a) ***C*$_{3v}$-*1*** (b) ***C*$_{3v}$-*1***

Figure 3.15: C_6H_6–CH_4 interaction with ***C*$_{3v}$-*2*** symmetry

Table 3.7: Energies of C_6H_6–CH_4 $\boldsymbol{C_{3v}}$-*2* symmetry

C-C$_{\text{Distance}}$/(Å)	**E**$_{\text{Not corrected}}$/(Kcal/mol)	**E**$^{\text{CP}}_{\text{corrected}}$/(Kcal/mol)
2.20000	85.20625490491510	86.41829824350860
2.40000	59.11691336290100	60.01384539781430
2.60000	29.24726877224750	29.90833528623260
2.80000	9.71662454886246	10.19119663377930
3.00000	4.24781301521580	4.56796476992531
3.20000	1.52828473056434	1.72121414055437
3.40000	-0.00016359859728	0.09189179519308
3.64360	0.00000000000000	0.00000000000000
3.80000	0.06291986111319	0.01798372127814
4.00000	0.27818654774455	0.18895657439862
4.20000	0.53740596189164	0.41688227211125
4.40000	0.78449252754217	0.64148743922124
4.60000	0.99822196018067	0.83984645679084
4.80000	1.17472100688610	1.00569548491694
5.80000	1.64446898605092	1.44631035224302

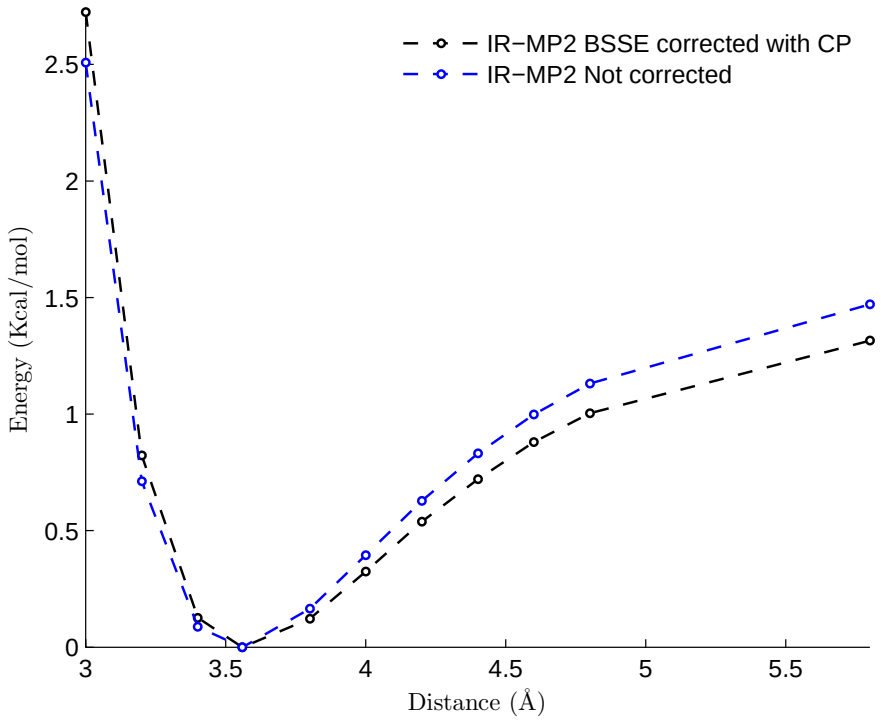

Figure 3.16: Energies of C_6H_6–CH_4 $\boldsymbol{C_{3v}}$-*2* symmetry

3.2.3 C_6H_6–CH_4-ANTI2 with C_{3v}-*3* symmetry

For each structure the **IR-MP2** calculation method was applied, then the BSSE was corrected using the *C*P method 2.1. The structure used to perform this calculation is shown in Figure 3.17. The data is plotted in the Figure 3.18. The values obtained after normalization are shown in the Table 3.8

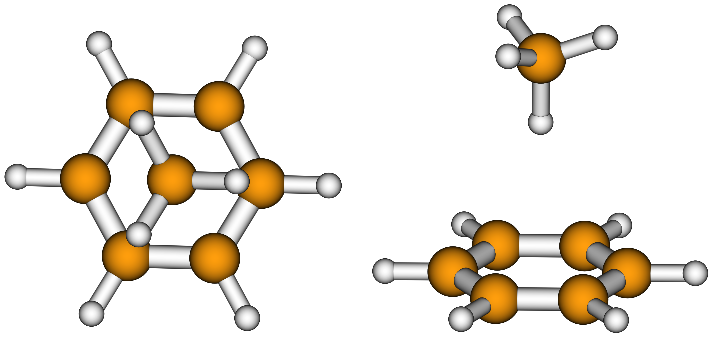

(a) $\boldsymbol{C_{3v}}$-*1* (b) $\boldsymbol{C_{3v}}$-*1*

Figure 3.17: C_6H_6–CH_4 interaction with $\boldsymbol{C_{3v}}$-*3* symmetry

Table 3.8: Energies of C_6H_6–CH_4 $\boldsymbol{C_{3v}}$-*3* symmetry

C-C$_{\text{Distance}}$/(Å)	**E**$_{\text{Not corrected}}$/(Kcal/mol)	**E**$^{\text{CP}}_{\text{corrected}}$/(Kcal/mol)
2.20000	61.55530227228880	62.60119646102610
2.40000	31.55394161911680	32.32860963097850
2.60000	15.14700692129550	15.69637593935840
2.80000	6.63318819578853	6.99744762334740
3.00000	2.50714866514317	2.72554163362292
3.20000	0.71158224137616	0.82267717403374
3.40000	0.08687590039335	0.12588604860139
3.55920	0.00000000000000	0.00000000000000
3.80000	0.16534100411809	0.12249221789534
4.00000	0.39542732716654	0.32448074639979
4.20000	0.62744528448093	0.53859097447639
4.40000	0.83102353039431	0.72033064266361
4.60000	0.99817097000778	0.87950223091684
4.80000	1.13133859756636	1.00349998859747
5.80000	1.47040263173403	1.31529413512180

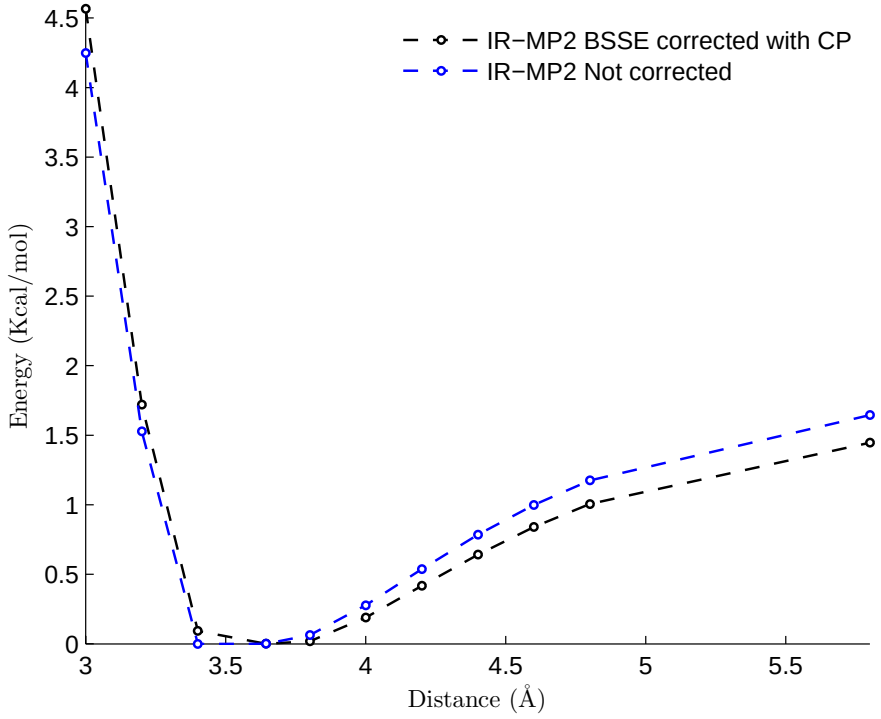

Figure 3.18: Energies of C_6H_6–CH_4 $\boldsymbol{C_{3v}}$-*3* symmetry

3.2.4 C_6H_6–CH_4-SYN2 with C_{3v}-*4* symmetry

For each structure the **IR-MP2** calculation method was applied, then the BSSE was corrected using the *C*P method 2.1. The structure used to perform this calculation is shown in Figure 3.19. The data is plotted in the Figure 3.20. The values obtained after normalization are shown in the Table 3.9

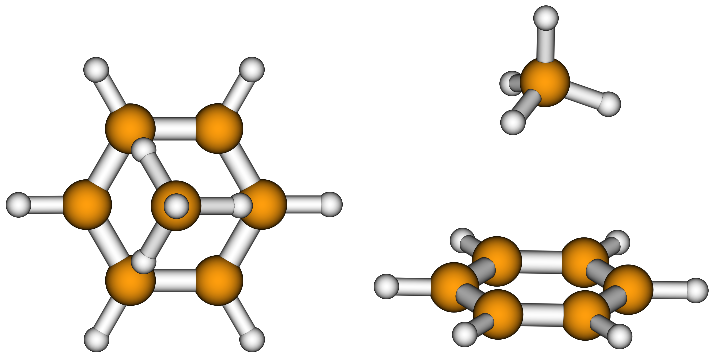

(a) $\boldsymbol{C_{3v}}$-*1* (b) $\boldsymbol{C_{3v}}$-*1*

Figure 3.19: C_6H_6–CH_4 interaction with $\boldsymbol{C_{3v}}$-*4* symmetry

Table 3.9: Energies of C_6H_6–CH_4 $\boldsymbol{C_{3v}}$-*4* symmetry

C-C$_{\text{Distance}}$/(Å)	**E**$_{\text{Not corrected}}$/(Kcal/mol)	**E**$^{\text{CP}}_{\text{corrected}}$/(Kcal/mol)
2.20000	61.83197976445080	62.90000740337930
2.40000	31.64323150645940	32.42705487485360
2.60000	15.17341971228600	15.72637886028680
2.80000	6.64042931716540	7.00364098977297
3.00000	2.50960519915679	2.72369688799154
3.20000	0.71275306178723	0.81809614469967
3.40000	0.08733824180672	0.11983931284340
3.52380	0.00000000000000	0.00000000000000
3.60000	0.01100619154749	-0.00522787505543
3.80000	0.16677241225261	0.11454791158030
4.00000	0.39767355954973	0.31618573402739
4.20000	0.63024798032711	0.52550591965337
4.40000	0.83405657493859	0.71194043634387
4.60000	1.00135026627686	0.86692583423428
5.60000	1.43513292941498	1.75681103835813

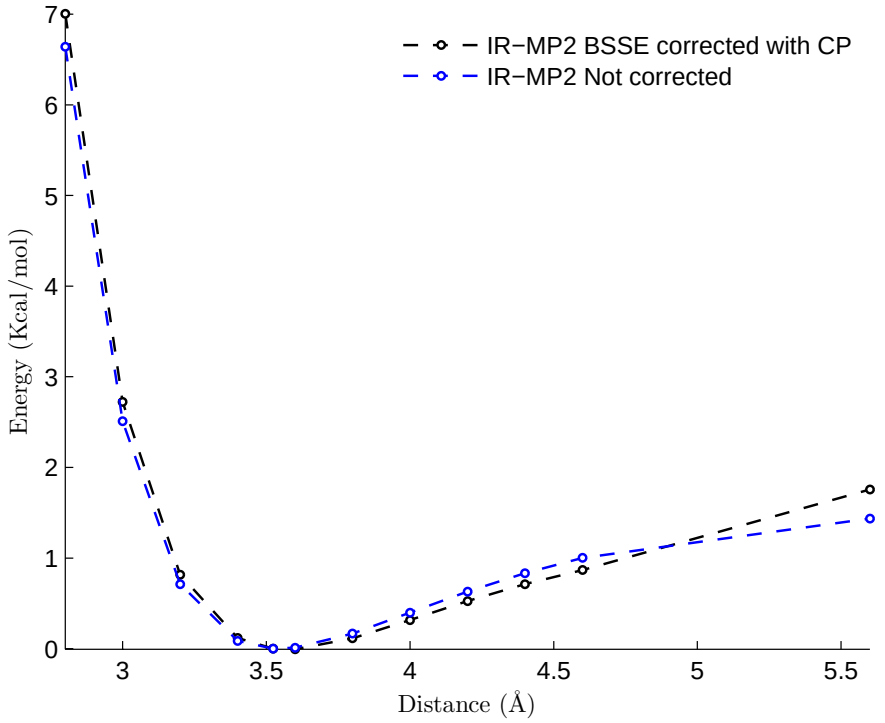

Figure 3.20: Energies of C_6H_6–CH_4 $\boldsymbol{C_{3v}}$-*4* symmetry

3.2.5 Fitting Quantum Mechanics to a Force Field

The MP2 results were fitted into a Force Field with a Morse Type Potential equation 2.4. The four geometries (see Figure 3.12) were used to obtain the best fitting for these configurations. The parameters obtained are shown in Table 3.10. Energies of the Force Field against Quantum Mechanics results are shown in Figure 3.22 and in Figure 3.21

Table 3.10: Parameters from Fitting equation 2.4 in C_6H_6–CH_4

Term	$\mathbf{D}$/(Kcal/mol)	$\mathbf{r_0}$/(Å)	$\boldsymbol{\alpha}$
C_{COF}—C_{CH_4}	0.04983	4.22836	13.24927
H_{COF}—C_{CH_4}	0.00088	3.25038	12.01304
C_{COF}—H_{CH_4}	0.11441	3.08342	9.07362
H_{COF}—H_{CH_4}	0.00088	3.2623	12.04535

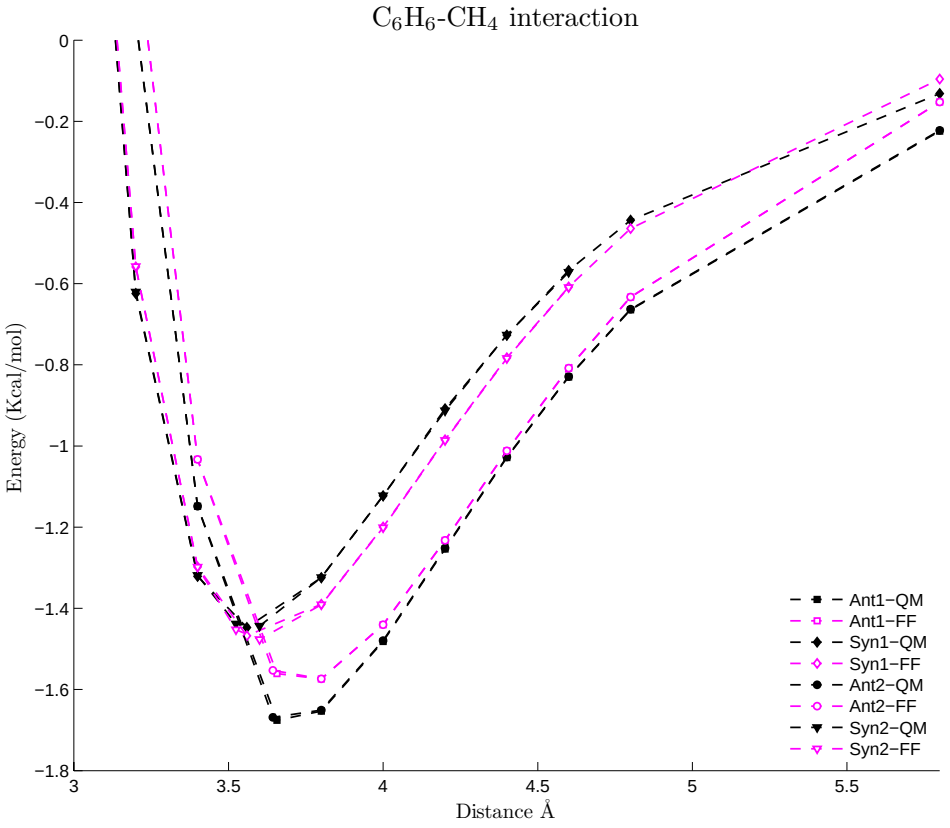

Figure 3.21: Force Field against MP2 results

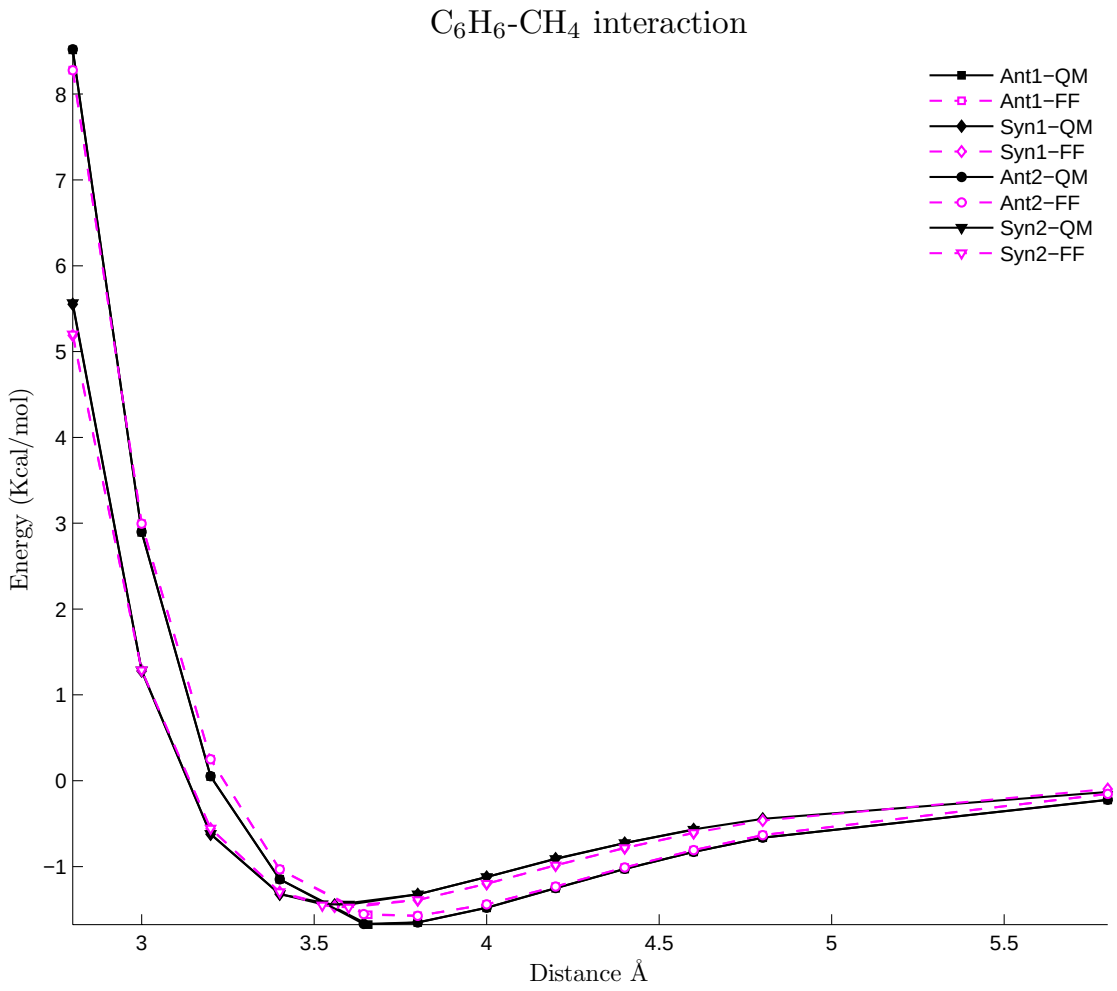

Figure 3.22: Force Field against MP2 results

3.3 $B_3O_3H_3$–CH_4 interaction

In order to calculate the properties of the intereactions in $B_3O_3H_3$–CH_4 system four symmetries were studied. These symetries were found to be the most stable. These are shown in the Figure 3.23.

- ANTI C_{3v}-*1* 3.3.1
- SYN C_{3v}-*2* 3.3.3
- ANTI2 C_{3v}-*3* 3.3.2
- SYN2 C_{3v}-*4* 3.3.4

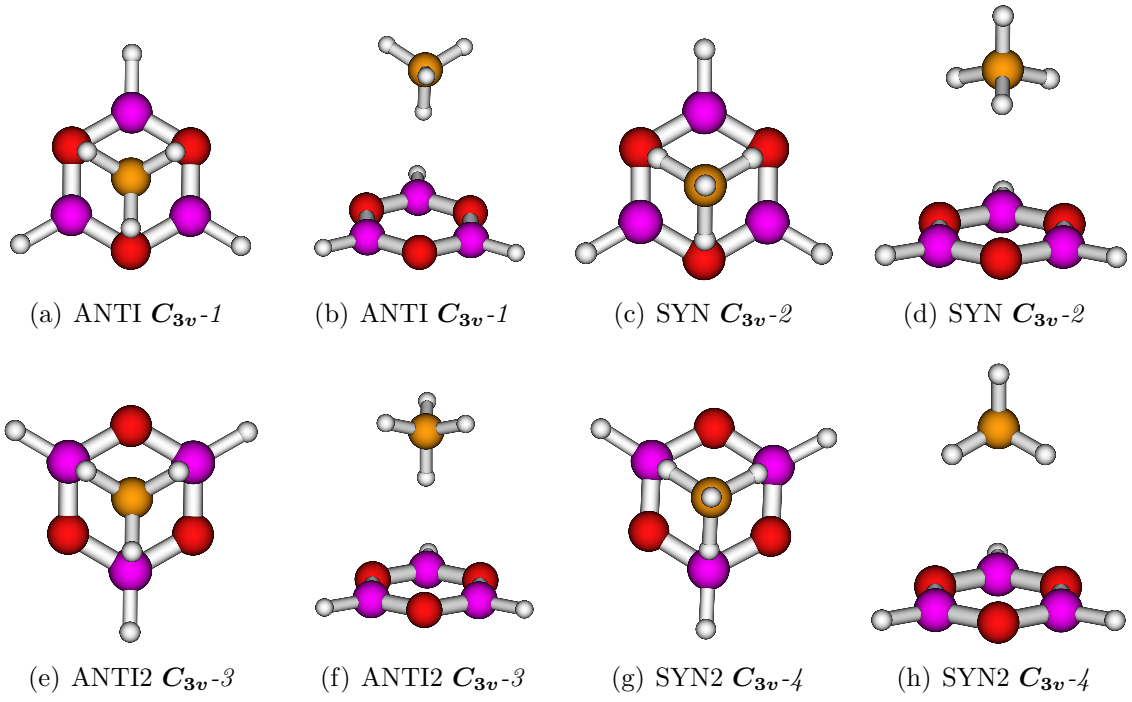

(a) ANTI C_{3v}-*1* (b) ANTI C_{3v}-*1* (c) SYN C_{3v}-*2* (d) SYN C_{3v}-*2*

(e) ANTI2 C_{3v}-*3* (f) ANTI2 C_{3v}-*3* (g) SYN2 C_{3v}-*4* (h) SYN2 C_{3v}-*4*

Figure 3.23: The structures used to calculate the $B_3O_3H_3$–CH_4 interaction

3.3.1 $B_3O_3H_3$–CH_4-ANTI with C_{3v}-*1* symmetry

For each structure the **IR-MP2** calculation method was applied, then the BSSE was corrected using the *C*P method 2.1. The structure used to perform this calculation is shown in Figure 3.24. The data is plotted in the Figure 3.25. The values obtained after normalization are shown in the Table 3.11

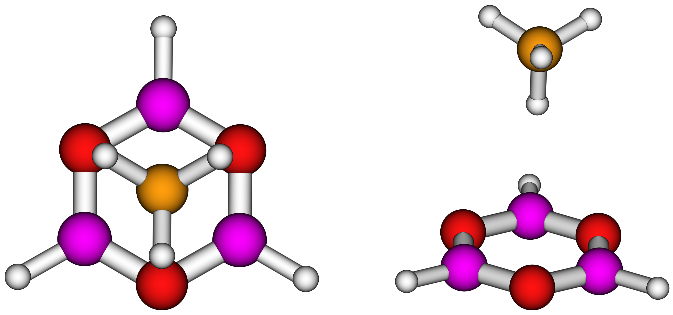

(a) $\boldsymbol{C_{3v}}$-*1* (b) $\boldsymbol{C_{3v}}$-*1*

Figure 3.24: $B_3O_3H_3$–CH_4 interaction with $\boldsymbol{C_{3v}}$-*1* symmetry

Table 3.11: Energies of $B_3O_3H_3$–CH_4 $\boldsymbol{C_{3v}}$-*1* symmetry

C-C$_{\text{Distance}}$/(Å)	**E**$_{\text{Not corrected}}$/(Kcal/mol)	**E**$^{\text{CP}}_{\text{corrected}}$/(Kcal/mol)
2.800000	8.90100051570334	9.28569735790006
3.000000	4.23088553786511	4.48834267424536
3.200000	1.78057831226033	1.95118842307784
3.400000	0.60252155837952	0.70522996586806
3.600000	0.12312561439467	0.16926105835591
3.800000	0.00000000000000	0.00000000000000
4.018200	0.04524618529831	0.00404487363630
4.200000	0.13806713072700	0.07134501825203
4.400000	0.25068175519118	0.16205746398555
4.600000	0.35467813280411	0.25019640661776
4.800000	0.43983932142146	0.32291446909221
5.000000	0.50880245794542	0.38524209662137
5.200000	0.56231945383479	0.43208626992055
6.200000	0.69469059677795	0.55069543375794

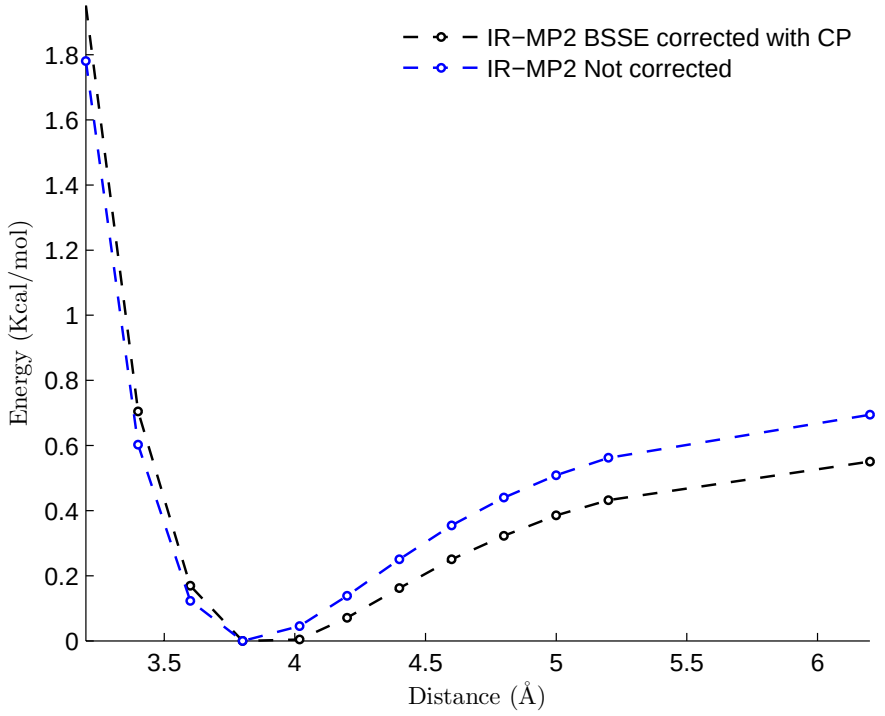

Figure 3.25: Energies of $B_3O_3H_3$–CH_4 $\boldsymbol{C_{3v}}$-*1* symmetry

3.3.2 $B_3O_3H_3$–CH_4-SYN with C_{3v}-*2* symmetry

For each structure the **IR-MP2** calculation method was applied, then the BSSE was corrected using the *C*P method 2.1. The structure used to perform this calculation is shown in Figure 3.26. The data is plotted in the Figure 3.27. The values obtained after normalization are shown in the Table 3.12

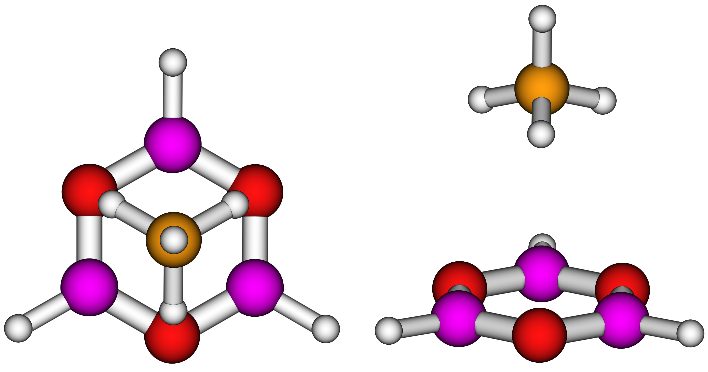

(a) $\boldsymbol{C_{3v}}$-*2* (b) $\boldsymbol{C_{3v}}$-*2*

Figure 3.26: $B_3O_3H_3$–CH_4 interaction with $\boldsymbol{C_{3v}}$-*2* symmetry

Table 3.12: Energies of $B_3O_3H_3$–CH_4 $\boldsymbol{C_{3v}}$-*2* symmetry

C-C$_{\text{Distance}}$/(Å)	**E**$_{\text{Not corrected}}$/(Kcal/mol)	**E**$^{\text{CP}}_{\text{corrected}}$/(Kcal/mol)
2.00000	79.14134549829760	80.40368694820430
2.20000	40.66689383177440	41.52625055928730
2.40000	19.66994270603750	20.25097966929390
2.80000	3.42859439743916	3.67628675236483
3.00000	1.05066278154845	1.19067857932168
3.20000	0.16956125968136	0.22293487756178
3.35230	0.00000000000000	0.00000000000000
3.80000	0.35030122520402	0.24938824061974
4.00000	0.58871338376775	0.46160678875458
4.20000	0.80077586189145	0.65241249328028
4.40000	0.97791027766652	0.81368655825281
4.60000	1.12003037999966	0.94338748360678

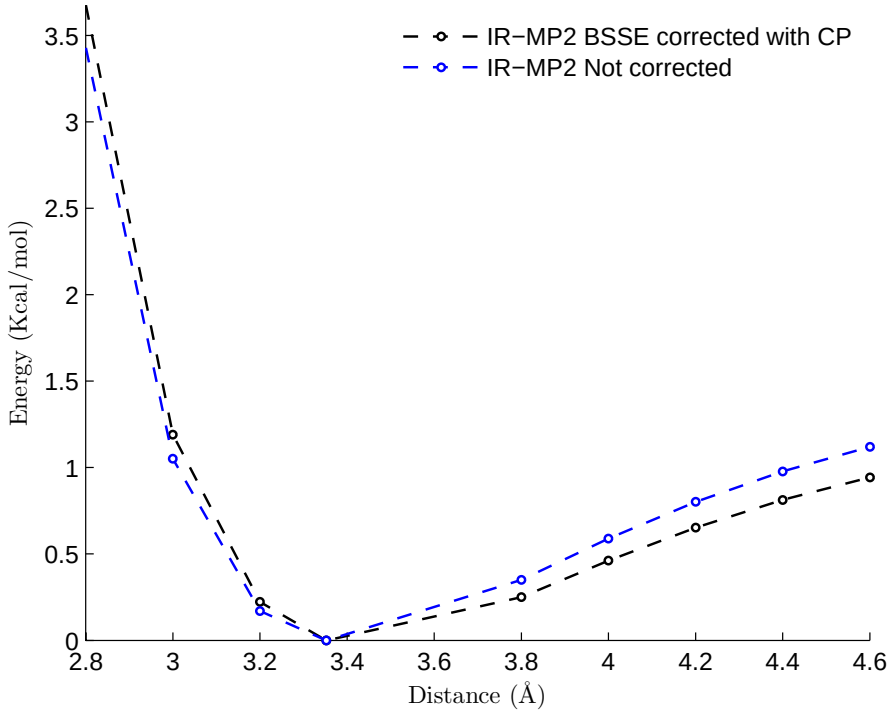

Figure 3.27: Energies of $B_3O_3H_3$–CH_4 $\boldsymbol{C_{3v}}$-*2* symmetry

3.3.3 $B_3O_3H_3$–CH_4-ANTI2 with C_{3v}-*3* symmetry

For each structure the **IR-MP2** calculation method was applied, then the BSSE was corrected using the *C*P method 2.1. The structure used to perform this calculation is shown in Figure 3.28. The data is plotted in the Figure 3.29. The values obtained after normalization are shown in the Table 3.13

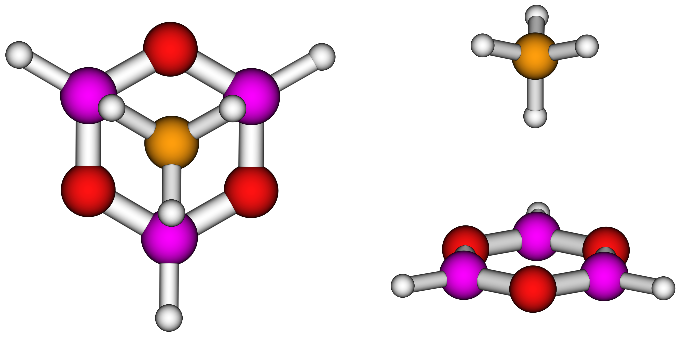

(a) $\boldsymbol{C_{3v}}$-*3* (b) $\boldsymbol{C_{3v}}$-*3*

Figure 3.28: $B_3O_3H_3$–CH_4 interaction with $\boldsymbol{C_{3v}}$-*3* symmetry

Table 3.13: Energies of $B_3O_3H_3$–CH_4 $\boldsymbol{C_{3v}}$-*3* symmetry

C-C$_{\text{Distance}}$/(Å)	**E**$_{\text{Not corrected}}$/(Kcal/mol)	**E**$^{\text{CP}}_{\text{corrected}}$/(Kcal/mol)
2.40000	30.02545711965650	30.83115178346270
2.60000	16.47187244435190	17.04429915962100
2.80000	8.49521082988940	8.88402310170568
3.00000	4.03377094792086	4.29085413850771
3.20000	1.68833792104851	1.85789103570642
3.40000	0.56695707974723	0.66987626917035
3.72140	0.01709263902740	0.03549743241092
3.80000	0.00000000000000	0.00000000000000
4.00000	0.04452099706396	0.00760484432976
4.20000	0.14727061367012	0.08173336946493
4.60000	0.36520386798657	0.26178378285840
4.80000	0.45270802269806	0.33768657258042
5.80000	0.67340897794929	0.53295375031303

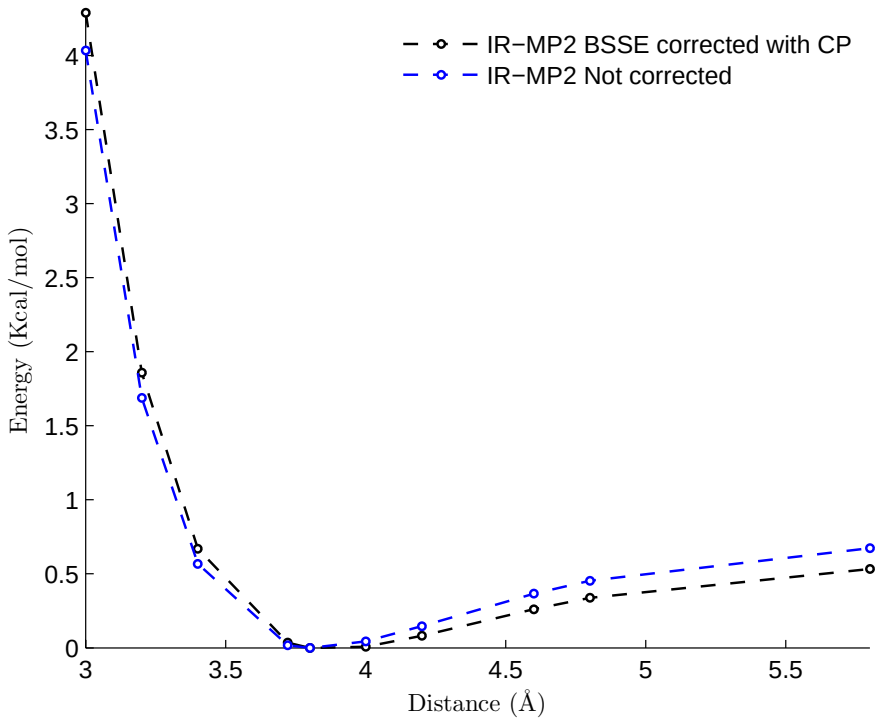

Figure 3.29: Energies of $B_3O_3H_3$–CH_4 $\boldsymbol{C_{3v}}$-*3* symmetry

3.3.4 $B_3O_3H_3$–CH_4-SYN2 with C_{3v}-*4* symmetry

For each structure the **IR-MP2** calculation method was applied, then the BSSE was corrected using the *C*P method 2.1. The structure used to perform this calculation is shown in Figure 3.30. The data is plotted in the Figure 3.31. The values obtained after normalization are shown in the Table 3.14

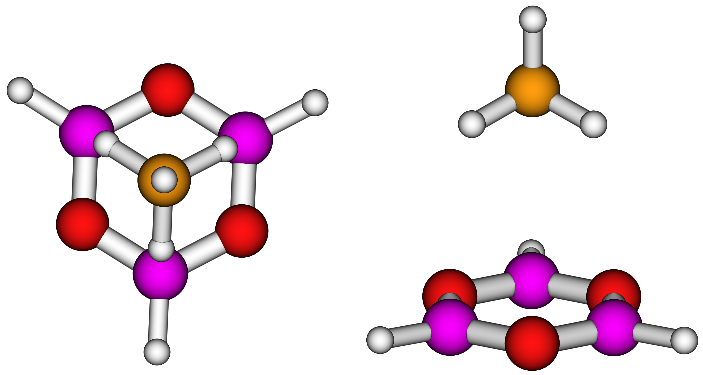

(a) $\boldsymbol{C_{3v}}$-*2* (b) $\boldsymbol{C_{3v}}$-*2*

Figure 3.30: $B_3O_3H_3$–CH_4 interaction with $\boldsymbol{C_{3v}}$-*4* symmetry

Table 3.14: Energies of $B_3O_3H_3$–CH_4 $\boldsymbol{C_{3v}}$-*4* symmetry

$\mathbf{C\text{-}C}_{\text{Distance}}/(\text{Å})$	$\mathbf{E}_{\text{Not corrected}}/(\text{Kcal/mol})$	$\mathbf{E}^{\text{CP}}_{\text{corrected}}/(\text{Kcal/mol})$
2.00000	68.54995461102230	69.63177092405750
2.60000	8.39849524231977	8.77382396461689
2.80000	3.46100247633876	3.71930888426505
3.00000	1.16022079155664	1.32050391409211
3.20000	0.24215623480268	0.31989491471541
3.43620	0.00000000000000	0.00000000000000
3.60000	0.06678465451114	0.02544217764807
3.80000	0.24250262446003	0.16307300571862
4.20000	0.62220750909182	0.49575120529335
4.40000	0.77692014948116	0.63508823493612
5.60000	1.22480167725007	1.07291369790619

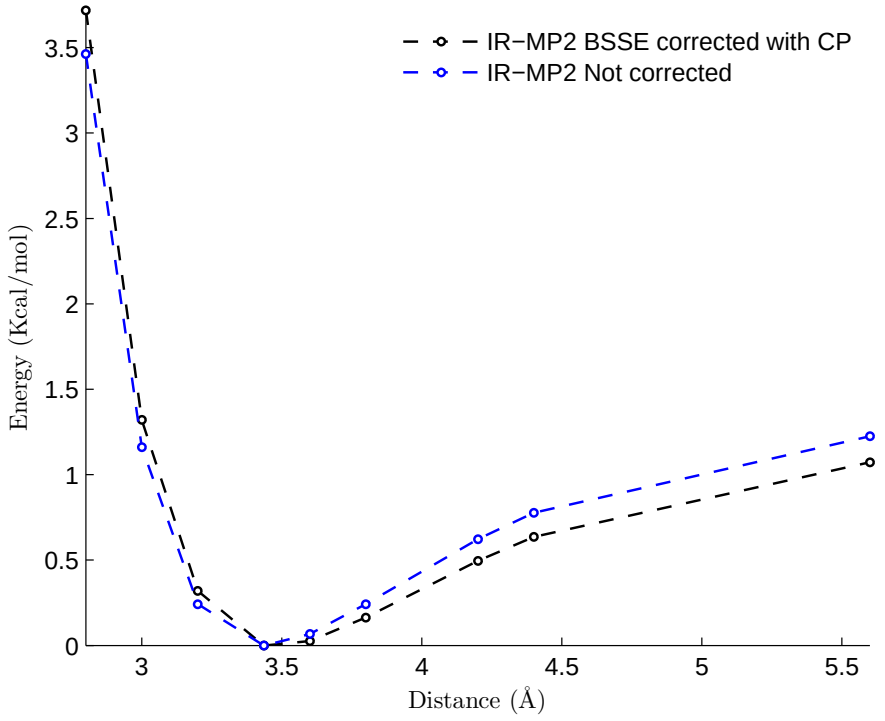

Figure 3.31: Energies of $B_3O_3H_3$–CH_4 $\boldsymbol{C_{3v}}$-*4* symmetry

3.3.5 Fitting Quantum Mechanics to a Force Field

The MP2 results were fitted into a Force Field with a Morse Type Potential equation 2.4. The four geometries (see Figure 3.23) were used to obtain the best fitting for these configurations. The parameters obtained are shown in Table 3.15. Energies of the Force Field against Quantum Mechanics results are shown in Figure 3.33 and in Figure 3.32

Table 3.15: Parameters from Fitting equation 2.4 in $B_3O_3H_3$–CH_4

Term	$\mathbf{D}$/(Kcal/mol)	$\mathbf{r_0}$/(Å)	$\boldsymbol{\alpha}$
O_{COF}—C_{CH_4}	0.04824	3.59396	11.26448
B_{COF}—C_{CH_4}	0.04651	4.113	12.2858
O_{COF}—H_{CH_4}	0.09212	2.54864	8.99322
B_{COF}—H_{CH_4}	0.09174	3.27898	11.71868

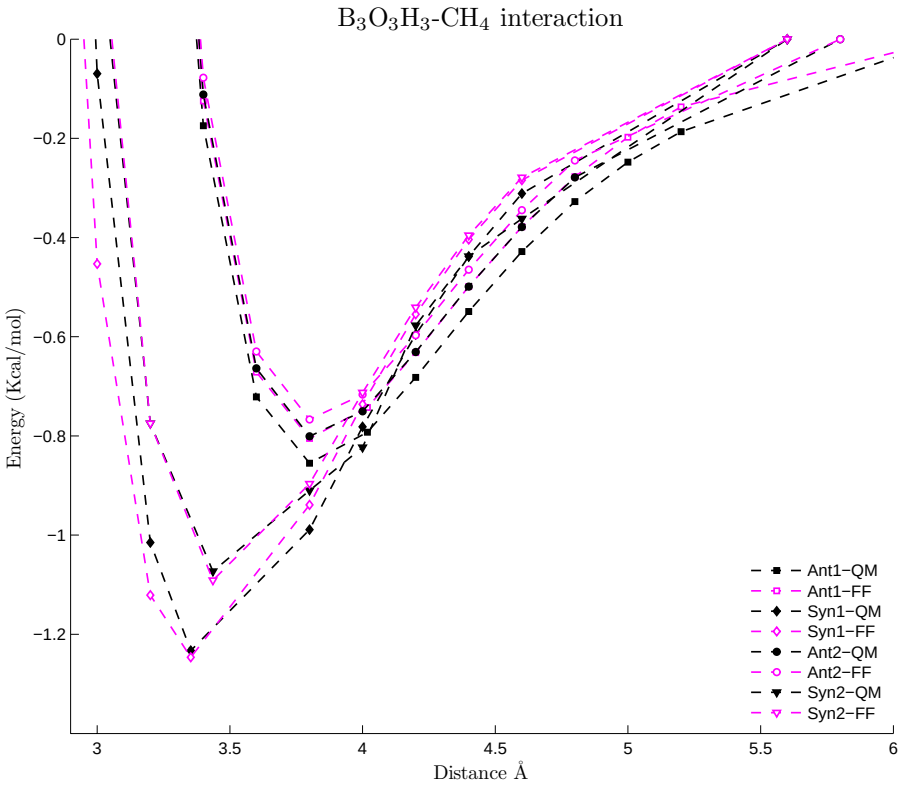

Figure 3.32: Force Field against MP2 results

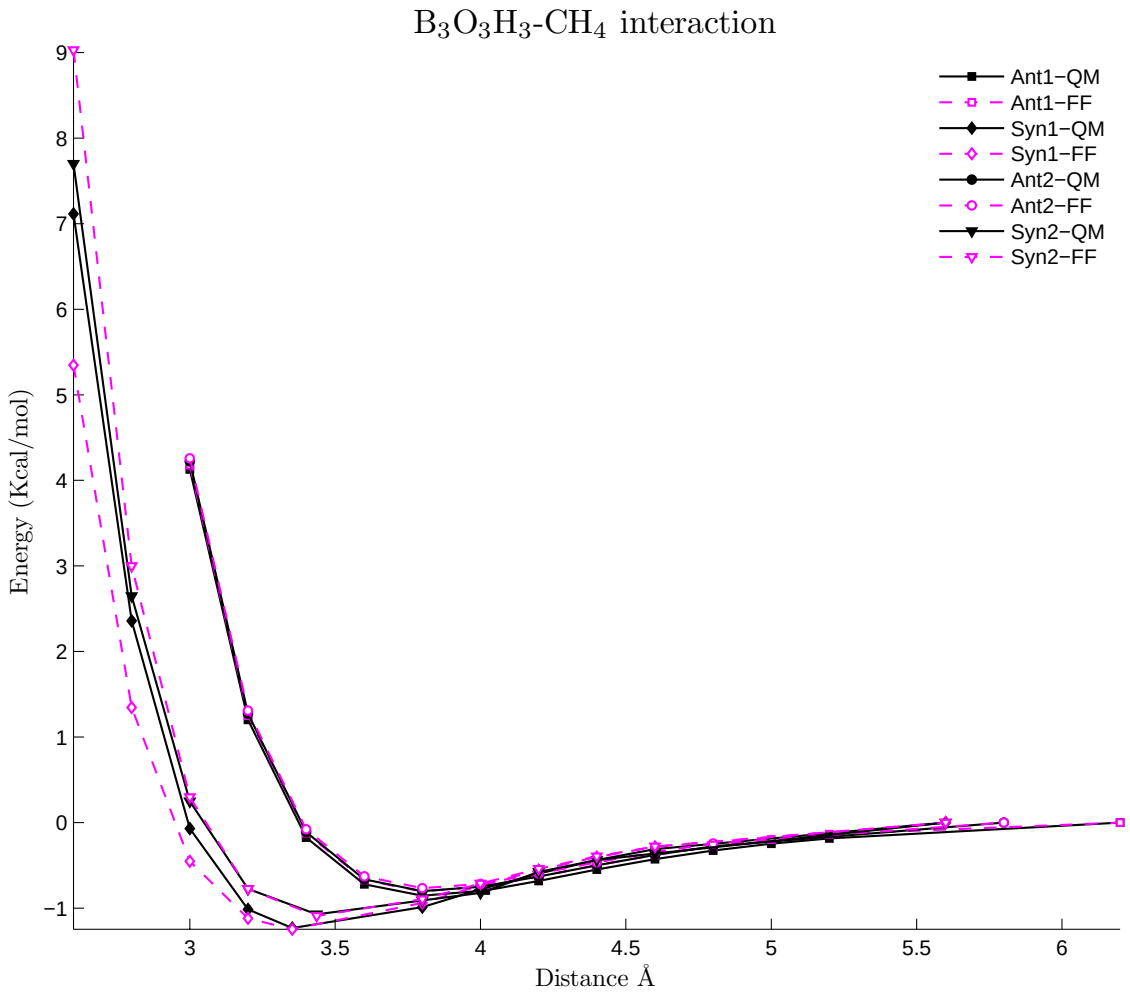

Figure 3.33: Force Field against MP2 results

3.4 $Si(CH_4)_4$–CH_4 interaction

In order to calculate the properties of the intereactions in $Si(CH_4)_4$–CH_4 system four symmetries were studied. These symetries were found to be the most stable. These are shown in the Figure 3.34.

- ANTI C_{3v}-*1* 3.4.1
- SYN C_{3v}-*2* 3.4.2
- ANTI2 C_{3v}-*3* 3.4.3
- SYN2 C_{3v}-*4* 3.4.4

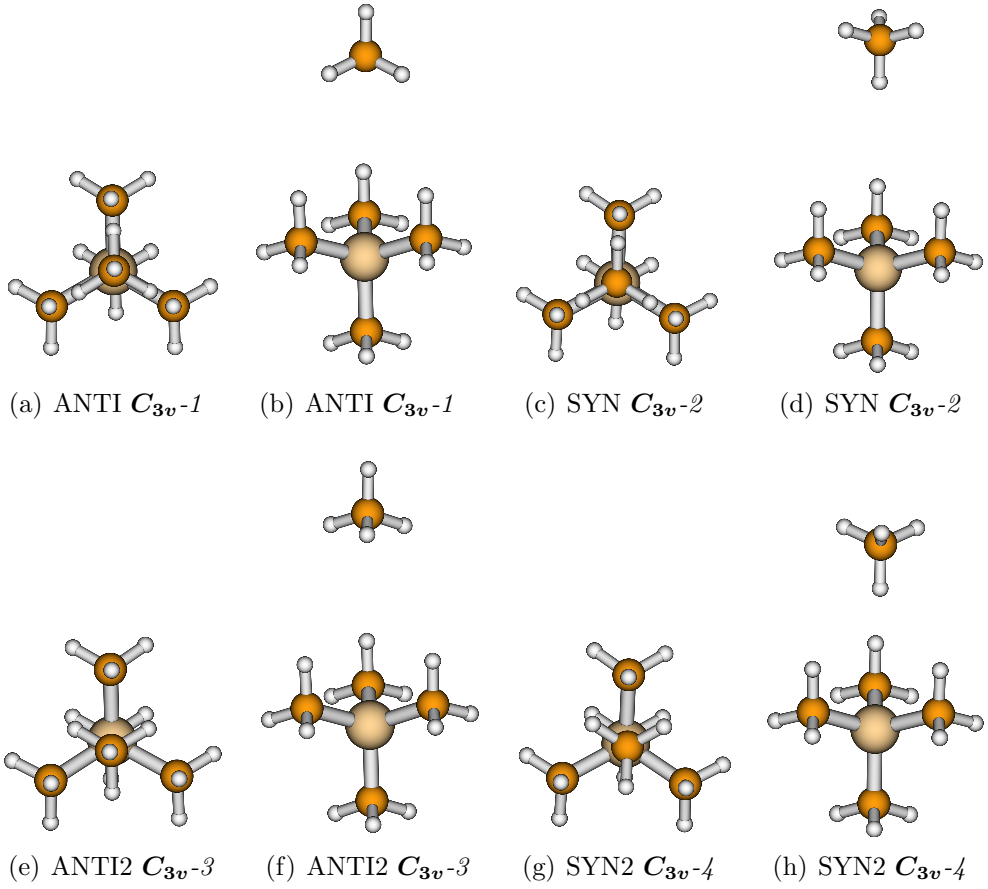

(a) ANTI C_{3v}-*1* (b) ANTI C_{3v}-*1* (c) SYN C_{3v}-*2* (d) SYN C_{3v}-*2*

(e) ANTI2 C_{3v}-*3* (f) ANTI2 C_{3v}-*3* (g) SYN2 C_{3v}-*4* (h) SYN2 C_{3v}-*4*

Figure 3.34: The structures used to calculate the $Si(CH_4)_4$–CH_4 interaction

3.4.1 $Si(CH_4)_4$–CH_4-ANTI with C_{3v}-*1* symmetry

For each structure the **IR-MP2** calculation method was applied, then the BSSE was corrected using the *C*P method 2.1. The structure used to perform this calculation is shown in Figure 3.35. The data is plotted in the Figure 3.36. The values obtained after normalization are shown in the Table 3.16

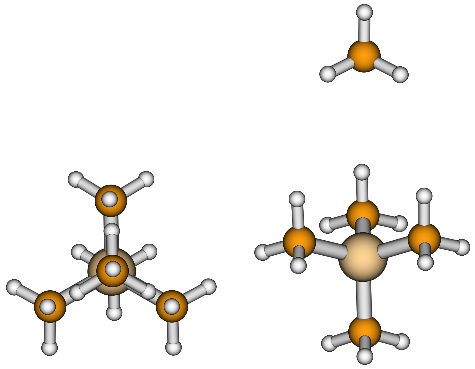

(a) C_{3v}-*1* (b) C_{3v}-*1*

Figure 3.35: $Si(CH_4)_4$–CH_4 interaction with C_{3v}-*1* symmetry

Table 3.16: Energies of $Si(CH_4)_4$–CH_4 C_{3v}-*1* symmetry

C-C$_{\text{Distance}}$/(Å)	**E**$_{\text{Not corrected}}$/(Kcal/mol)	**E**$^{\text{CP}}_{\text{corrected}}$/(Kcal/mol)
4.000000	1.26815129542956	1.37225594575284
4.100000	0.71542427752866	0.79525244766410
4.200000	0.36223722837167	0.42112964118860
4.400000	0.04049009003211	0.06547270623196
4.600000	0.00000000000000	0.00000000000000
4.800000	0.07868778938428	0.06108567636693
5.068030	0.23948738671606	0.20584710118783
5.200000	0.31877808965510	0.27911550321733
5.400000	0.42726228974061	0.38064750846388
5.600000	0.51809076266363	0.46615160157307
5.800000	0.59263264312176	0.53645418643282
6.000000	0.65262208762579	0.59297380874341
6.200000	0.70064089290099	0.63794837303431
7.000000	0.81501216994366	0.74428278189589
7.500000	0.81480683316477	0.74369628034037

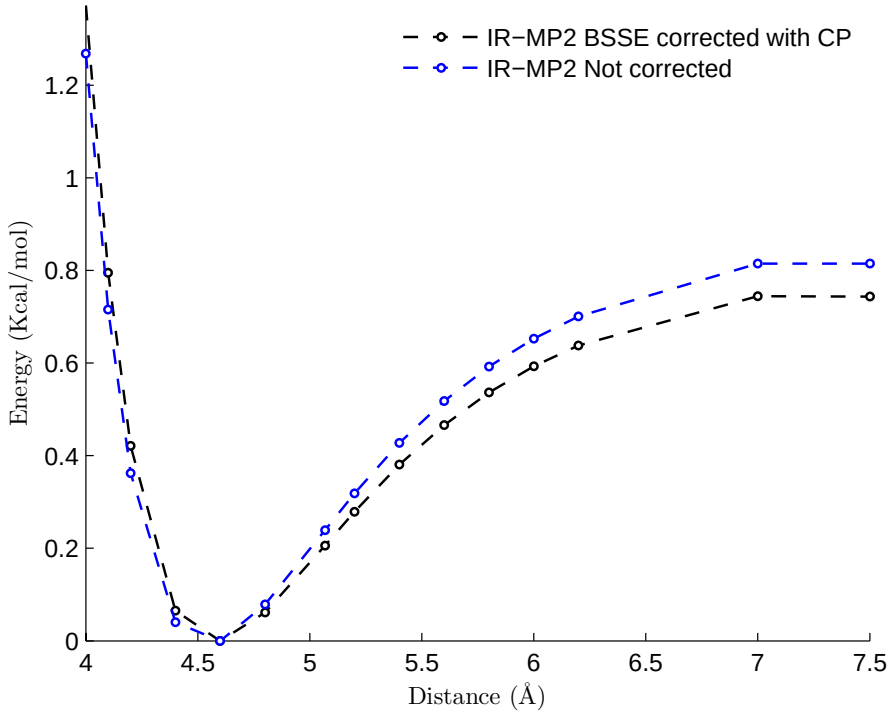

Figure 3.36: Energies of $Si(CH_4)_4$–CH_4 $\boldsymbol{C_{3v}}$-*1* symmetry

3.4.2 $Si(CH_4)_4$–CH_4-SYN with C_{3v}-*2* symmetry

For each structure the **IR-MP2** calculation method was applied, then the BSSE was corrected using the *C*P method 2.1. The structure used to perform this calculation is shown in Figure 3.37. The data is plotted in the Figure 3.38. The values obtained after normalization are shown in the Table 3.17

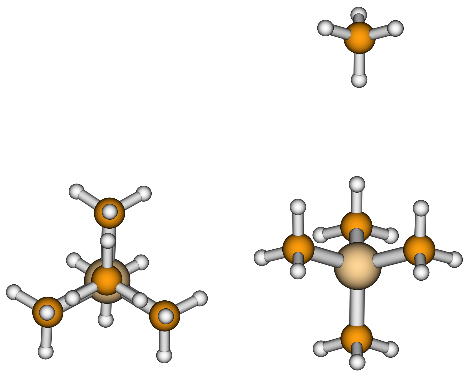

(a) $\boldsymbol{C_{3v}}$-*2* (b) $\boldsymbol{C_{3v}}$-*2*

Figure 3.37: $Si(CH_4)_4$–CH_4 interaction with $\boldsymbol{C_{3v}}$-*2* symmetry

Table 3.17: Energies of $Si(CH_4)_4$–CH_4 $\boldsymbol{C_{3v}}$-*2* symmetry

C-C$_{\text{Distance}}$/(Å)	**E**$_{\text{Not corrected}}$/(Kcal/mol)	$\mathbf{E}^{\text{CP}}_{\text{corrected}}$/(Kcal/mol)
4.00000	1.17179731209762	1.28044531759951
4.20000	0.39861467381707	0.45996894741984
4.40000	0.07669801753946	0.10260370026299
4.60000	0.00000000000000	0.00000000000000
4.80000	0.04569609271130	0.02727799372951
5.00000	0.14354516571621	0.11072887500632
5.20000	0.25579226220725	0.21217328119383
5.40000	0.36279708921211	0.31058836778175
5.60000	0.45648708508816	0.39742518409184
5.80000	0.53493090876145	0.47108129795015
5.91442	0.57309387915302	0.50641115019243
6.00000	0.59870223561302	0.53039978045490
6.20000	0.65010017523309	0.57854817926636
6.40000	0.69057906290982	0.61634822440465
6.60000	0.72325589408865	0.64674710183681
6.80000	0.74903337570140	0.67071240612131
7.50000	0.80469209532021	0.72214287439056

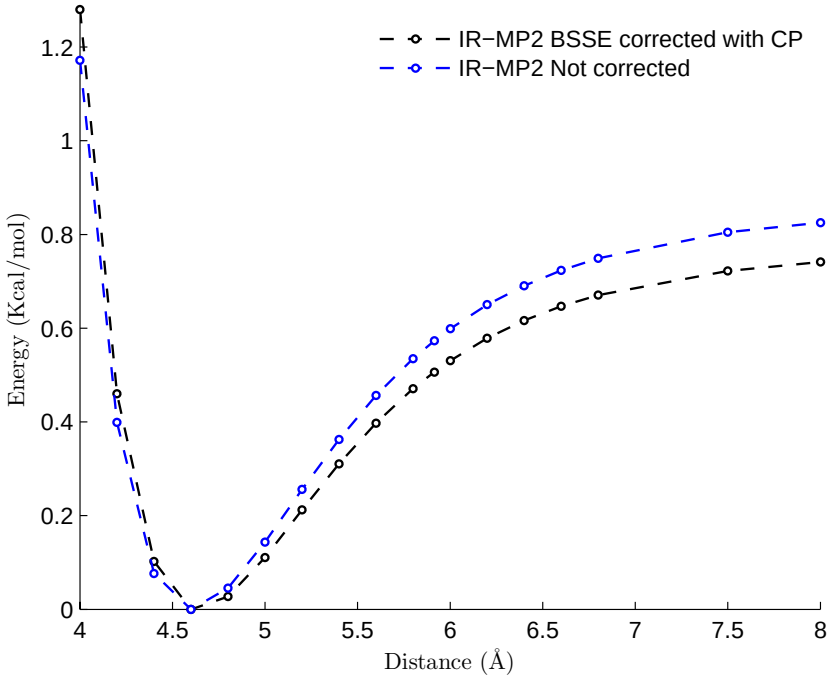

Figure 3.38: Energies of $Si(CH_4)_4$–CH_4 $\boldsymbol{C_{3v}}$-*2* symmetry

3.4.3 $Si(CH_4)_4$–CH_4-ANTI2 with C_{3v}-*3* symmetry

For each structure the **IR-MP2** calculation method was applied, then the BSSE was corrected using the *C*P method 2.1. The structure used to perform this calculation is shown in Figure 3.39. The data is plotted in the Figure 3.40. The values obtained after normalization are shown in the Table 3.18

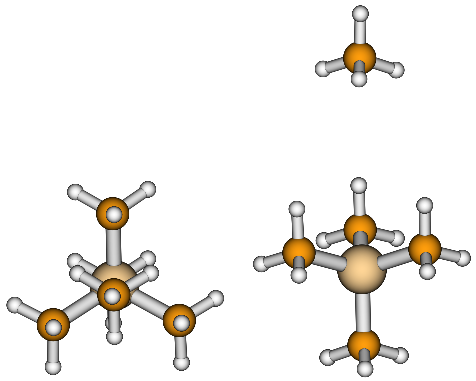

(a) $\boldsymbol{C_{3v}}$-*3* (b) $\boldsymbol{C_{3v}}$-*3*

Figure 3.39: $Si(CH_4)_4$–CH_4 interaction with $\boldsymbol{C_{3v}}$-*3* symmetry

Table 3.18: Energies of $Si(CH_4)_4$–CH_4 $\boldsymbol{C_{3v}}$-*3* symmetry

C-C$_{\text{Distance}}$/(Å)	**E**$_{\text{Not corrected}}$/(Kcal/mol)	**E**$^{\text{CP}}_{\text{corrected}}$/(Kcal/mol)
3.80000	1.29347614687867	1.41585973187466
3.90000	0.73695915919961	0.83190571260639
4.00000	0.37327841483057	0.44397604287951
4.20000	0.03617404453689	0.06684822439638
4.40000	0.00000000000000	0.00000000000000
4.60000	0.10159351315815	0.07953662450745
4.80000	0.25182063539978	0.21383861727009
5.00000	0.40586052223807	0.35561027650692
5.20220	0.54691616387572	0.48744371922658
5.40000	0.66366570757236	0.59713444230874
5.60000	0.76049355283612	0.68812025851366
5.80000	0.83797347481595	0.76149307817104
6.00000	0.90034949540859	0.82006359487423
6.20000	0.94954374717781	0.86624759570987
6.40000	0.98834931361489	0.90257014055896
7.00000	1.06513712089508	0.97371670793655

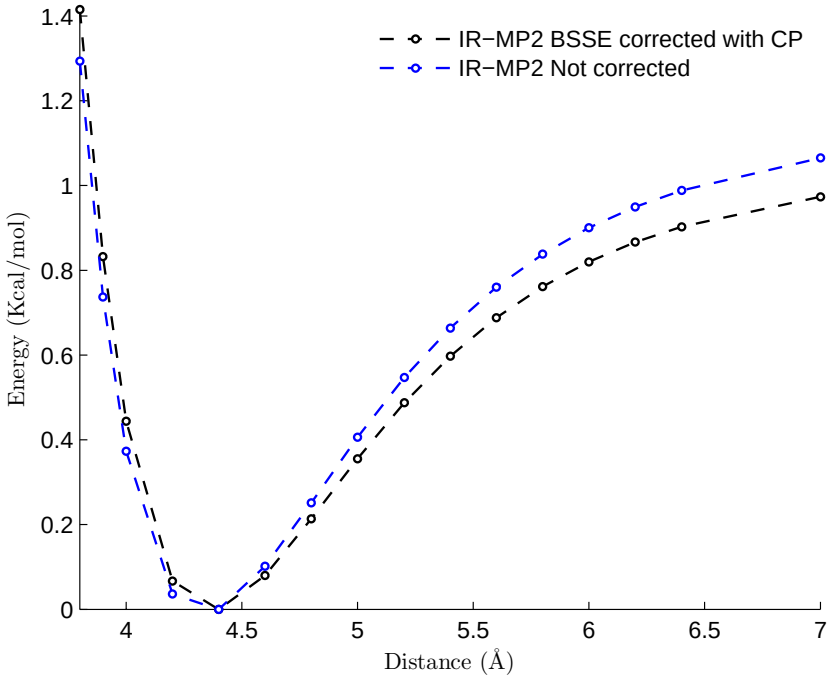

Figure 3.40: Energies of $Si(CH_4)_4$–CH_4 $\boldsymbol{C_{3v}}$-*3* symmetry

3.4.4 $Si(CH_4)_4$–CH_4-SYN2 with C_{3v}-*4* symmetry

For each structure the **IR-MP2** calculation method was applied, then the BSSE was corrected using the *C*P method 2.1. The structure used to perform this calculation is shown in Figure 3.41. The data is plotted in the Figure 3.42. The values obtained after normalization are shown in the Table 3.19

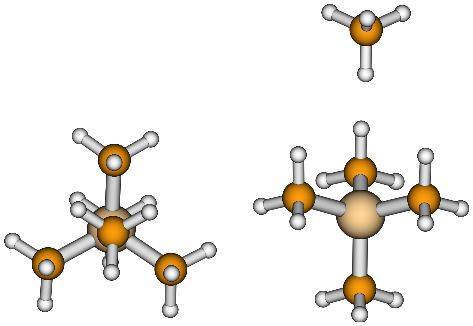

(a) $\boldsymbol{C_{3v}}$-*4* (b) $\boldsymbol{C_{3v}}$-*4*

Figure 3.41: $Si(CH_4)_4$–CH_4 interaction with $\boldsymbol{C_{3v}}$-*4* symmetry

Table 3.19: Energies of $Si(CH_4)_4$–CH_4 C_{3v}-*4* symmetry

C-C$_{\text{Distance}}$/(Å)	**E**$_{\text{Not corrected}}$/(Kcal/mol)	**E**$^{\text{CP}}_{\text{corrected}}$/(Kcal/mol)
3.20000	16.62647107755760	17.09358309866000
3.40000	9.45806616632035	9.79976253463610
3.60000	5.07821662386414	5.32255038573203
3.80000	2.50573936413275	2.67443491126323
4.00000	1.08357586001512	1.19237391976639
4.20000	0.36845283792354	0.43053253272592
4.40000	0.06952129869023	0.09610147337298
4.60053	0.00000000000000	0.00000000000000
4.80000	0.04715634050081	0.02806436017636
5.00000	0.14428960531950	0.11084668164767
5.20000	0.25530823966255	0.21106799625341
5.40000	0.36108781164512	0.30826112636714
5.60000	0.45394855435006	0.39447574735459
6.60000	0.71780255419435	0.64113538253878
7.50000	0.79942827578634	0.71679864586986

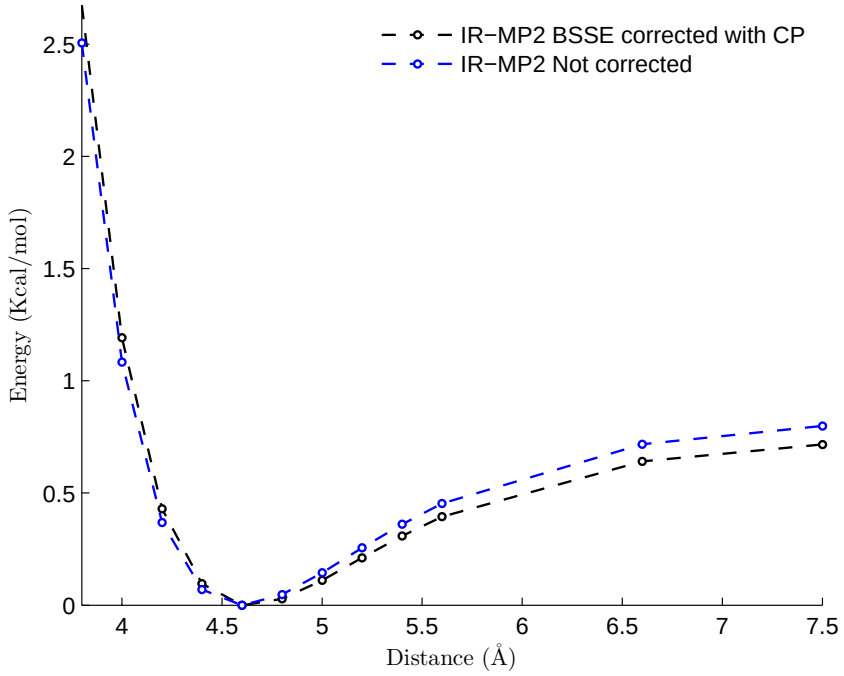

Figure 3.42: Energies of $Si(CH_4)_4$–CH_4 C_{3v}-*4* symmetry

3.4.5 Fitting Quantum Mechanics to a Force Field

The MP2 results were fitted into a Force Field with a Morse Type Potential equation 2.4. The four geometries (see Figure 3.34) were used to obtain the best fitting for these configurations. The parameters obtained are shown in Table 3.20. Energies of the Force Field against Quantum Mechanics results are shown in Figure 3.44 and in Figure 3.43

Table 3.20: Parameters from Fitting equation 2.4 in $Si(CH_4)_4$–CH_4

Term	$\mathbf{D}$/(Kcal/mol)	$\mathbf{r_0}$/(Å)	$\boldsymbol{\alpha}$
Si_{COF}—H_{CH_4}	0.1094	4.05745	7.18911
Si_{COF}—C_{CH_4}	0.08555	4.77968	16.5125

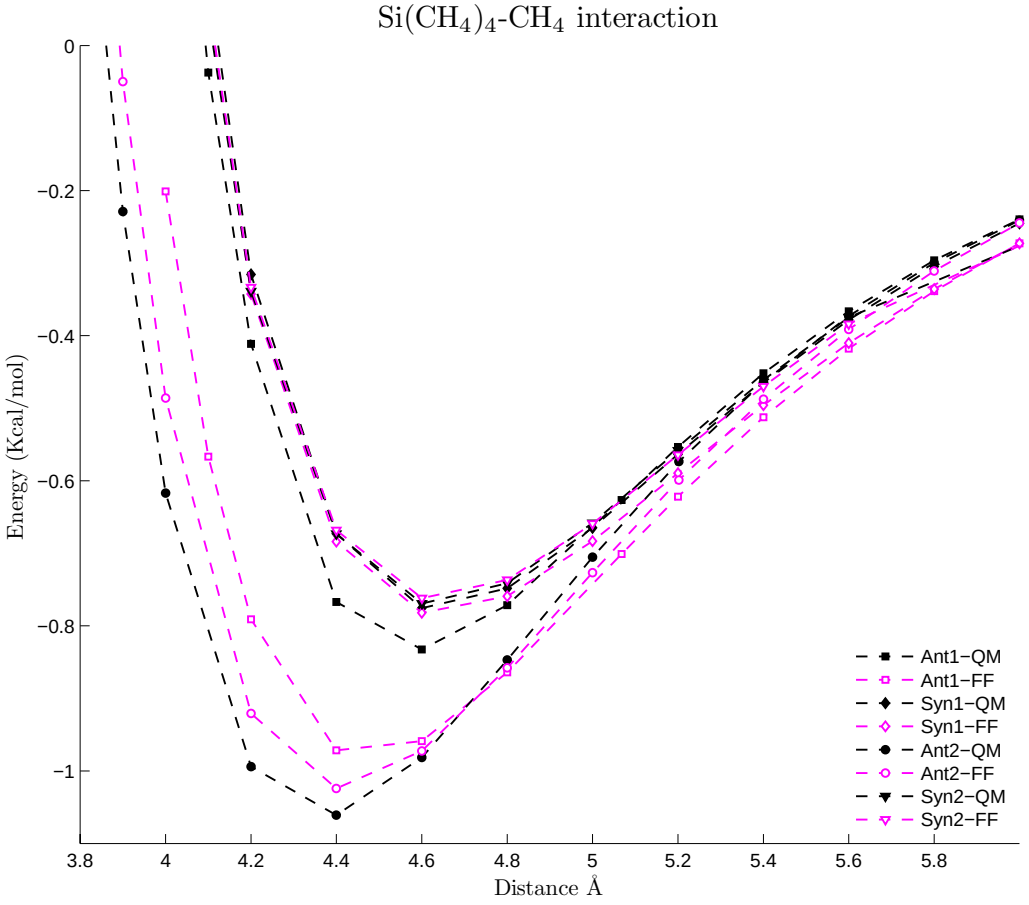

Figure 3.43: Force Field against MP2 results

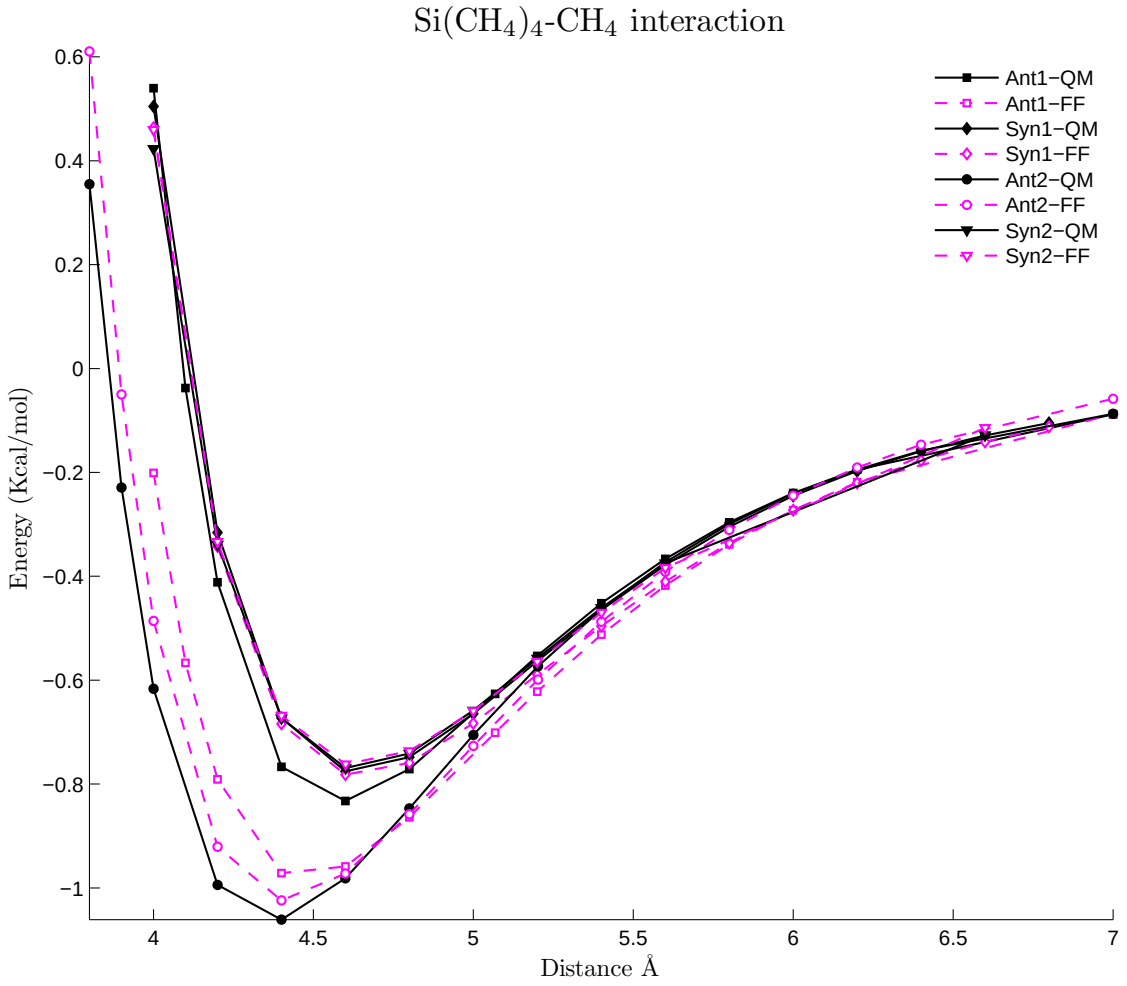

Figure 3.44: Force Field against MP2 results

Chapter 4

Validation against experiments

4.1 Prediction of CH_4 Density

The parameters developed in this study from first principles are presented. The energies predicted from the developed FF is compared against Quantum Mechanical results. The agreement is excellent.The complete Force Field parameters are shown in Table 4.1 and it was developed step by step in the previous sections. The parameters are in good agreement with the quantum mechanical results (i.e. MP2). It has to be noticed that this parameters are just considering *non covalent interaction* or *van der Waals interactions*. The rest of energetic consideration like: bond stretch, angle bend, torsions and inversions are shown in the appendix A. Nomenclature and definitions are based on Dreiding Force Field [29]. However when simulations are performed the framework is frozen so just non-covalent forces are important.

In order to validate our theoretical results from the developed Force Field we performed calculations of density of methane at different temperatures. Our results are graphed in Figure 4.1. The numerical results are shown in Table 4.2. The experimental results were obtained from the National Institute of Standards and Technology (NIST) Standard Reference Database [30]. According to our calculations the developed *ab initio* Force Field allows a very good prediction of the densities of Methane in temperatures and pressure ranges which are of interest for this work, i.e. 200-400K and 0-10MPa. As it can be seen our theory predicts experimental results both for gaseous and supercritical methane. It should be noticed that units for density (ρ_0) expressed in mol/L as it is reported by NIST database.

In Figure 4.1 the important pressure values for the simulation are shown: 10, 1.0 and 0.1 MPa. At 10 MPa the agreement is not so good in the range of 260-290 K, this can be due to the supercritical state of methane at these conditions. Supercritical fluids have more long term forces that are not taking into account for the GCMC code. In GCMC code the cut off is of 18 Åfor electrostatic and van der Waals forces, however in a more condensed phase like a supercritical fluid this cut off should be

Table 4.1: Parameters from Fitting equation 2.4 in $Si(CH_4)_4$–CH_4

Term	**D**/(Kcal/mol)	$\mathbf{r_0}$/(Å)	$\boldsymbol{\alpha}$
C_{CH_4}—C_{CH_4}	0.07672	3.92295	12.69130
H_{CH_4}—H_{CH_4}	0.00321	3.12660	11.42550
C_{CH_4}—H_{CH_4}	0.05212	3.45922	11.01982
C_{COF}—C_{CH_4}	0.04983	4.22836	13.24927
H_{COF}—C_{CH_4}	0.00088	3.25038	12.01304
O_{COF}—C_{CH_4}	0.04824	3.59396	11.26448
B_{COF}—C_{CH_4}	0.04651	4.11300	12.28580
C_{COF}—H_{CH_4}	0.11441	3.08342	9.07362
H_{COF}—H_{CH_4}	0.00088	3.26230	12.04535
O_{COF}—H_{CH_4}	0.09212	2.54864	8.99322
B_{COF}—H_{CH_4}	0.09174	3.27898	11.71868
Si_{COF}—H_{CH_4}	0.10940	4.05745	7.18911
Si_{COF}—C_{CH_4}	0.08555	4.77968	16.51250

increased. The purpose of this study is methane sorption into COFs at 298K in the range of 0-80 bar because these are the experimental characteristics that can be achieved with current high pressure instruments. If the cut off of the calculations is increased so do calculation time, as this condition are above practical criteria our simulation gives pretty good results for a practical purpose. As it was mentioned before GCMC steps for these simulations were of 10,000,000, but if simulations steps are increased a better agreement is not observed for this case, so the cut off argument is a plausible explination if the code needs to be refined for future applications. In Figure 4.1 simulations 1.0MPa in the range of 200-400 K are also shown, it can be observed that agreement between experiment and theory are very good. Error bar are necessary for this case and more simulations should be performed to ensure validation of this precision. Finally in Figure 4.1 results about 0.1MPa are shown. For this case the agreement is not as good as 1.0MPa case, this could be explained because of the short cut off condition of the GCMC code. Even tough methane is in a gas state at these conditions the cut off should be increased to get a better correlation with experiments. The cut off increment increase substantially calculation time and in COFs the small size nature of the pores makes this long distance forces not to be important. With current conditions, prediction of methane density is very acceptable with current GCMC code and our first principles developed force field.

4.1.1 Details about Density calculations

In order to calculate the density of Methane at different temperatures and pressure the Grand Canonical Monte Carlo method was applied. The parameter from our

Table 4.2: Density of CH_4 at 0.1, 1.0 and 10 MPa from theory and experiments

10 MPa			
Temp. / (K)	Theoretical ρ / (mol/L)	Exp.(NIST) ρ / (mol/L)	State
260.00	4.679917	6.296300	Supercritical
290.00	4.002667	4.980000	Supercritical
320.00	3.533481	4.214600	Supercritical
350.00	3.194655	3.693900	Supercritical
400.00	2.756505	3.100200	Supercritical
1.0 MPa			
Temp. / (K)	Theoretical ρ / (mol/L)	Exp.(NIST) ρ / (mol/L)	State
200.00	0.643038	0.643630	gas
230.00	0.559154	0.545810	gas
260.00	0.500044	0.475870	gas
290.00	0.456013	0.422780	gas
320.00	0.420448	0.380840	gas
350.00	0.401953	0.346750	gas
400.00	0.353699	0.302050	gas
0.1 MPa			
Temp. / (K)	Theoretical ρ / (mol/L)	Exp.(NIST) ρ / (mol/L)	State
200.00	0.120539	0.060518	Vapor
230.00	0.108739	0.052508	Vapor
260.00	0.099213	0.046387	Vapor
290.00	0.091523	0.041552	Vapor
320.00	0.084582	0.037635	Vapor
350.00	0.079141	0.034395	Vapor
400.00	0.071110	0.030082	Vapor

Force Field were used. A empty box of 20x20x20 Åwas used. The cut off for this simulations as the others was 10 Å. The cut off for the van der Waals calculations was min(8);max(10). For the GCMC process 10,000,000 steps were used and stabilization energy was monitored. As it can be seen from these considerations, the empty box should contain at least twice the cut off used during the simulation. This is obvious since periodical consitions are imposed so in order to avoid periodical effects lenght in every coordinate should be at least of 16 Å.

Stabilization studies are essential to have an idea of the number of steps that required to reach equilibrium. With GCMC equilibration properties are obtained and the minimun/maximum number of steps needed are essential to have the best

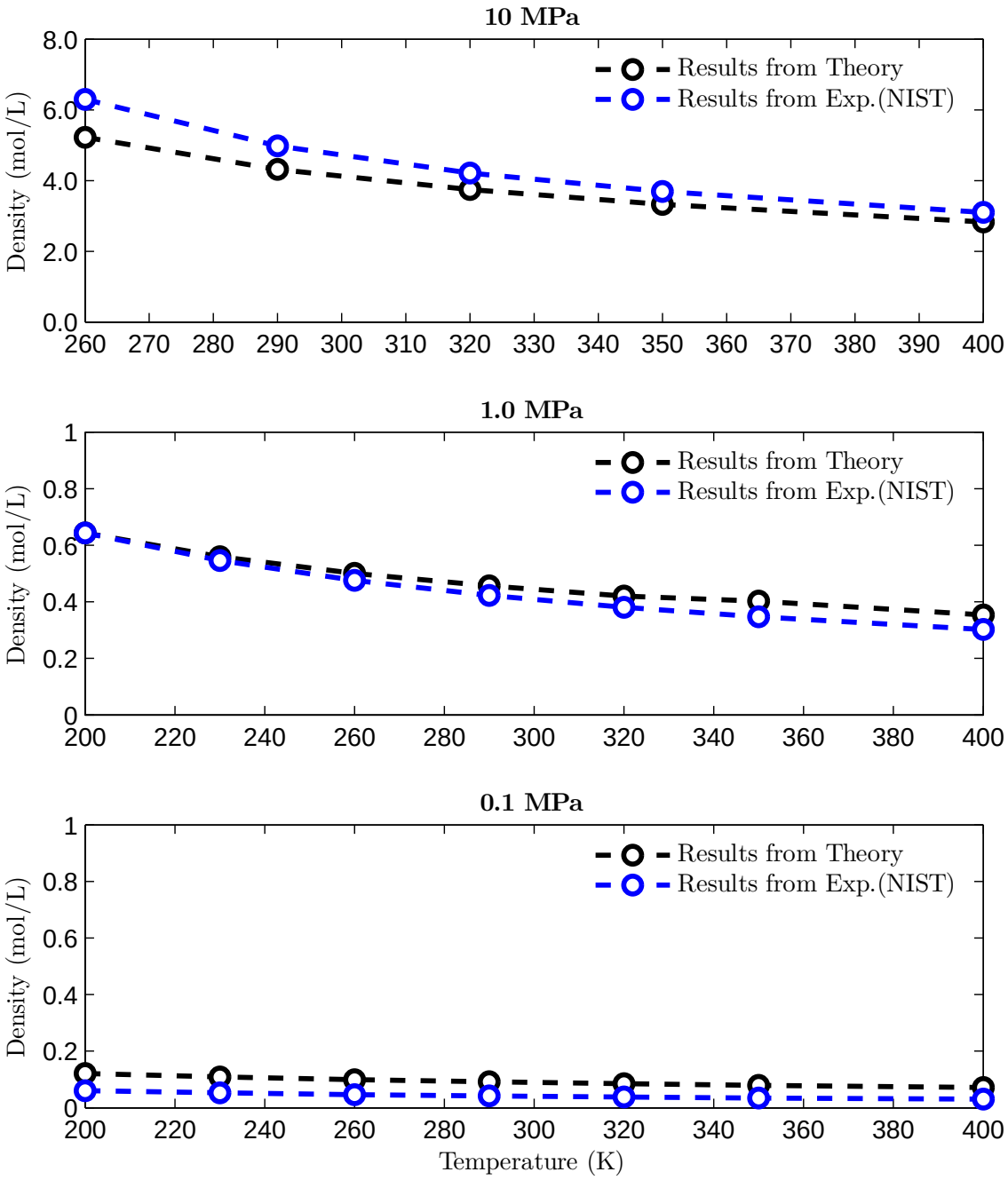

Figure 4.1: Experimental vs Theoretical Density of CH_4

ratio of efficiency to accuracy. During the course of this investigation stabilization studies were performed.

4.2 Sorption experiments

COFs were synthesized in University of California, Los Angeles (UCLA). The materials were characterized first with Powder X-Ray Diffraction (PXRD), and then compared with simulated patterns. In this way crystallinity and structure of the framework is examined. It is worth to mention that crystallinity is directly related to the width of the PXRD peak, so in this process this characteristic is covered. The next step is to clean out pores of COFs to remove starting materials and solvent. In order to do this solvent exchange was used.

In this method a low boiling point and high vapor pressure solvent is added to the final product in a vessel and it is placed at 60-80 °C in a vacuum chamber with heating control during some predetermined time. There is not a general procedure to determine this heating-vacuum time; it is an error-try method. To obtain these optimal conditions the temperature should not be so high so the structure collapse and the time should be long enough to remove all solvent, but not to long so the experiment can be carried out in a practical time. The best pore volume and uptake values obtained from sorption experiments are the parameters to decide the best activation conditions. Changing periodically solvent with fresh one allow the new solvent take out starting materials and primary solvent out of the pores. The sample is place into a vacuum chamber with some heating. Generally speaking solvents used during synthesis have a high boiling point thus it is difficult to remove them, so without changing the solvent for a low boiling point one, the cleaning procedure of the pores would take a long time.

After the samples pass trough this process, surface area (S_A) and pore volume (V_p) of these materials were tested. These two concepts are used generally in the sorption field to characterized porous materials, however they differ in the theory behind them B. The surface area hypothesis is based in layer formation of the adsorbed gas and it was proposed for flat surfaces, while pore volume is based in a pore filling process and it is used for concave surfaces materials. Historically surface area has been used to compare materials, however for current porous materials where concave surfaces are obvious, surface area approach has become out of date. Pore filling has a theory that fits naturally to current porous materials and this concept will be the main parameter to compare COFs. Surface area were calculated experimentally and in theory for matching purpose and to examine the theory, *albeit of their inadequacy*.

The surface area parameter is one of the most representative quantities for characterizing novel porous materials because it is easy to calculate. The experimental BET analysis as the standard method for determination of surface area from N_2 adsorption isotherms is originally derived for multilayer gas adsorption onto flat surfaces. This experiment is performed at boiling point of the gas used, in the case of N_2 is 77.3 K while for Ar is 87.4 K. Using Connolly method or a solvent accessible method, the surface area of COFs can be calculated directly and quickly from crystal structures. The Connolly surface area is calculated by considering the bottom of an adsorbate

molecule rolling along the surface of COFs, while the solvent accessible surface area is calculated by considering the center of mass of an adsorbate probe. Also through a similar method we can easily calculate free volume of COFs. Discrepancies between calculated and the BET surface areas can be used to judge the quality of the experimental sample. Another reason that could explain this differences is the possible presence of solvent molecules or there is not a complete periodicity in the sample.

Not all materials were examined at high pressure conditions since this process is really expensive. The most promising synthesized materials where experimental results match those from theory were evaluated. V_p is the parameter of interested since more molecules are presented. At high pressure the gas used to measure this quantity was He. Table 4.3 shows the parameters used for experiments during all this process.

Table 4.3: Parameters used for sorption experiments

Gas	Bath Temp./(K)	Cross section Area/(Å^2)	Molecular Weight/(g/mol)
N_2	77.3	16.2	28.0134
Ar	87.4	14.2	39.9480
He	4.3	11.7	4.0026

Once all COFs were synthesized and their crystallinity was checked with PXRD. The following process was to purify the pores with the procedure mentioned before. The pore volume and surface area were examined at low pressure. Since the ultimate purpose of these materials is to serve in high pressure condition the parameter to meet is V_p at both low and high pressure. In Figure 4.2 the parameters reached during experimentation are shown. As it can be observed that only COF-5 and COF-8 were optimized to reach the optimal pore volume values at high and low pressure range. Black circles are landmarks used to calibrate the machine and it proves the relation of pore volume in the full pressure range. Synthesis and V_p of landmarks have been fully optimized. The red points correspond to current synthesized COFs. As it can be inferred some COFs have not been fully optimized and their results can not be used for comparison against theory. Because of this reason COF-5 and COF-8 were the only ones used to compare against our theory.

4.2.1 Prediction of CH_4 Uptake in COF-5

As it was shown in section 4.2 the best samples for sorption at high pressure were COF-5 and COF-8. The values of pore volume at high and low pressure match pretty well, in the high pressure region (≈1-100 bar) He is used while at low pressure ($\leq$ 1 bar) Ar is used. The structural features of COF-5 are shown in Figure 4.3. COF-5 has homogeneous pores of 27 Å, and in this samples the measured surface was

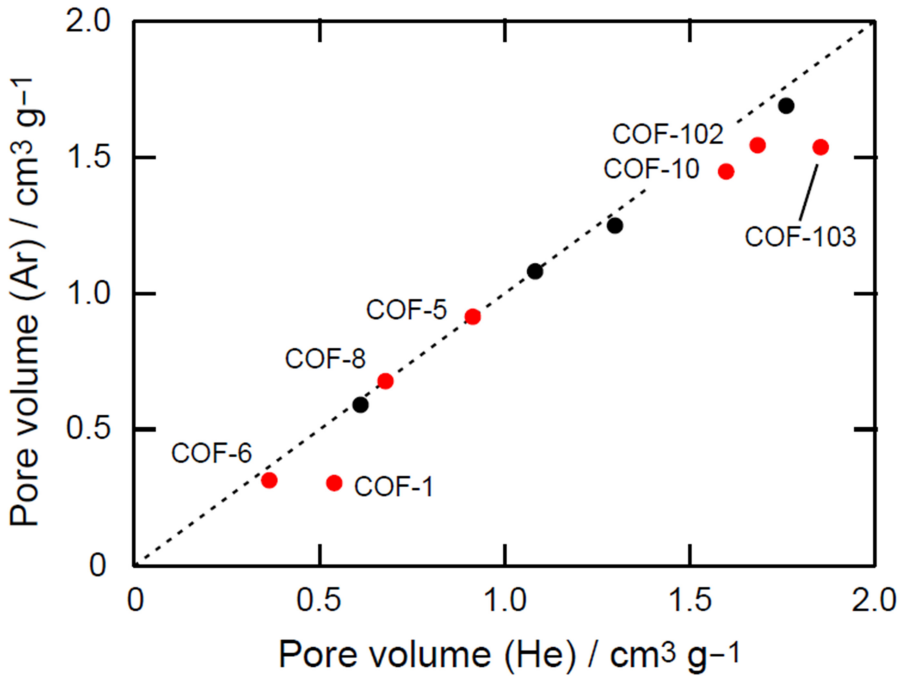

Figure 4.2: Experimental Pore volume of COFs syntesized heretofore. Black circles are landmarks

of 1670 m^2/g. COF-5 has a space group of $P6/mmm$. In Figure 4.3 van der Waals representations can be observed on part *a*) while part *b*) shows a more chemical based representation. The experimental procedure for synthesizing COF-5 is almost the same as literature procedure [14], but with the only difference that the post-handling material were under inert atmosphere. This careful handling under inert atmosphere (Ar or N_2 atmosphere) was proposed after realizing that the boroxine ring could suffer attack from moisture presented in air. The hypothesis was proved to be right, because the surface area and pore volume were higher when the same activation conditions were used. All these precautions result into confident experimental results where they matched with theoretical results. It is important to mention that when theoretical results are mentioned, they are referred to calculations where ideal structures were used to apply the algorithms to know both surface area and pore volume.

After verifying that experimental results were trustful the next step was to undertake the samples to high pressure measurements. Also simulations were per-formed in COF-5 with the methodology described in section 2. Data obtained is presented in Table 4.4 and plotted properly in Figure 4.4. In this table gravimetric and volumetric units were included. The experimental data is generally given in mg of gas/g of framework. It should be remembered that COF-5 has a boron nitride topology **bnn**.

In the sorption field, it is common to express gravimetric units as wt % instead of (mg of gas)/(g of framework) or (g of gas)/(g of framework). In this work wt % will be used to make comparisions among different COFs. In equation 4.1 wt % is

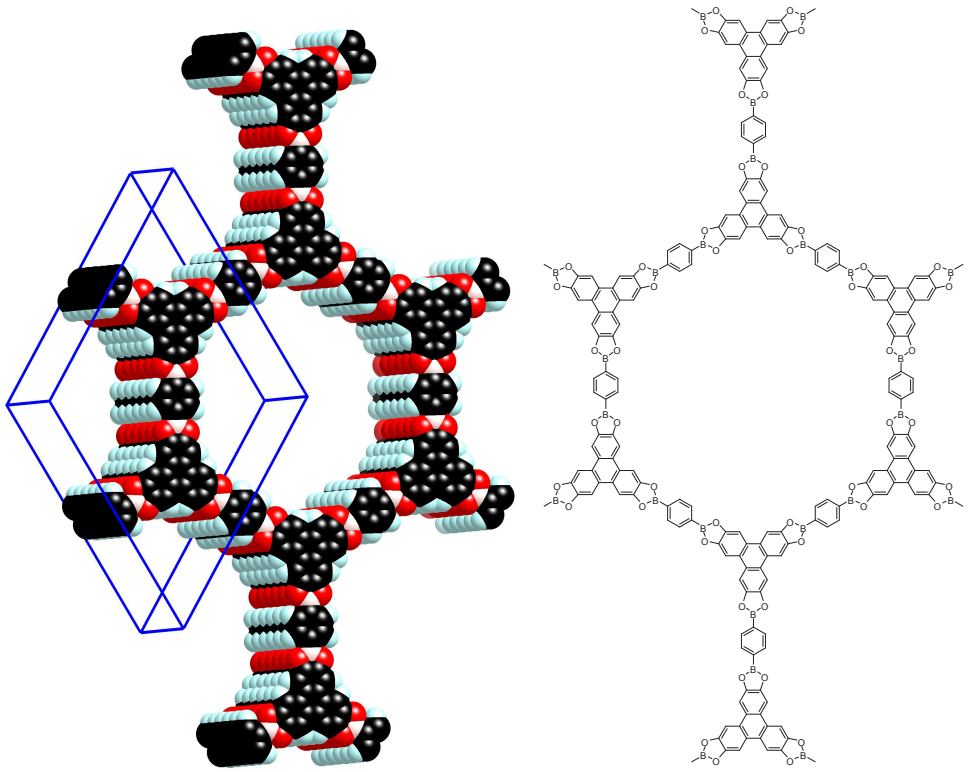

(a) COF-5 structure (b) COF-5 structure

Figure 4.3: COF-5 structural characteristics

defined. All this conversion values are shown in Table 4.4

$$wt\ \% = \frac{Gas}{Gas + Framework} \times 100 \tag{4.1}$$

In calculating volumetric units (g/L) density of the ideal crystal structure was taken into account, this assumption is correct since we know the structure from PXRD and surface area and pore volume fits to those from theory.

$$wt\ \% = \frac{g\ gas}{g\ Framework} \times \rho\ (framework) \tag{4.2}$$

4.2.2 Prediction of CH_4 Uptake in COF-8

The values of pore volume at high and low pressure match pretty well for COF-8, in the high pressure region (≈1-100 bar) He is used while at low pressure ($\leq$ 1 bar) Ar is used. The structural features of COF-8 are shown in Figure 4.5. COF-8 has homogeneous pores of 16.4 Å, considering the crystal structure, it has a pore diam-

Table 4.4: Experimental data obtained for COF-5

p/(bar)	COF-5/(mg/g)	COF-5/(g/g)	COF-5_{exc}/(wt %)	COF-5_{exc}/(g/L)
0.00047	0.00000	0.00000	0.00000	0.00000
1.34705	6.94632	0.00695	0.68984	4.03634
2.69442	13.86171	0.01386	1.36722	8.05471
6.56524	27.29562	0.02730	2.65704	15.86083
9.98978	37.89533	0.03790	3.65117	22.02007
13.05288	46.65148	0.04665	4.45721	27.10805
16.69862	55.46021	0.05546	5.25460	32.22659
19.98807	62.93122	0.06293	5.92054	36.56782
23.20147	69.79618	0.06980	6.52425	40.55689
26.42516	75.87403	0.07587	7.05232	44.08858
30.35341	82.55317	0.08255	7.62578	47.96967
32.97836	86.73871	0.08674	7.98156	50.40178
36.81080	91.70329	0.09170	8.40002	53.28658
39.97278	95.90074	0.09590	8.75086	55.72562
44.17954	100.85055	0.10085	9.16115	58.60184
48.63234	105.34897	0.10535	9.53083	61.21576
52.73198	108.59427	0.10859	9.79567	63.10153
59.28709	113.97805	0.11398	10.23162	66.22991
65.62778	118.21692	0.11822	10.57191	68.69301
72.00250	122.27542	0.12228	10.89531	71.05131
78.40632	124.85299	0.12485	11.09949	72.54907
84.83669	127.20621	0.12721	11.28509	73.91648
78.55090	124.29378	0.12429	11.05528	72.22413
69.82009	120.57171	0.12057	10.75984	70.06133
60.21586	114.35484	0.11435	10.26198	66.44886
51.75362	107.31080	0.10731	9.69112	62.35573
42.19439	98.45015	0.09845	8.96264	57.20702
33.15395	87.98736	0.08799	8.08717	51.12735
23.75789	70.54472	0.07054	6.58961	40.99184
14.67448	51.48978	0.05149	4.89684	29.91947
8.13659	33.26423	0.03326	3.21933	19.32904
4.06194	19.59510	0.01960	1.92185	11.38624
2.02715	11.04912	0.01105	1.09284	6.42038

eter of 18.7 Åby fitting non-local density functional theory models to experimental isotherms [19]. To the best samples surface area was measured with a value of 1400 m^2/g. COF-8 has a boron nitride structure(**bnn**) were layers are "eclipsed" and it has space group $P6/mmm$.

Table 4.5: Theoretical data obtained for COF-5

Press /(KPa)	Press /(bar)	Total /(wt)%	Excess /(wt)%	Total /(g/L)	Excess /(g/L)
0	0	0.00000	0.00000	0.00000	0.00000
100	1	0.63578	0.56992	3.71806	3.33068
200	2	1.16767	1.03718	6.86530	6.09003
300	3	1.69464	1.50073	10.01700	8.85333
400	4	2.17130	1.91491	12.89703	11.34443
500	5	2.66592	2.34826	15.91547	13.97341
1000	10	4.74996	4.13758	28.97754	25.08041
2000	20	7.72508	6.56076	48.64705	40.80017
3000	30	9.82728	8.13798	63.32789	51.47755
4000	40	11.35570	9.15092	74.43894	58.53035
5000	50	12.72469	10.01867	84.72133	64.69855
6000	60	13.72826	10.51388	92.46636	68.27229
7000	70	14.65355	10.93535	99.76875	71.34509
8000	80	15.54279	11.32670	106.93733	74.22455
9000	90	16.31462	11.59593	113.28292	76.22023
10000	100	16.92336	11.68674	118.37078	76.89609

In Figure 4.5 van der Waals representations can be observed on part *a*) while part *b*) shows a more chemical based representation. After verifying that experimental results were trustful the next step was to undertake the samples to high pressure measurements. Also simulations were performed in COF-8 with the methodology described in section 2. Data obtained from this process is presented in Table 4.6 and they are graphed properly in Figure 4.6. The experimental data is generally given in mg of gas/g of framework. Once again the units for gravimetric and volumetric uptake were used. wt % for gravimetric uptake and g CH_4/L for volumetric uptake. Definitions of these quantities were shown previously in equation 4.1 and in equation 4.2. COF-8 has the same topology as COF-5, they have a carbon nitride topology **bnn**. Co-condensation reactions between the building blocks: 2,3,6,7,10,11-hexahydroxytriphenylene (HHTP) and 1,3,5-benzenetris(4-phenylboronic acid) produced COF-8 with chemical formulas of $C_{14}H_7BO_2$ [19]. To generate COF-8 formation of C_2O_2B rings create the dymanic covalent bonds necessary for proper crystallization.

The experimental procedure for synthesizing COF-8 is almost the same as literature procedure [19], but with the only difference that the post-handling material were under inert atmosphere. This careful handling under inert atmosphere (Ar or N_2 atmosphere) because of reasons presented above in section 4.2.1. All these precautions result into confident experimental results where they matched with theoretical results, so COF-8 results were considered to validate our theoretical results.

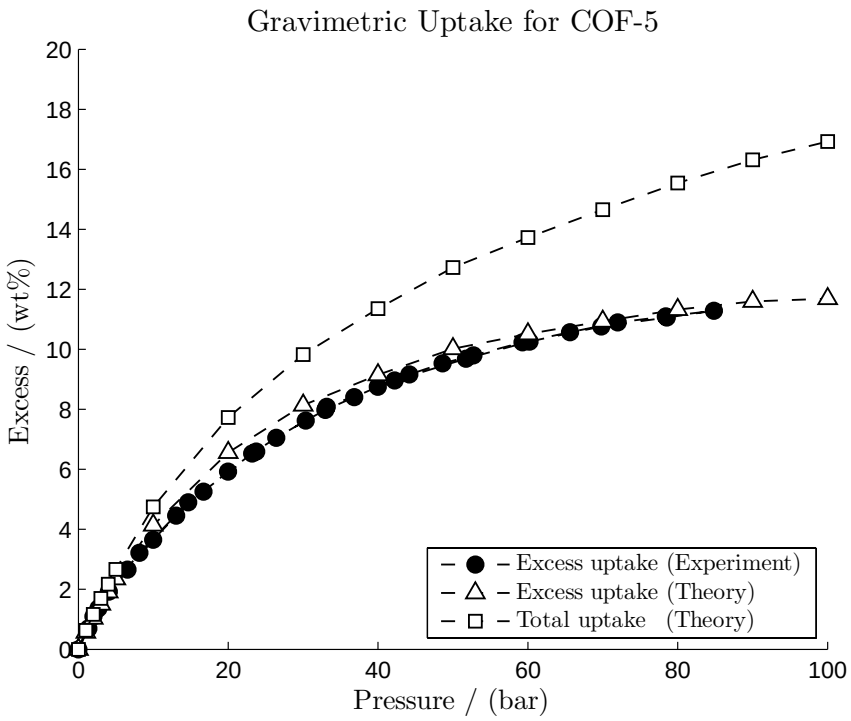

(a) Gravimetric uptake for COF-5

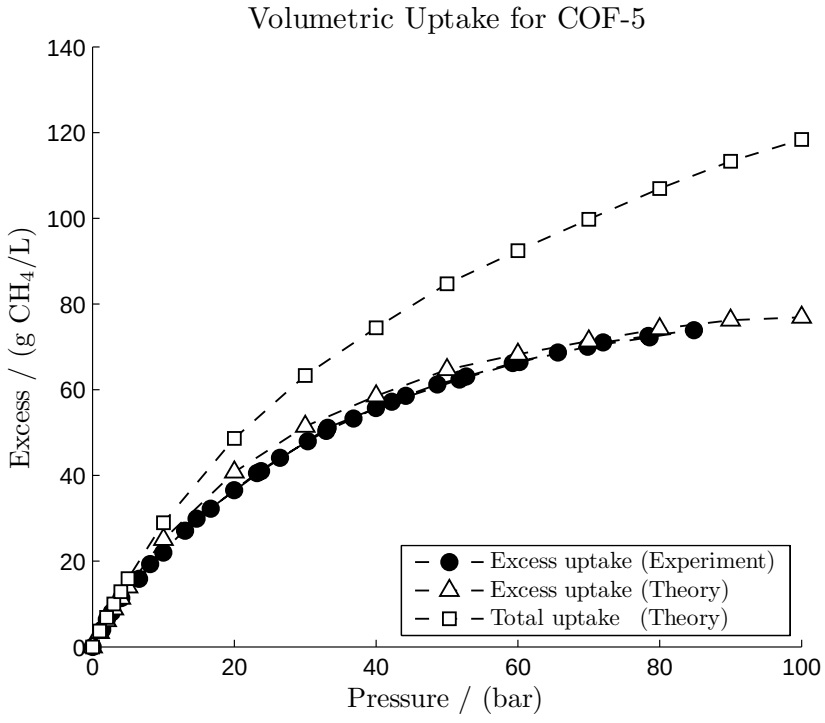

(b) Volumetric uptake for COF-5

Figure 4.4: Experimental vs theoretical results for COF-5

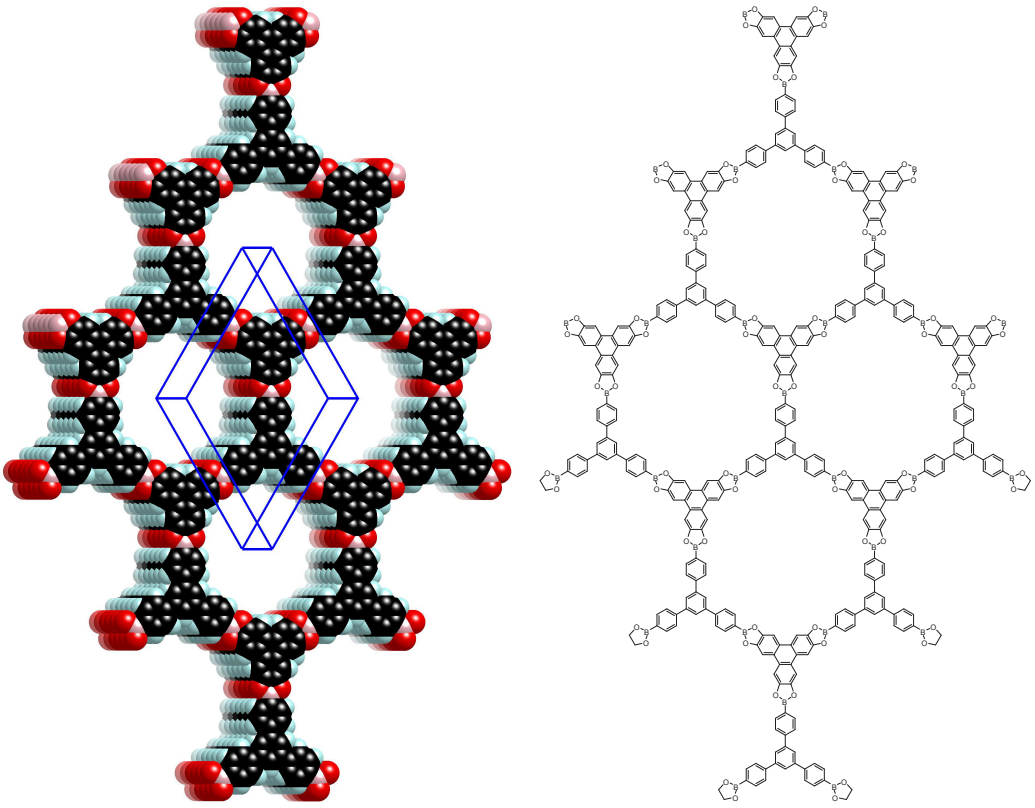

(a) COF-8 structure (b) COF-8 structure

Figure 4.5: COF-8 structural characteristics

In graph 4.6 the fitting between experimental and theoretical results it is not as good as the COF-5 case in the region of 10 to 60 bar. This could be due to an experimental error. As it is well known this kind of experiments are done just once and the experimental error is latent at least this measurement is done at least three times. An inclusion of an error bar would give a better understanding of this affirmation, however this was not done and these are the only results obtained for this case. The really important part of this comparison is the maximum uptake which both experiment and simulation agree pretty well (see Figure 4.6)

4.2.3 More experimental parameters

To complete the comparison analysis calculations of Pore Volume, Surface Area and Density were performed in both theory and experiment. This data can be observed in Table 4.8. In order to calculate experimentally Pore Volume the Dubinin-Radushkevitch model (DR) was used. To calculate Surface Area the BET model was used. In determining density the ideal crystal structure was used. As it can be observed the agreement is very good.

Table 4.6: Experimental data obtained for COF-8

p/(bar)	COF-8/(mg/g)	COF-8/(g/g)	COF-8$_{exc}$/(wt %)	COF-8$_{exc}$/(g/L)
0.00063	0.00000	0.00000	0.00000	0.00000
1.34988	5.85301	0.00585	0.58190	4.17303
2.69074	10.41287	0.01041	1.03056	7.42408
6.71595	25.20121	0.02520	2.45817	17.96775
9.90081	35.39188	0.03539	3.41821	25.23342
13.33762	45.08651	0.04509	4.31414	32.14542
16.68676	54.26448	0.05426	5.14714	38.68905
19.95682	61.61534	0.06162	5.80392	43.93001
23.16193	68.38912	0.06839	6.40114	48.75953
26.26993	73.96339	0.07396	6.88696	52.73382
30.64587	81.10964	0.08111	7.50244	57.82890
35.70726	88.01065	0.08801	8.08913	62.74913
39.93977	92.84927	0.09285	8.49607	66.19893
46.37792	98.94867	0.09895	9.00394	70.54763
52.83319	103.66438	0.10366	9.39274	73.90980
59.12908	107.31546	0.10732	9.69150	76.51292
65.57471	109.78991	0.10979	9.89286	78.27713
71.92999	111.87397	0.11187	10.06175	79.76301
78.33886	113.22923	0.11323	10.17124	80.72927
85.04760	114.31558	0.11432	10.25882	81.50381
78.51829	113.22014	0.11322	10.17051	80.72279
69.57184	111.93794	0.11194	10.06692	79.80862
60.62433	108.19152	0.10819	9.76289	77.13753
51.71873	103.34913	0.10335	9.36686	73.68503
42.39615	95.87745	0.09588	8.74892	68.35794
33.50055	85.44171	0.08544	7.87161	60.91755
24.25604	70.77840	0.07078	6.61000	50.46302
17.17178	55.56214	0.05556	5.26375	39.61425
12.06509	42.00340	0.04200	4.03102	29.94725
8.09125	29.73082	0.02973	2.88724	21.19724
4.74493	18.09447	0.01809	1.77729	12.90085
2.01670	7.60658	0.00761	0.75492	5.42328

Table 4.7: Theoretical data obtained for COF-8

Press /(KPa)	Press /(bar)	Total /(wt)%	Excess /(wt)%	Total /(g/L)	Excess /(g/L)
0	0	0.00000	0.00000	0.00000	0.00000
100	1	0.70420	0.63973	5.05644	4.59056
200	2	1.21807	1.09030	8.79169	7.85931
300	3	1.75307	1.56324	12.72214	11.32266
400	4	2.27011	2.01934	16.56147	14.69428
500	5	2.75740	2.44666	20.21727	17.88175
1000	10	4.89744	4.29922	36.71607	32.02969
2000	20	7.94962	6.81454	61.57437	52.13960
3000	30	9.97556	8.32652	79.00524	64.75883
4000	40	11.41852	9.26279	91.90646	72.78387
5000	50	12.57667	9.91862	102.56923	78.50463
6000	60	13.44612	10.27946	110.76162	81.68785
7000	70	14.14074	10.45823	117.42590	83.27440
8000	80	14.82261	10.62659	124.07358	84.77437
9000	90	15.38473	10.66485	129.63435	85.11602
10000	100	15.93571	10.69066	135.15705	85.34667

Table 4.8: Parameters from theory and experiment for COF-5 and COF-8

Material	S_{BET} / m^2 g^{-1}	V_p^{DR} / cm^3 g^{-1}	ρ_{bulk} / g cm^{-3}
COF-5 (Exp)	1670	1.07	0.58
COF-8 (Exp)	1350	0.69	0.71

Material	S_A / m^2 g^{-1}	V_p / cm^3 g^{-1}	ρ / g cm^{-3}
COF-5 (Theory)	1681.9856	0.8601	0.5811
COF-8 (Theory)	1540.3660	0.5386	0.7130

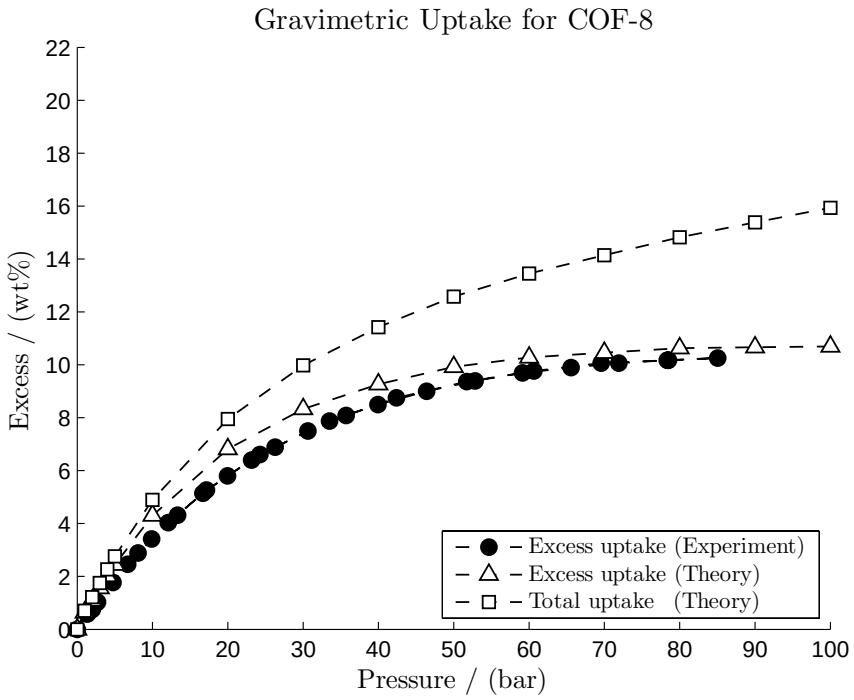

(a) Gravimetric uptake for COF-8

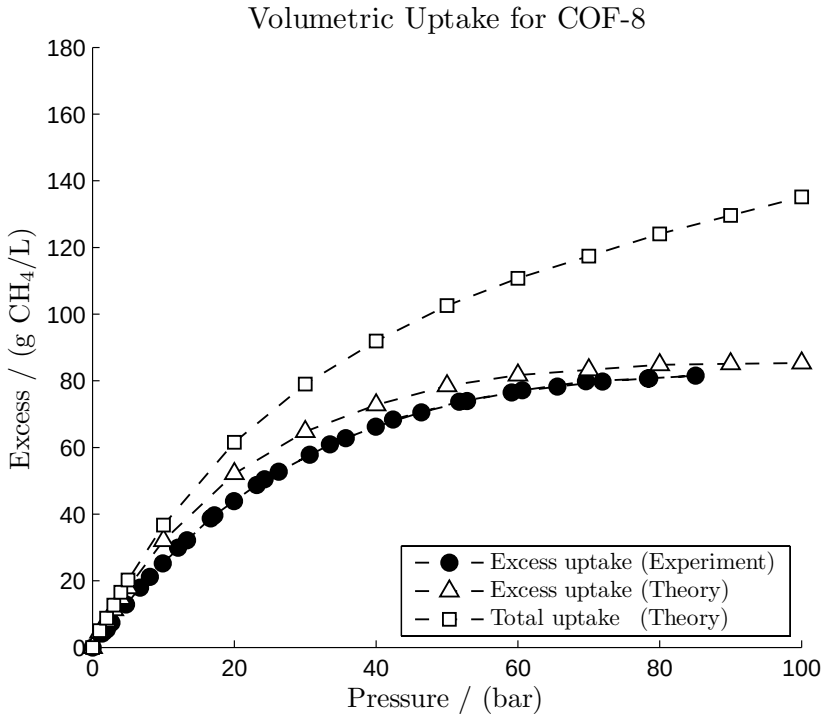

(b) Volumetric uptake for COF-8

Figure 4.6: Experimental vs theoretical results for COF-8

Chapter 5

Application to real and hypothetical COFs

5.1 Studies in COF-1

COF-1 is the first member of the Covalent Organic Frameworks family. It is the only member of COF family so far in having **gra** topology where graphitic layers are stagered and it has space group $P6_3/mmc$. All the theory developed before was applied into adsorption studies of methane into COF-1 accesible pores. In the following sections data about sorption steps and Qst values (ΔH^{ads})are presented.

5.1.1 Methane adsorption in COF-1

COF-1 has the crystal structure shown in Figure 5.1. The most important insight from this simulations are the observations of sorption steps. A snapshot was taken at the equilibration step of every pressure, these are exposed in Figure 5.2. GCMC simulations were performed with 3,000,000 steps using the Force Field developed in previous sections and explicitly shown in appendix A.

Sorption experimental data at high pressure is not currently available for COF-1, however this methodology can be applied to attain this data. Once again with this theoretical approach an important quantity is accessible: total amount of gas. As it was mentioned in section 4.2 with experiment this is not easily possible. Simulation data is presented in Table 5.1 and is graphed in Figure 5.4. At 20 bar saturation has been reached, as it can be observed in Figure 5.2 too.

For the case of COF-1 an interesting phenomena was observed, total uptake was almost the same as excess uptake. This is due most probably to the pore diameter of COF-1, in the xy plane is 15 Å and 6.6 Å in yz plane without taking in account van der Waals radii. However if a sphere is placed between layers the diameter is of 9.6 Å

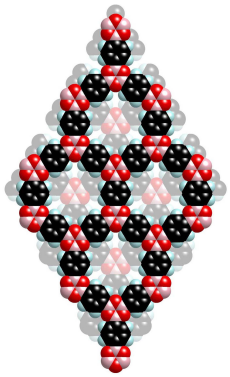

Figure 5.1: COF-1 structure

taking into account van der Waals radii, from now on van der Waals considerations will be used (See Figure 5.3). However if a sphere is placed between layers the diameter in the same pore is of 4.0 Å(yz plane). In order to calculate the excess uptake in the GCMC code, the attraction forces are suppressed and the intrinsic cut off of this force makes radii of the pore even shorter and thus almost inaccessible. So when the simulations to estimate excess uptake were carry out without attractive force between the framework and the gas, the uptake was almost cero. This is a critical example but it is expected that this do not affect uptake estimation.

Table 5.1: Theoretical data obtained for COF-1

Press /(KPa)	Press /(bar)	Total /(wt)%	Excess /(wt)%	Total /(g/L)	Excess /(g/L)
0	0	0.00000	0.00000	0.00000	0.00000
100	1	3.00618	3.00618	33.49555	33.49555
200	2	5.27277	5.27277	60.15617	60.15616
300	3	6.77352	6.77351	78.52188	78.52186
400	4	7.87922	7.87922	92.43609	92.43606
500	5	8.48465	8.48464	100.19722	100.19718
1000	10	9.69534	9.69533	116.02956	116.02948
2000	20	10.35215	10.35214	124.79769	124.79755
3000	30	10.57398	10.57396	127.78812	127.78791
4000	40	10.67102	10.67100	129.10098	129.10070
5000	50	10.72149	10.72147	129.78493	129.78457
6000	60	10.77887	10.77884	130.56343	130.56300
7000	70	10.79296	10.79292	130.75465	130.75415
8000	80	10.82549	10.82545	131.19666	131.19609
9000	90	10.86005	10.86001	131.66657	131.66593
10000	100	10.89563	10.89558	132.15061	132.14990

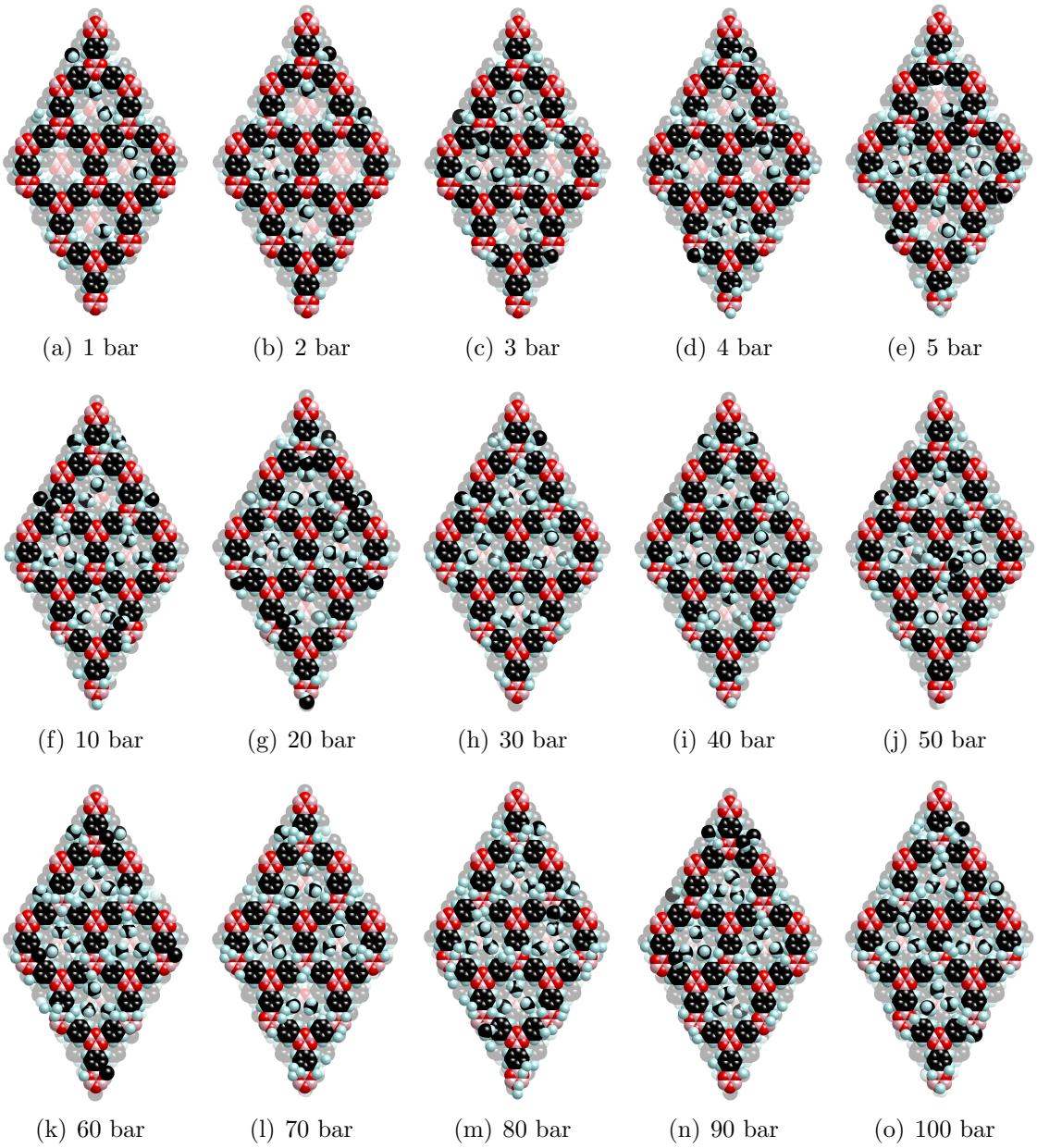

(a) 1 bar (b) 2 bar (c) 3 bar (d) 4 bar (e) 5 bar

(f) 10 bar (g) 20 bar (h) 30 bar (i) 40 bar (j) 50 bar

(k) 60 bar (l) 70 bar (m) 80 bar (n) 90 bar (o) 100 bar

Figure 5.2: COF-1 sorption steps

5.1.2 Qst values for methane in COF-1

Qst or ΔH^{ads} is the energy liberated in the sorption process, thus the bigger values more favorable is the process. It has been observed that in the case of H_2 sorption values decreased with pressure thus more hydrogen do not collaborate to absorb more gas. Typical values for H_2 sorption in Metal-Organic Frameworks are 10-5 KJ/mol around 77K [31]. These characteristics are quite different for methane in COFs were values range from 8-25 KJ/mol at 298 K. The most interesting phenomena is that during the sorption process of methane into COFs the Qst values increase with

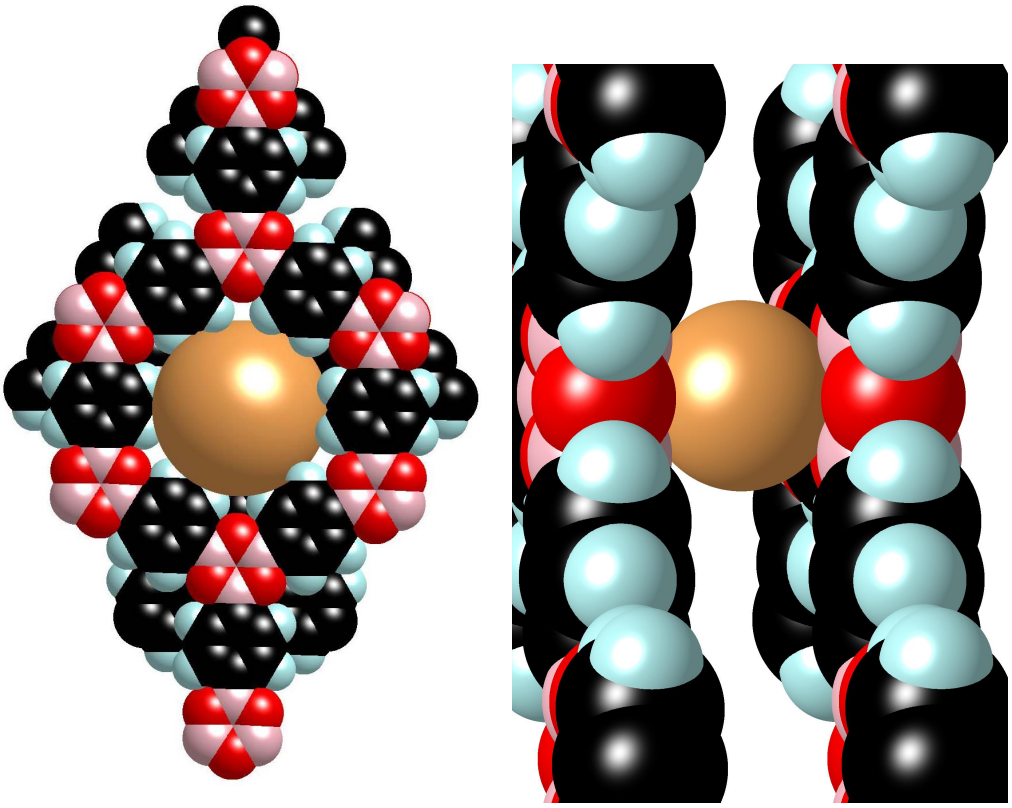

(a) xy plane for COF-1 (b) yz plane for COF-1

Figure 5.3: COF-1 pore aperture estimation. a)AB layers are shown b) Layer A is not shown

pressure; therefore molecules of methane absorbed into the surface collaborate to absorb more methane molecules. This interesting behavior is because of polarization. During simulation it was observed that charges of methane changes when interacting with the framework, so the first molecules absorbed molecules are polarized and this help to other methane molecules to absorb. For hydrogen this polarization process is very difficult to reach because of the very neutral nature of the molecule. The values obtained are shown in Table 5.2 and they are graphed in Figure 5.5

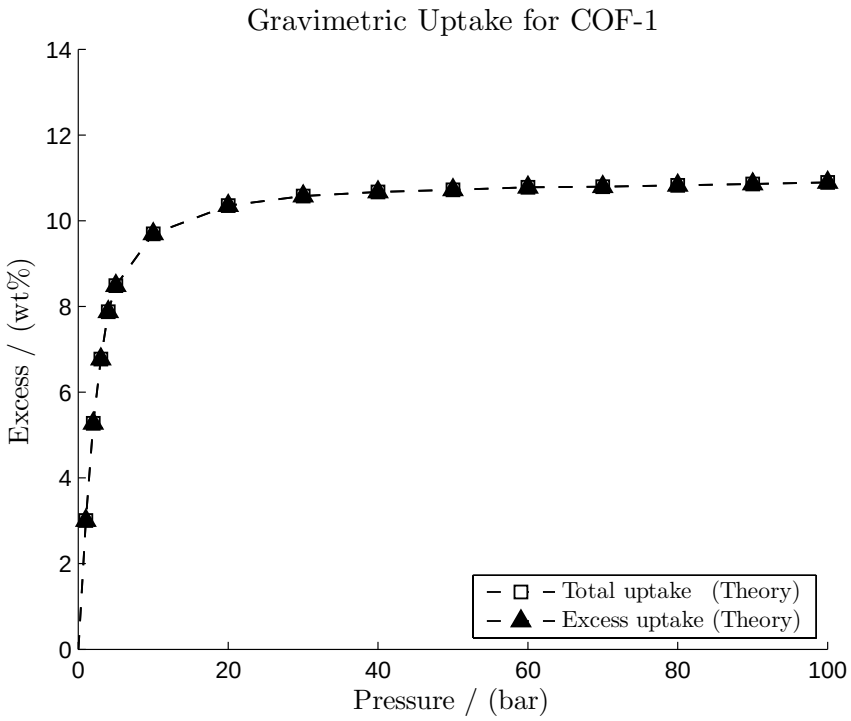

(a) Gravimetric uptake for COF-1

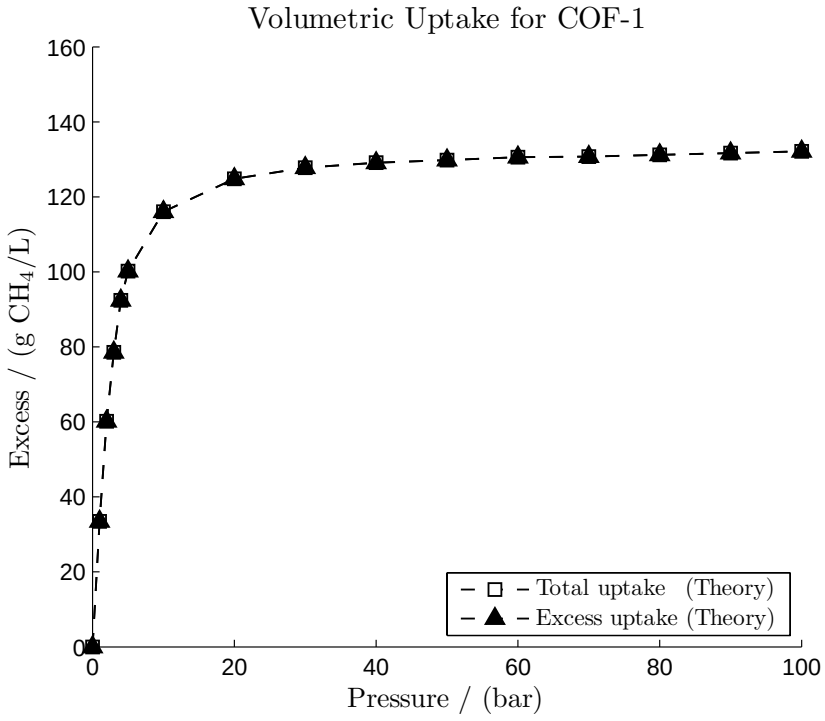

(b) Volumetric uptake for COF-1

Figure 5.4: Theoretical results for COF-1

Table 5.2: Qst values obtained from theory for COF-1

Pressure /(bar)	Qst /(Kcal/mol)	Qst /(KJ/mol)
1	5.73716	24.00428
2	5.82905	24.38875
3	5.89435	24.66196
4	5.93499	24.83200
5	5.95943	24.93426
10	6.01179	25.15333
20	6.04361	25.28646
30	6.04975	25.31215
40	6.05556	25.33646
50	6.05752	25.34466
60	6.06216	25.36408
70	6.06098	25.35914
80	6.05953	25.35307
90	6.06003	25.35517
100	6.06253	25.36563

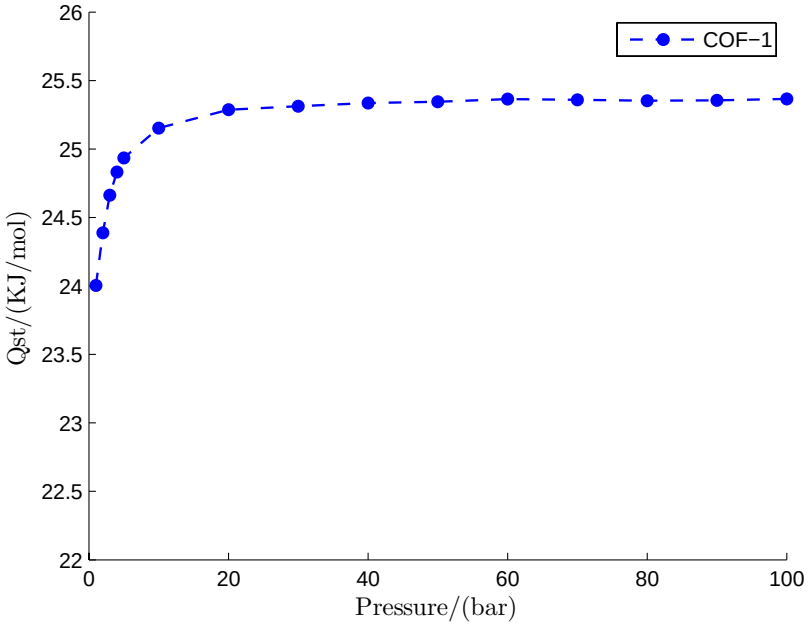

Figure 5.5: Qst values obtained from theory for COF-1

5.2 Studies in COF-5

COF-5 is the second member of the Covalent Organic Frameworks family synthesized. It has the **bnn** topology where graphitic layers are eclipsed and space group $P6/mmm$. All the theory developed before was applied into adsorption studies of methane into COF-5 cylindrical pores. In the following sections data about sorption steps and Qst values (ΔH^{ads})are presented.

5.2.1 Methane adsorption in COF-5

COF-5 has the crystal structure shown in Figure 4.3. COF-5 is the second member ever synthesized of the COF family. The most important insight from this simulations are the observations of sorption steps. A snapshot was taken at the equilibration step of every pressure, these are exposed in Figure 5.6. GCMC simulations were performed with 3,000,000 steps using the Force Field developed in previous sections and explicitly shown in appendix A. Experimental and theoretical data was shown in section 4.2.1 for COF-5.

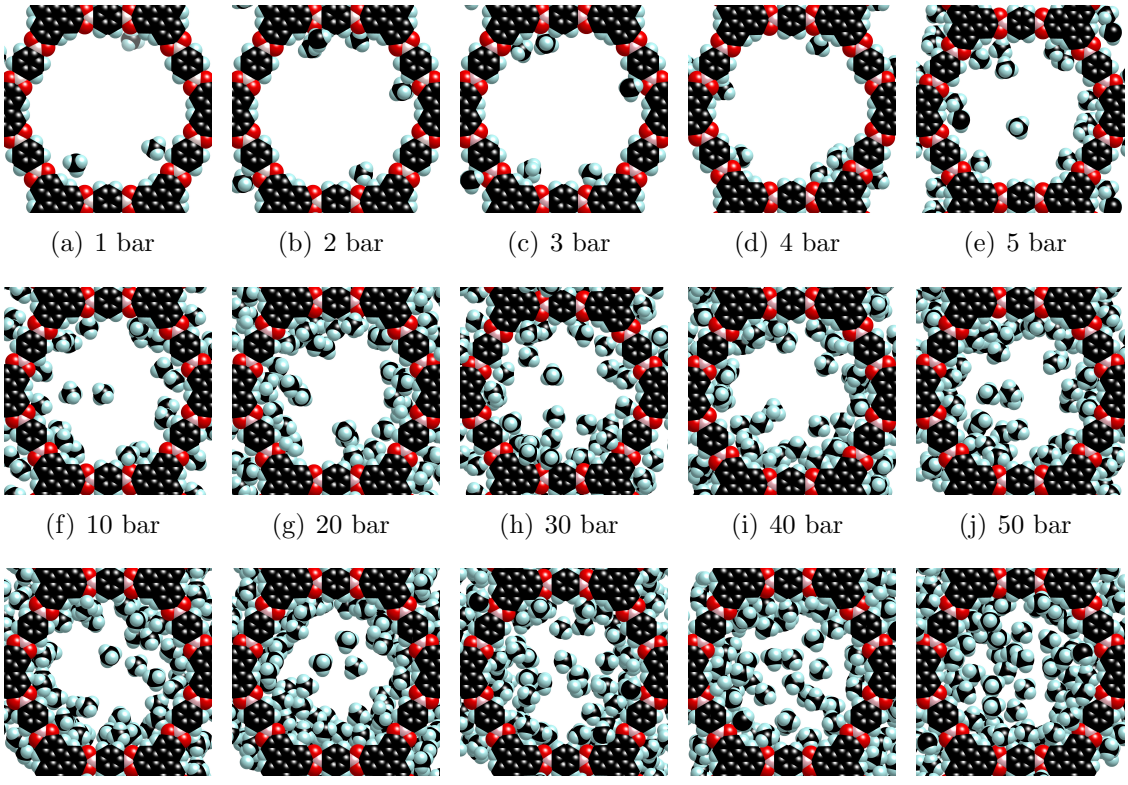

(a) 1 bar (b) 2 bar (c) 3 bar (d) 4 bar (e) 5 bar

(f) 10 bar (g) 20 bar (h) 30 bar (i) 40 bar (j) 50 bar

(k) 60 bar (l) 70 bar (m) 80 bar (n) 90 bar (o) 100 bar

Figure 5.6: COF-5 sorption steps

5.2.2 Qst values for methane in COF-5

Qst or ΔH^{ads} is the energy liberated in the sorption process, thus bigger values more favorable is the process. For COF-5 this values are 12-11 KJ/mol at 298K which are much better that H_2 in MOFs. For COF-5 the increment with pressure was not observed. This is probably because of a bigger pore aperture; 24.4 Å. Figure 5.7 shows how a sphere is placed in the cylindrical pore to estimate the pore aperture with van der Waals radii. These bigger pores make that the next layers of methane do not effectively help the next molecules to adhere to the surface; the potential surface is not efficient. Because of this a COFs with a proper pore diameter for methane should be found. COF-5 potential surface should be useful for a bigger gas such as ethylene. The values obtained are shown in Table 5.3 and they are graphed in Figure 5.8

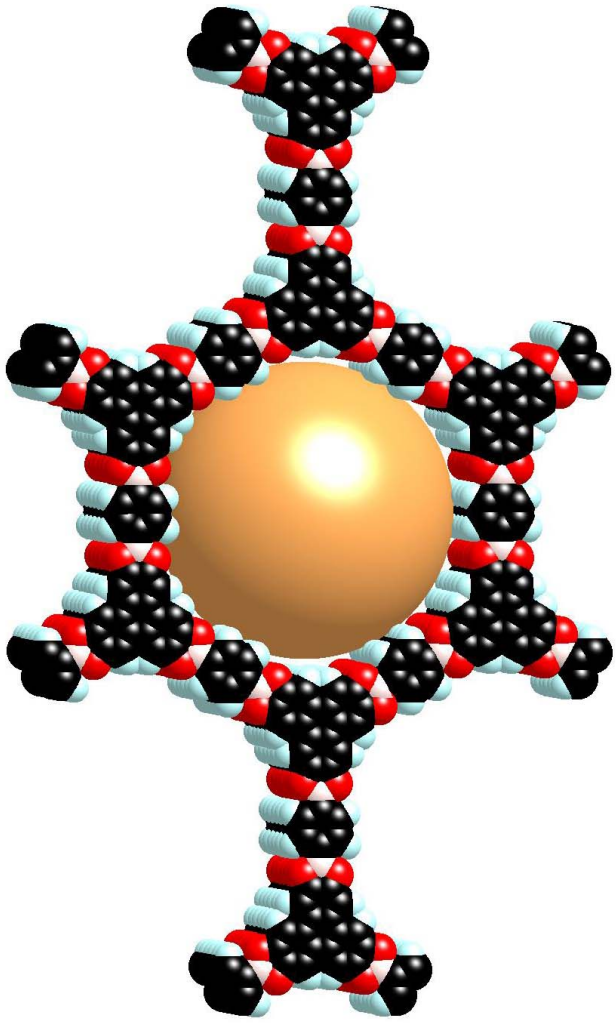

Figure 5.7: COF-5 pore aperture estimation

Table 5.3: Qst values obtained from theory for COF-5

Pressure /(bar)	Qst /(Kcal/mol)	Qst /(KJ/mol)
1	2.88101	12.05415
2	2.89326	12.10540
3	2.89666	12.11963
4	2.88376	12.06565
5	2.89459	12.11096
10	2.89960	12.13193
20	2.88532	12.07218
30	2.86043	11.96804
40	2.82896	11.83637
50	2.81660	11.78465
60	2.78043	11.63332
70	2.75942	11.54541
80	2.75321	11.51943
90	2.73062	11.42491
100	2.70369	11.31224

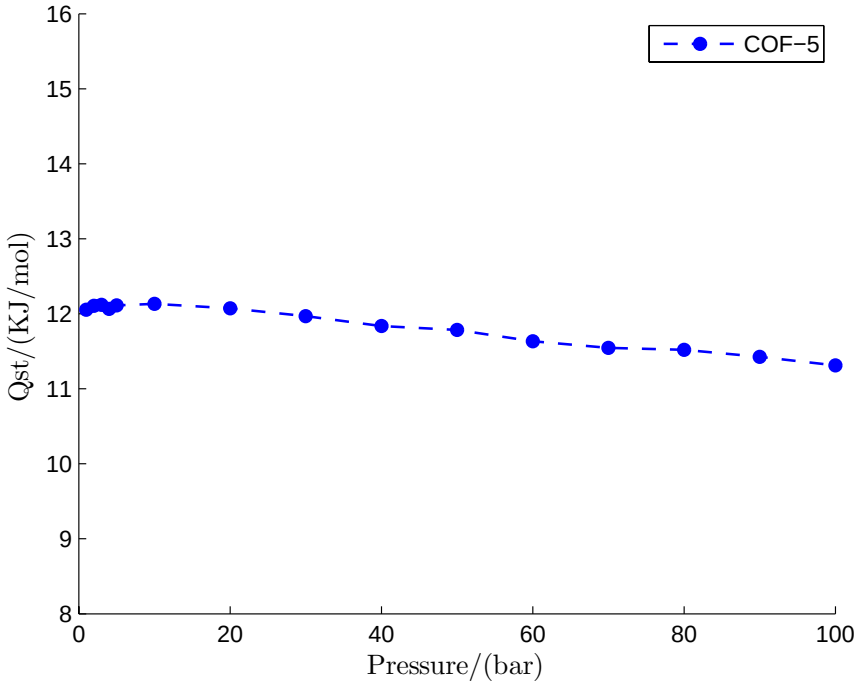

Figure 5.8: Qst values obtained from theory for COF-5

5.3 Studies in COF-6

COF-6 is produces from co-condensation reactions between 2,3,6,7,10,11-hexahydroxytriphenylene and 1,3,5-benzenetriboronic acid. COF-6 has the **bnn** topology where graphitic layers are eclipsed and space group $P6/mmm$. All the theory developed before was applied into adsorption studies of methane into COF-6 cylindrical pores. In the following sections data about sorption steps and Qst values (ΔH^{ads})are presented.

5.3.1 Methane adsorption in COF-6

COF-6 has the crystal structure shown in Figure 5.9. The most important insight from this simulations are the observations of sorption steps. A snapshot was taken at the equilibration step of every pressure, these are exposed in Figure 5.10. GCMC simulations were performed with 3,000,000 steps using the Force Field developed in previous sections and explicitly shown in appendix A.

Sorption experimental data at high pressure is not currently available for COF-6, however this methodology can be applied to attain this data. Once again with this theoretical approach an important quantity is accessible: total amount of gas. As it was mentioned in section 4.2 with experiment this is not easily possible or it is meaningless with current gravimetric instruments. Simulation data is presented in Table 5.4 and is graphed in Figure 5.11. At 60 bar saturation has been reached, this can also be observed in Figure 5.10.

From Figure 5.11 it can observed that in the range from 1-5 bar the sorption uptake is almost linear while from 20-100 bar the increment is of just 2 wt%, also this can be observed at the atomistic level in Figure 5.10. This behavior is expected for a pore of such aperture (See Figure 5.12), the optimal uptake take place when the surface is almost empty (1-2 bar) or when just some methane molecules are in the surface (2-5 bar) this makes the synergic effect greater and it is numerically observed in some way in the Qst values.

5.3.2 Qst values for methane in COF-6

Qst values for COF-6 range from 16.5 to 17 KJ/mol. COF-6 has the second best Qst values of all COFs presented in this study. This is probably because of an optimal the pore aperture; 9.1 Å. Figure 5.12 shows how a sphere is placed in the cylindrical pore to estimate the pore aperture with van der Waals radii. The values obtained are shown in Table 5.5 and they are graphed in Figure 5.13

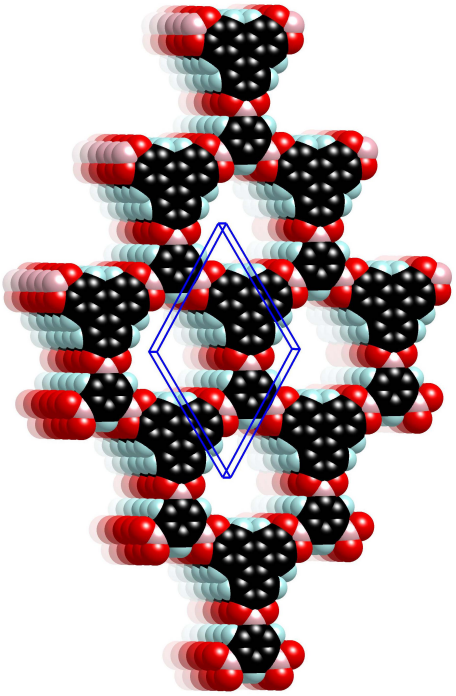

Figure 5.9: COF-6 structure

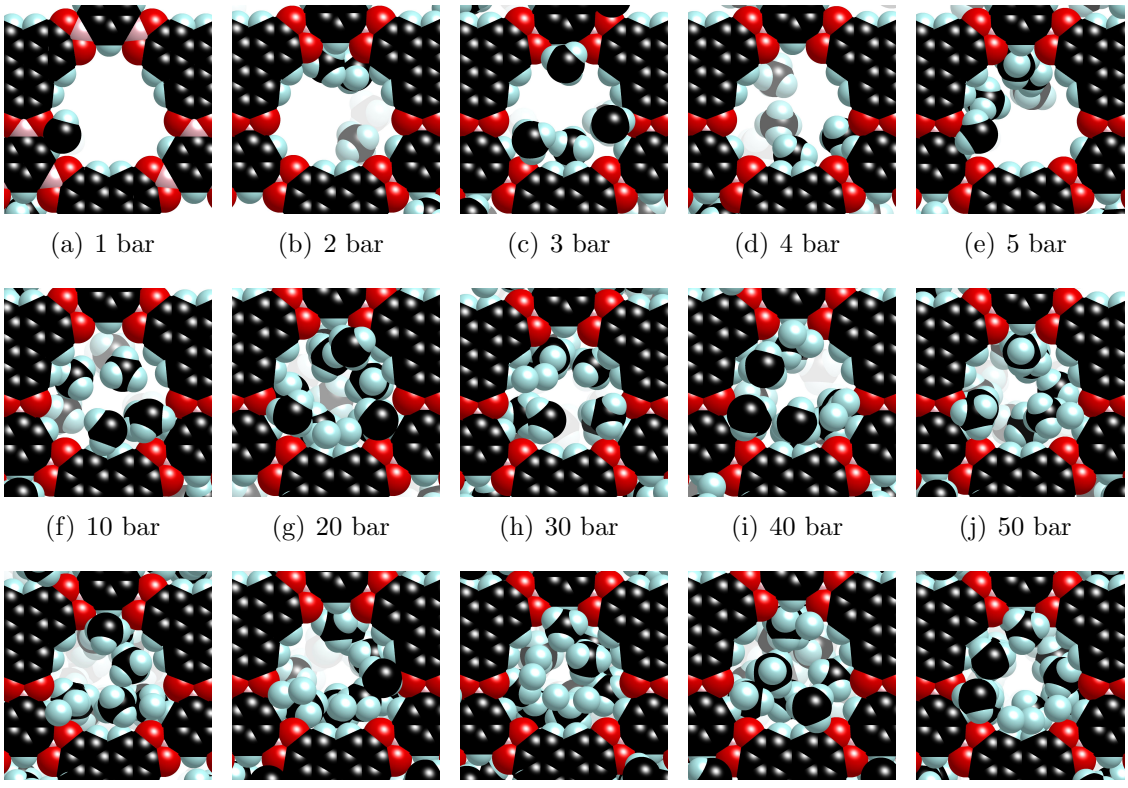

(a) 1 bar (b) 2 bar (c) 3 bar (d) 4 bar (e) 5 bar

(f) 10 bar (g) 20 bar (h) 30 bar (i) 40 bar (j) 50 bar

(k) 60 bar (l) 70 bar (m) 80 bar (n) 90 bar (o) 100 bar

Figure 5.10: COF-6 sorption steps

Table 5.4: Theoretical data obtained for COF-6

Press /(KPa)	Press /(bar)	Total /(wt)%	Excess /(wt)%	Total /(g/L)	Excess /(g/L)
0	0	0.00000	0.00000	0.00000	0.00000
100	1	1.09718	1.08172	11.40225	11.23983
200	2	2.02674	1.99639	21.26248	20.93758
300	3	2.81223	2.76741	29.74142	29.25400
400	4	3.46154	3.40256	36.85459	36.20459
500	5	4.05311	3.98028	43.41911	42.60648
1000	10	6.09843	5.95869	66.75264	65.12609
2000	20	8.32982	8.06266	93.39652	90.13827
3000	30	9.45002	9.05783	107.26727	102.37213
4000	40	10.22573	9.71019	117.07526	110.53803
5000	50	10.79202	10.15379	124.34313	116.15859
6000	60	11.30052	10.54109	130.94845	121.11133
7000	70	11.69894	10.81825	136.17698	124.68200
8000	80	11.95042	10.94661	139.50141	126.34327
9000	90	12.15978	11.03246	142.28368	127.45705
10000	100	12.34833	11.09736	144.80080	128.30032

Table 5.5: Qst values obtained from theory for COF-6

Pressure /(bar)	Qst /(Kcal/mol)	Qst /(KJ/mol)
1	3.94290	16.49709
2	3.95121	16.53186
3	3.96663	16.59638
4	3.96682	16.59717
5	3.96675	16.59688
10	3.99371	16.70968
20	4.03078	16.86478
30	4.04672	16.93148
40	4.06249	16.99746
50	4.06318	17.00035
60	4.08685	17.09938
70	4.09684	17.14118
80	4.08989	17.11210
90	4.10183	17.16206
100	4.11019	17.19703

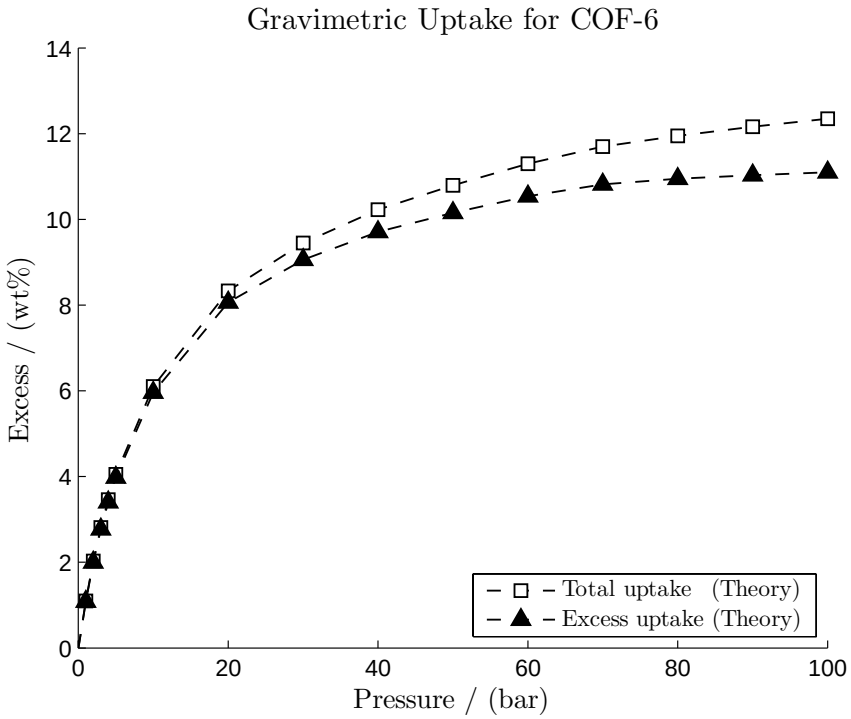

(a) Gravimetric uptake for COF-6

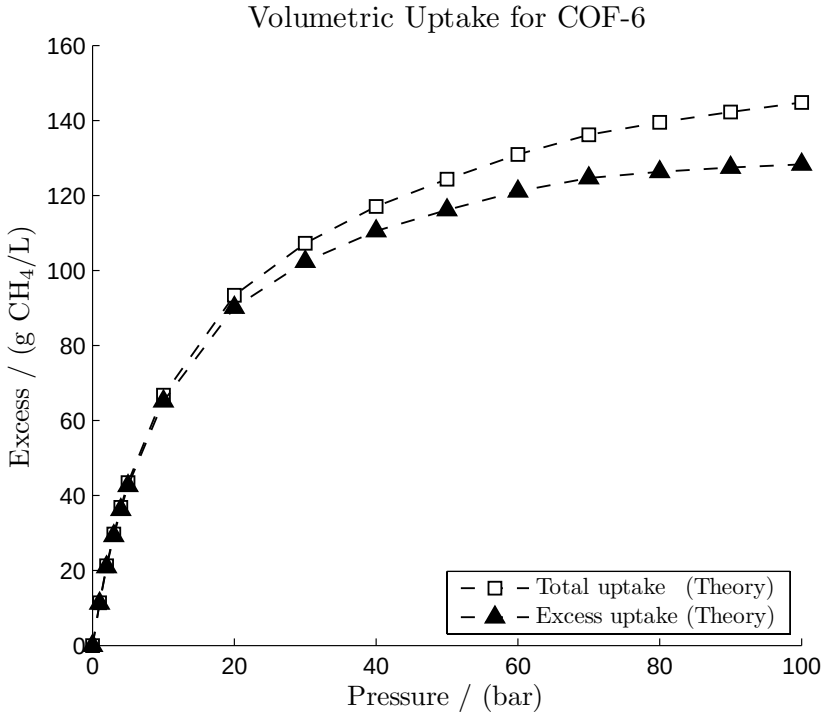

(b) Volumetric uptake for COF-6

Figure 5.11: Theoretical results for COF-6

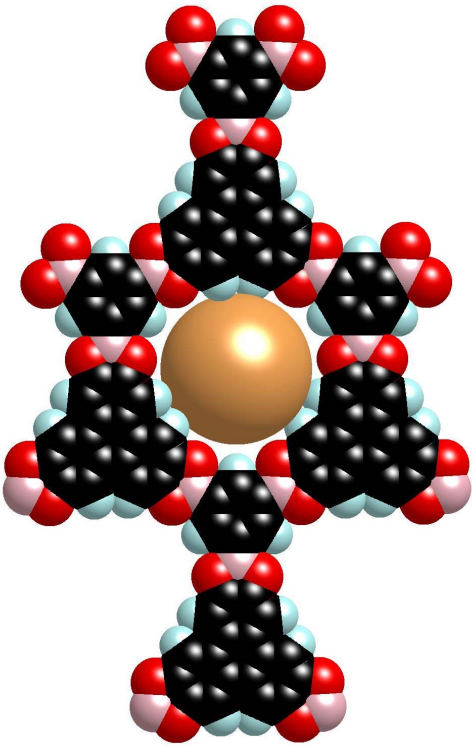

Figure 5.12: COF-6 pore aperture estimation

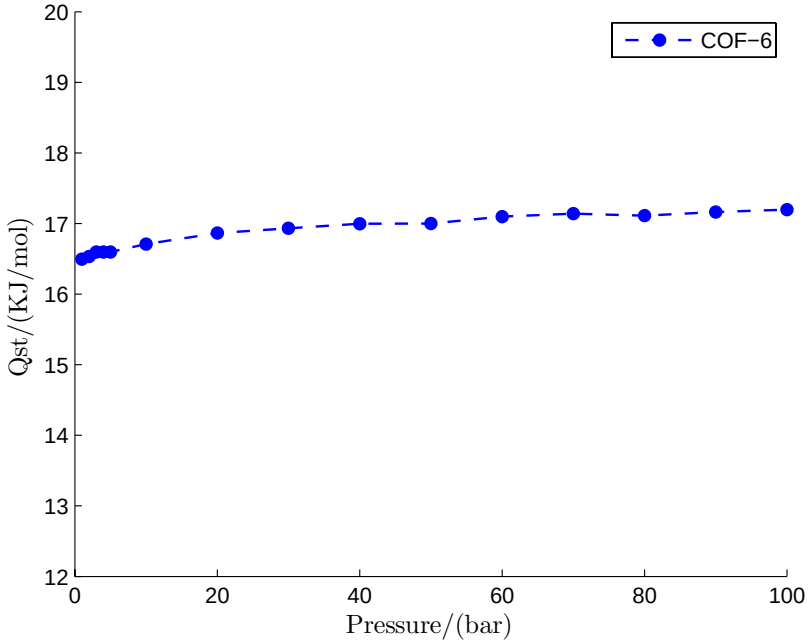

Figure 5.13: Qst values obtained from theory for COF-6

5.4 Studies in COF-8

COF-8 is produced by co-condensation reactions between 2,3,6,7,10,11-hexahydroxy triphenylene and 1,3,5-benzenetris (4-phenylboronic acid). COF-8 is another member of the COF family that has been synthesized. It has the **bnn** topology where graphitic layers are eclipsed and space group $P6/mmm$. All the theory developed before was applied into adsorption studies of methane into COF-8 cylindrical pores. In the following sections data about sorption steps and Qst values (ΔH^{ads})are presented.

5.4.1 Methane adsorption in COF-8

COF-8 has the crystal structure shown in Figure 4.5. A snapshot was taken at the equilibration step of every pressure, these are exposed in Figure 5.14. GCMC simulations were performed with 3,000,000 steps using the Force Field developed in previous sections and explicitly shown in appendix A. Experimental and theoretical data was shown in section 4.2.2 for COF-8.

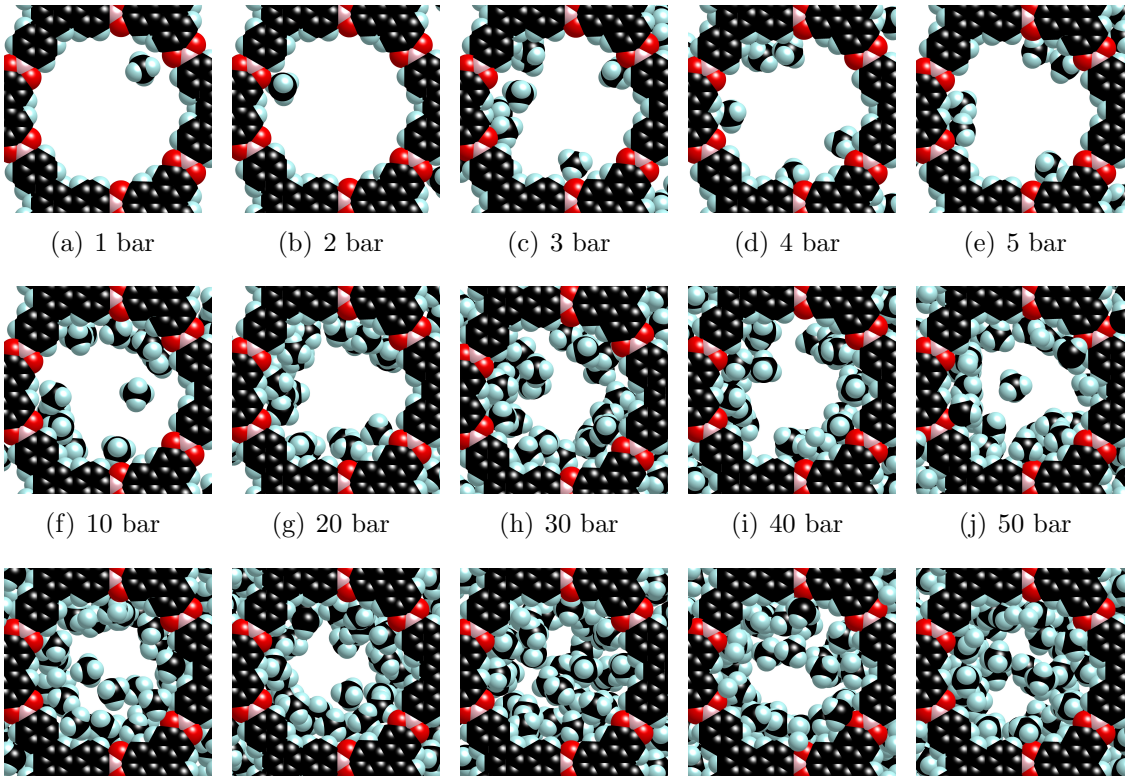

(a) 1 bar (b) 2 bar (c) 3 bar (d) 4 bar (e) 5 bar

(f) 10 bar (g) 20 bar (h) 30 bar (i) 40 bar (j) 50 bar

(k) 60 bar (l) 70 bar (m) 80 bar (n) 90 bar (o) 100 bar

Figure 5.14: COF-8 sorption steps

5.4.2 Qst values for methane in COF-8

For COF-8 this values are ≈ 13 KJ/mol at 298K which are much better that H_2 in MOFs. COF-8 has the third best Qst values for COFs in this study. COF-8 shows the same behavior as COF-1 and COF-6 where there is an increment in Qst values with pressure, for this COF is not so obvious the increment, but there is a 0.3 KJ/mol increment. The estimation of the cylindrical pore aperture was performed, the value of pore aperture is a sphere is placed in the centroid of the pore using van der Waals was of 16.8 Å and it shown in Figure 5.15. For COF-6 estimation of pore aperture was of 9.1 Å and for COF-1 was of 4.0 Å. These values are shorter than COF-5 pore aperture which is of 24.4 Å, accordingly the pore diameter has an effect in this increment of Qst with pressure. A pore diameter smaller than 20 Å is expected to have this interesting characteristic in 2D-COF with cylindrical pores and so potential energy surface to be optimal for methane adsorption. The values obtained are shown in Table 5.6 and they are graphed in Figure 5.16

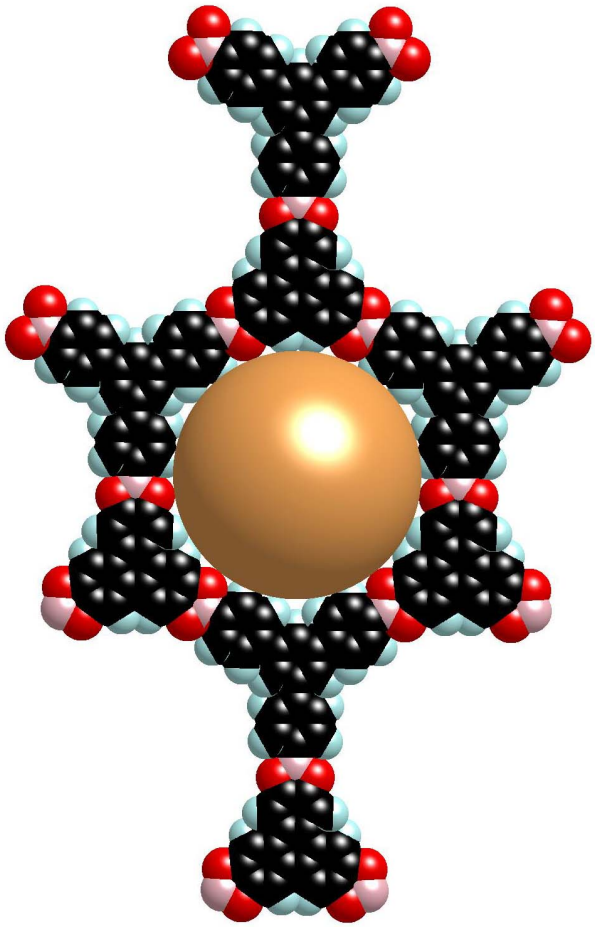

Figure 5.15: COF-8 pore aperture estimation

Table 5.6: Qst values obtained from theory for COF-8

Pressure /(bar)	Qst /(Kcal/mol)	Qst /(KJ/mol)
1	3.05973	12.80191
2	3.06863	12.83915
3	3.08744	12.91785
4	3.09783	12.96132
5	3.09933	12.96760
10	3.12702	13.08345
20	3.17160	13.26997
30	3.19234	13.35675
40	3.19342	13.36127
50	3.20507	13.41001
60	3.19738	13.37784
70	3.18800	13.33859
80	3.19016	13.34763
90	3.18156	13.31165
100	3.16782	13.25416

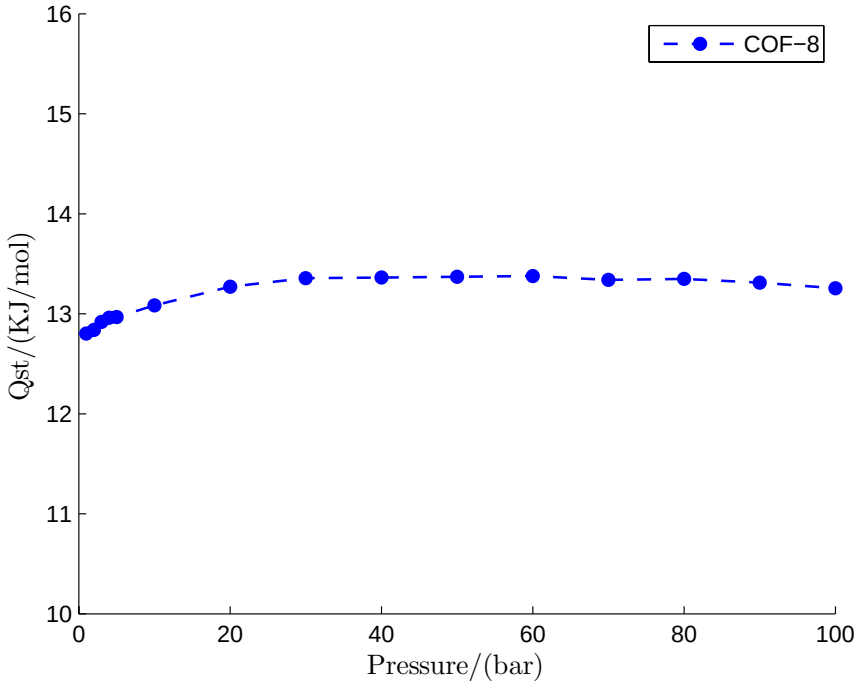

Figure 5.16: Qst values obtained from theory for COF-8

5.5 Studies in COF-10

COF-10 is produced by co-condensation reactions between 2,3,6,7,10,11-hexahydroxy triphenylene and 4,4 -biphenyldiboronic acid [19]. It has the **bnn** topology like COF-5, COF-6 and COF-8 where graphitic layers are eclipsed and space group $P6/mmm$. All the theory developed before was applied into adsorption studies of methane into COF-10 cylindrical pores. The pore diameter of COF-10 is 31.7 Å , which exceeds that of other 2D COFs (COF-1, 9 Å; COF-18A, 18 Å; COF-5, 27 Å) and 3D COFs (COF-102 and -103, 12 Å) [32]. This makes COF-10 a mesoporous material. In the following sections data about sorption steps and Qst values (ΔH^{ads})are presented.

5.5.1 Methane adsorption in COF-10

COF-10 has the crystal structure shown in Figure 5.17. A snapshot was taken at the equilibration step of every pressure, these are exposed in Figure 5.18. GCMC simulations were performed with 3,000,000 steps using the Force Field developed in previous sections and explicitly shown in appendix A. Sorption experimental data at high pressure is not currently available for COF-10, however this methodology can be applied to obtain this data. Once again with this theoretical approach an important quantity is accessible: total amount of gas. As it was mentioned in section 4.2 with experiment this is not easily possible to get or it is meaningless with current gravimetric instruments. Simulation data is presented in Table 5.7 and is graphed in Figure 5.19. At 70 bar saturation has been reached, this can also be observed in Figure 5.18 graphically. The maximum uptake of COF-10 is 12 wt %.

From Figure 5.19 it can observed that in the range from 1-20 bar the sorption uptake is almost linear while from 40-100 bar the increment is of just 1 wt %, also this can be observed at the atomistic level in Figure 5.18. This type of isotherm at high pressure resembles type I isotherm. However it should be remember that these materials it is mesoporous, so at low pressure an isotherm type IV should be observed.

5.5.2 Qst values for methane in COF-10

Qst values for COF-10 range from 12.2 to 11 KJ/mol. COF-10 has almost the same values as COF-5. The of the graph is really interesting, where lineal decaying values are observed, this usually for flat surface. This phenomena should be attributed to the pore aperture of 31.7 Å (See Figure 5.20) where some space is wasted and more of two layers of methane forms in the pore. As it can observed from Figure 5.18 methane molecules does not fill the pore even at 100 bar, this also can be observed from the total uptake plot (See Figure 5.19). The values obtained are shown in Table 5.8 and they are graphed in Figure 5.21

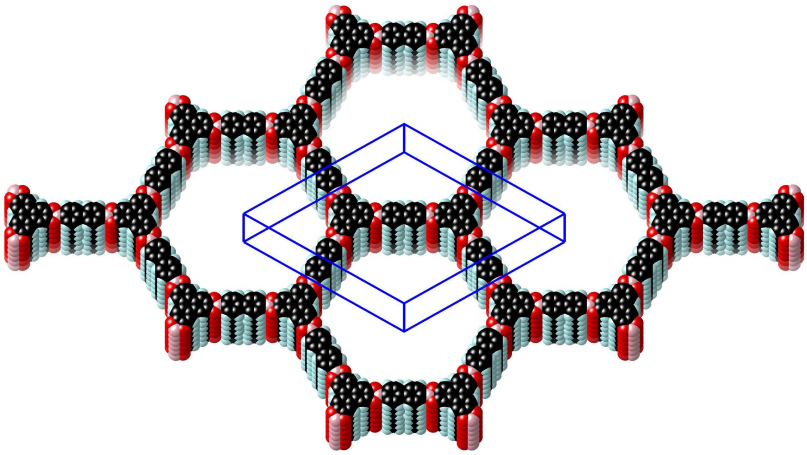

Figure 5.17: COF-10 structure

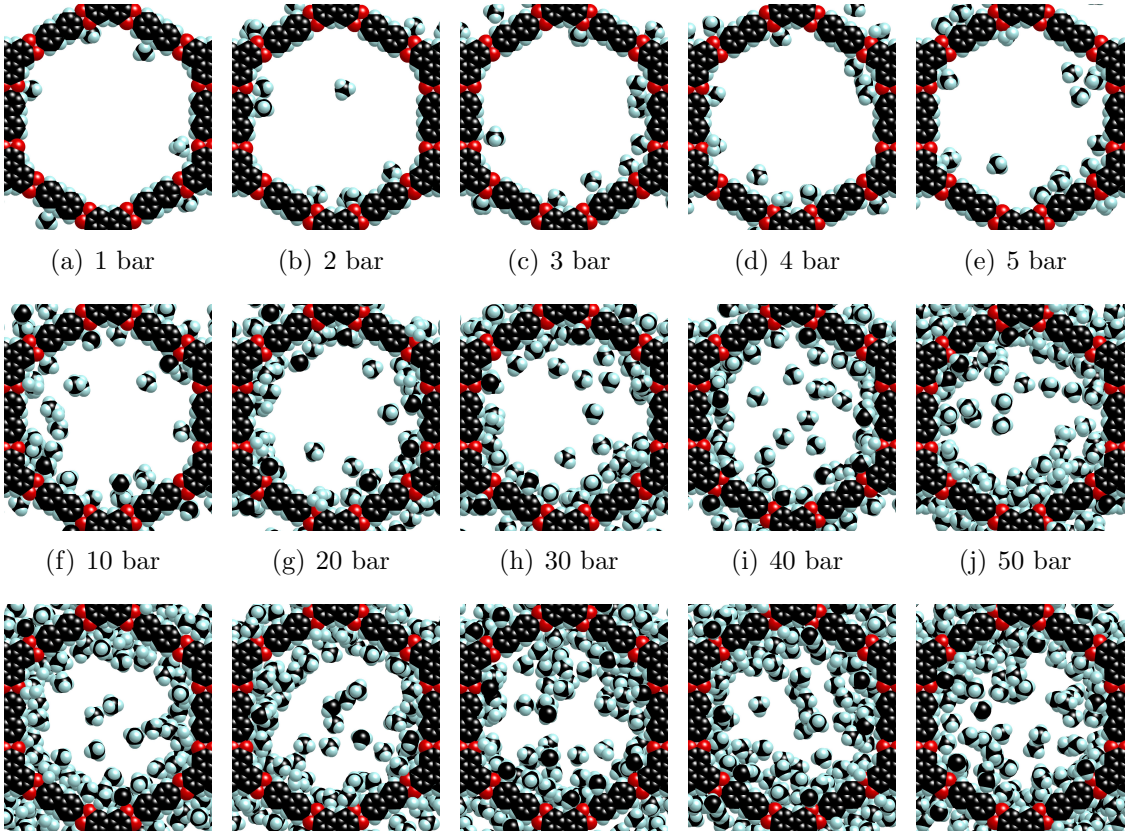

(a) 1 bar (b) 2 bar (c) 3 bar (d) 4 bar (e) 5 bar

(f) 10 bar (g) 20 bar (h) 30 bar (i) 40 bar (j) 50 bar

(k) 60 bar (l) 70 bar (m) 80 bar (n) 90 bar (o) 100 bar

Figure 5.18: COF-10 sorption steps

Table 5.7: Theoretical data obtained for COF-10

Press /(KPa)	Press /(bar)	Total /(wt)%	Excess /(wt)%	Total /(g/L)	Excess /(g/L)
0	0	0.00000	0.00000	0.00000	0.00000
100	1	0.73381	0.64091	3.58618	3.12925
200	2	1.38675	1.20304	6.82199	5.90727
300	3	2.02942	1.75694	10.04906	8.67569
400	4	2.62423	2.26465	13.07374	11.24085
500	5	3.19196	2.74689	15.99541	13.70213
1000	10	5.53785	4.68253	28.44022	23.83187
2000	20	8.97631	7.35886	47.84018	38.53509
3000	30	11.33711	8.99308	62.03121	47.93842
4000	40	13.17730	10.12531	73.62793	54.65381
5000	50	14.59700	10.83737	82.91632	58.96447
6000	60	15.84427	11.38167	91.33521	62.30634
7000	70	16.95076	11.78470	99.01551	64.80734
8000	80	17.93475	12.05962	106.01945	66.52655
9000	90	18.81532	12.22168	112.43126	67.54499
10000	100	19.55102	12.21519	117.89584	67.50415

Table 5.8: Qst values obtained from theory for COF-10

Pressure /(bar)	Qst /(Kcal/mol)	Qst /(KJ/mol)
1	2.92957	12.25732
2	2.93769	12.29129
3	2.94609	12.32644
4	2.93788	12.29209
5	2.93418	12.27661
10	2.92147	12.22343
20	2.88829	12.08461
30	2.85353	11.93917
40	2.81659	11.78461
50	2.77303	11.60236
60	2.73913	11.46052
70	2.70685	11.32546
80	2.68022	11.21404
90	2.65205	11.09618
100	2.62482	10.98225

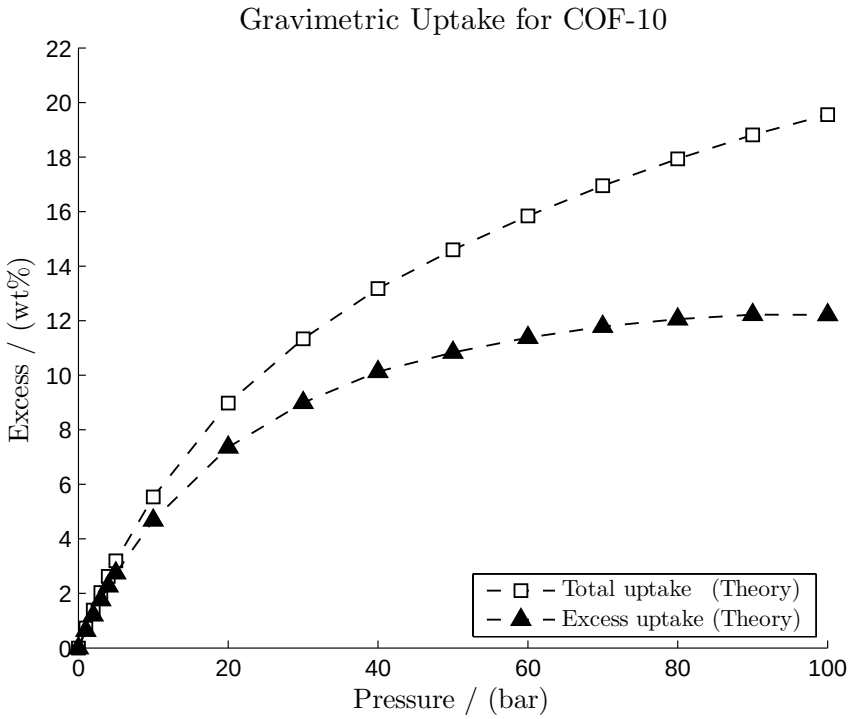

(a) Gravimetric uptake for COF-10

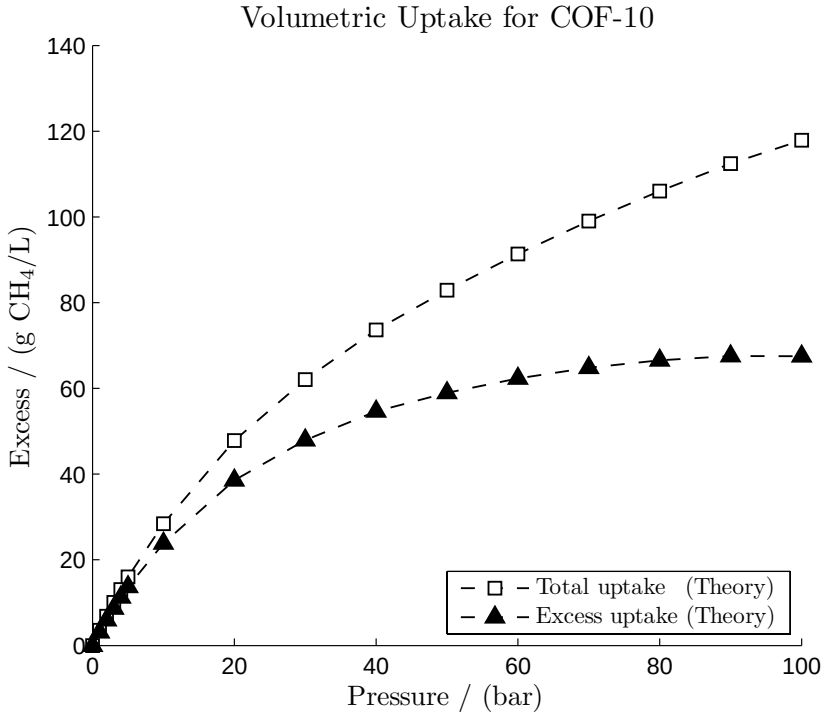

(b) Volumetric uptake for COF-10

Figure 5.19: Theoretical results for COF-10

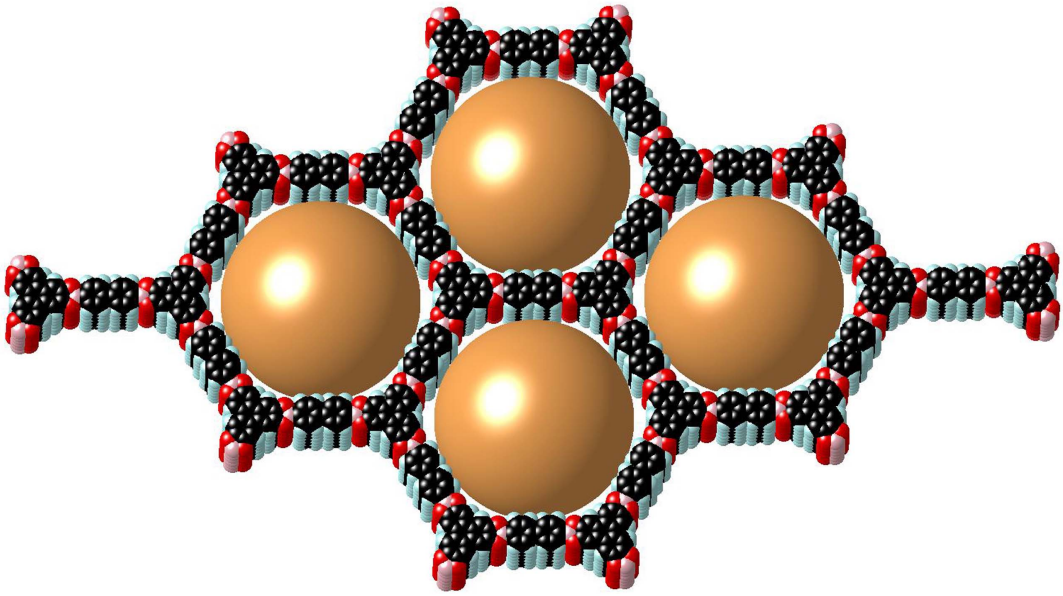

Figure 5.20: COF-10 pore aperture estimation

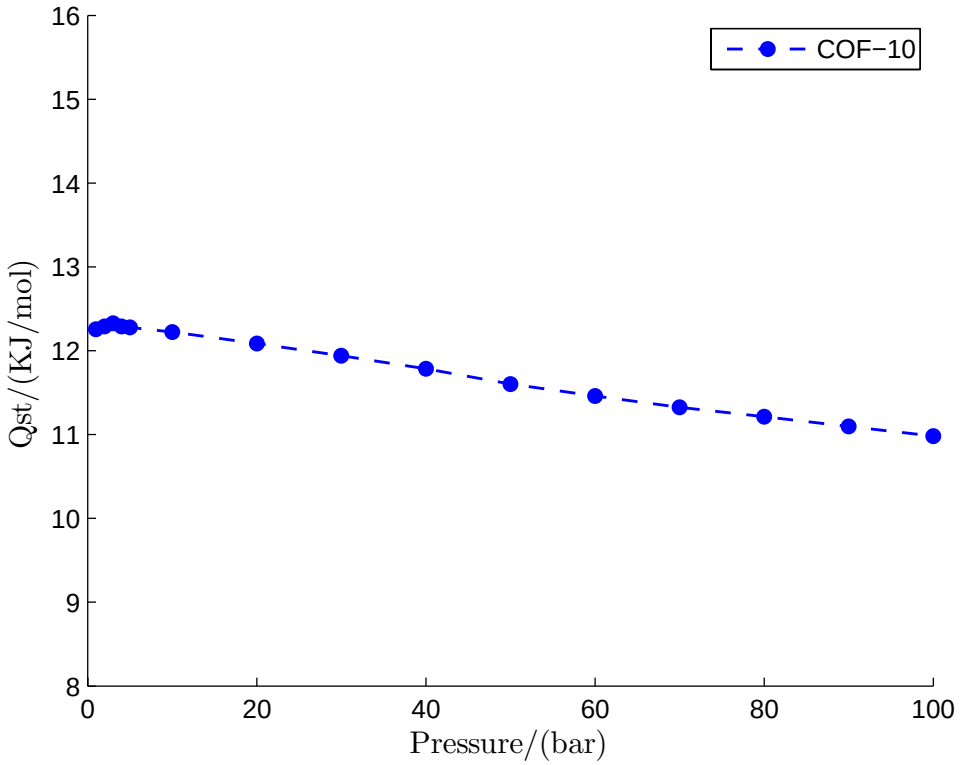

Figure 5.21: Qst values obtained from theory for COF-10

5.6 Studies in COF-102

COF-102 is produced by condensation reactions of tetrahedral tetra(4-dihydroxyborylphenyl) methane [16]. It has the **ctn** topology like COF-103 and COF-105 and space group $I\bar{4}3d$. All the theory developed before was applied into adsorption studies of methane into COF-102 pores. The pore diameter of COF-102 is 12 Å . This makes COF-102 a beautiful example of microporous crystalline material. In the following sections data about sorption steps and Qst values (ΔH^{ads})are presented.

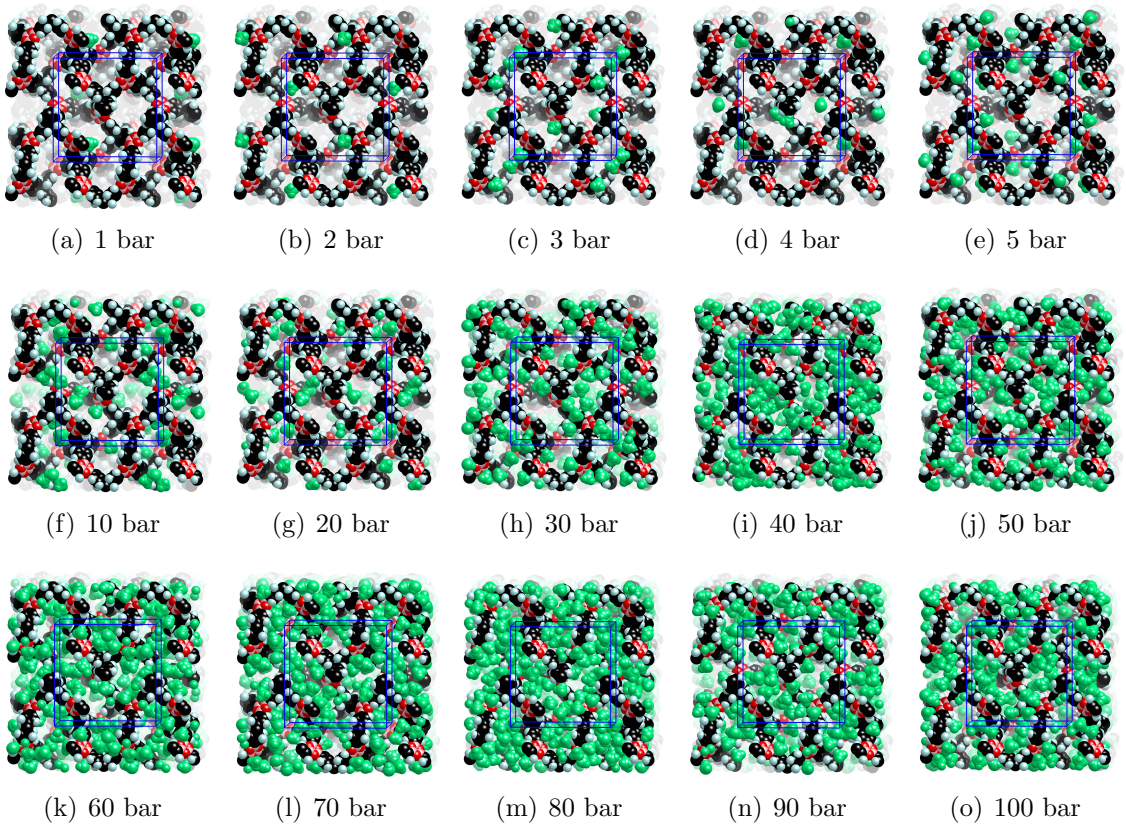

(a) 1 bar (b) 2 bar (c) 3 bar (d) 4 bar (e) 5 bar

(f) 10 bar (g) 20 bar (h) 30 bar (i) 40 bar (j) 50 bar

(k) 60 bar (l) 70 bar (m) 80 bar (n) 90 bar (o) 100 bar

Figure 5.22: COF-102 sorption steps

5.6.1 Methane adsorption in COF-102

COF-102 has the crystal structure shown in Figure 1.11. A snapshot was taken at the equilibration step of every pressure, these are exposed in Figure 5.22. GCMC simulations were performed with 3,000,000 steps using the Force Field developed in previous sections and explicitly shown in appendix A. Sorption experimental data at high pressure is not currently available for COF-102, however this methodology can be applied to obtain this data.

Simulation data is presented in Table 5.9 and is graphed in Figure 5.23. At 100 bar saturation has not been reached yet, this can also be observed in Figure 5.22 graphically. The maximum uptake of COF-102 is 23.8 wt % at 100 bar, the fourth best uptake for studied COFs, after COF-105 and COF-103 in gravimetric units. In volumetric units is the third best after COF-103 and COF-1.

From Figure 5.23 it can observed that in the range from 1-40 bar the sorption uptake is almost linear while from 40-100 bar the increment is of 5 wt %, also this can be observed at the atomistic level in Figure 5.22. This type of isotherm at high pressure resembles type I isotherm. Even at low pressure an isotherm type I should be observed.

Table 5.9: Theoretical data obtained for COF-102

Press /(KPa)	Press /(bar)	Total /(wt)%	Excess /(wt)%	Total /(g/L)	Excess /(g/L)
0	0	0.00000	0.00000	0.00000	0.00000
100	1	0.83910	0.76198	3.55878	3.22922
200	2	1.57327	1.42108	6.72232	6.06269
300	3	2.32517	2.10002	10.01159	9.02136
400	4	3.08262	2.78660	13.37668	12.05534
500	5	3.80615	3.44108	16.64058	14.98761
1000	10	7.13732	6.45175	32.32395	29.00496
2000	20	12.61194	11.37989	60.69603	54.00525
3000	30	16.63889	14.93308	83.94432	73.82767
4000	40	19.74188	17.60373	103.44987	89.85197
5000	50	21.97353	19.41145	118.43722	101.30133
6000	60	23.89406	20.92749	132.03891	111.30690
7000	70	25.38621	22.01187	143.08995	118.70224
8000	80	26.59477	22.80823	152.37009	124.26559
9000	90	27.64624	23.44706	160.69608	128.81220
10000	100	28.42917	23.79591	167.05461	131.32711

5.6.2 Qst values for methane in COF-102

Qst values for COF-102 range from 9.5 to 11 KJ/mol. COF-102 values are slightly less than COF-103 but better than COF-105, COF-108 and COF-300. The shape of the plot is the same as for COF-1, COF-6 and COF-8, where there is an increment in the sorption energy as the pressure increase, as it was mentioned before the pore diameter of COF-102 is 12 Å so the hypothesis that a pore diameter less than 20 Å is fulfill for this case. Thus COF-102 has a diameter that creates synergy between

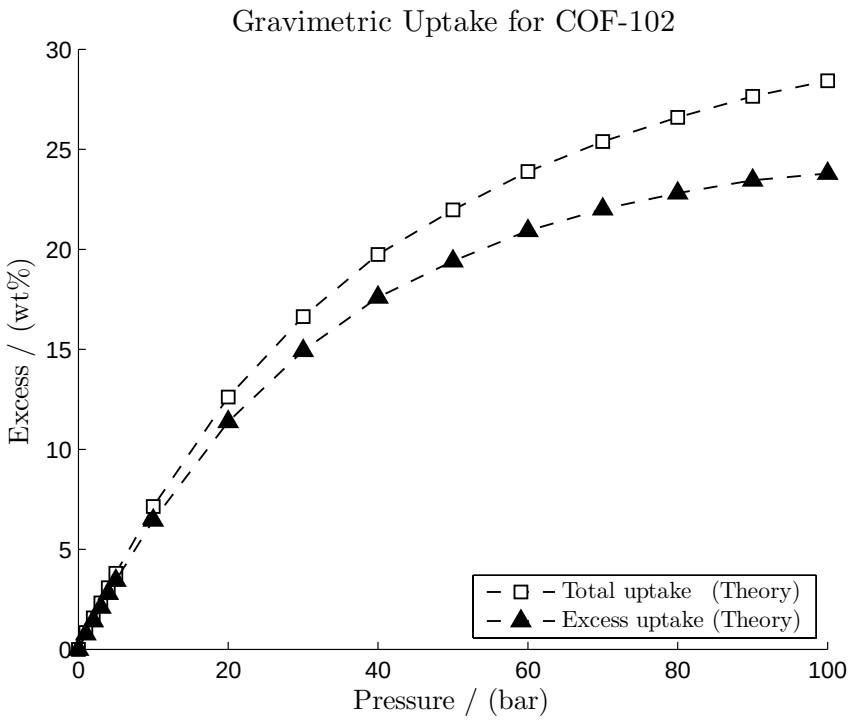

(a) Gravimetric uptake for COF-102

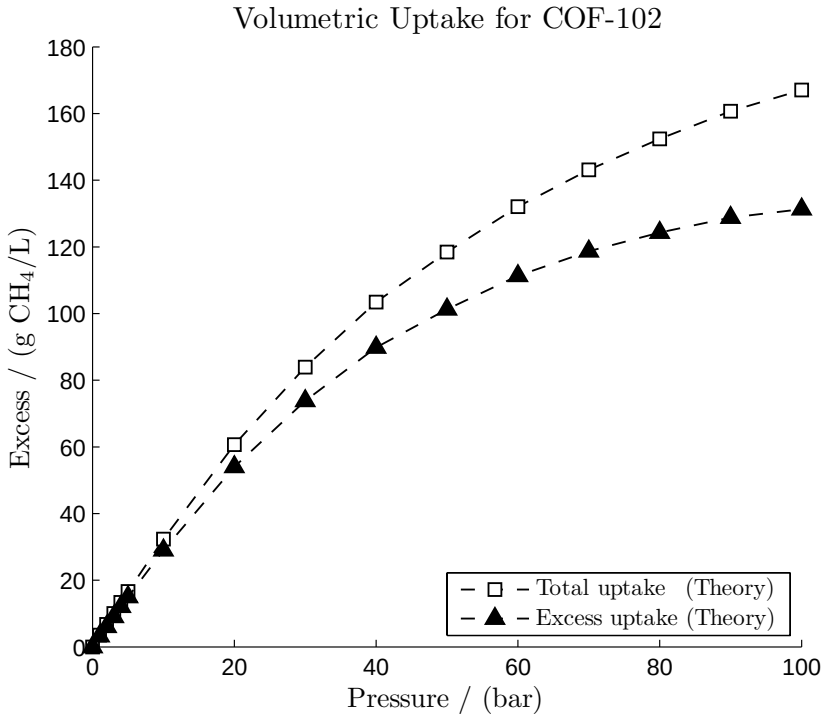

(b) Volumetric uptake for COF-102

Figure 5.23: Theoretical results for COF-102

absorbed gas and accessible surface of the framework; there is not an explicit wasting space. The values obtained are shown in Table 5.10 and they are graphed in Figure 5.24.

Table 5.10: Qst values obtained from theory for COF-102

Pressure /(bar)	Qst /(Kcal/mol)	Qst /(KJ/mol)
1	2.30793	9.65638
2	2.31237	9.67496
3	2.32069	9.70977
4	2.32844	9.74219
5	2.33473	9.76851
10	2.36455	9.89328
20	2.42036	10.12679
30	2.46281	10.30440
40	2.50278	10.47163
50	2.52981	10.58473
60	2.55742	10.70025
70	2.58012	10.79522
80	2.60074	10.88150
90	2.61891	10.95752
100	2.63313	11.01702

5.7 Studies in COF-103

COF-103 is produced by condensation reactions of tetrahedral tetra(4-dihydroxyborylphenyl)silane [16]. It has the **ctn** topology like COF-102 and COF-105 and space group $I\bar{4}3d$. All the theory developed before was applied into adsorption studies of methane into COF-103 pores. The pore diameter of COF-103 is 12 Å , almost the same as COF-102. This makes COF-103 another beautiful example of microporous crystalline material. In the following sections data about sorption steps and Qst values (ΔH^{ads})are presented.

5.7.1 Methane adsorption in COF-103

COF-103 has the crystal structure shown in Figure 1.11. A snapshot was taken at the equilibration step of every pressure, the look like COF-102 steps so there is not need to show them again. GCMC simulations were performed with 3,000,000 steps using the Force Field developed in previous sections and explicitly shown in appendix A.

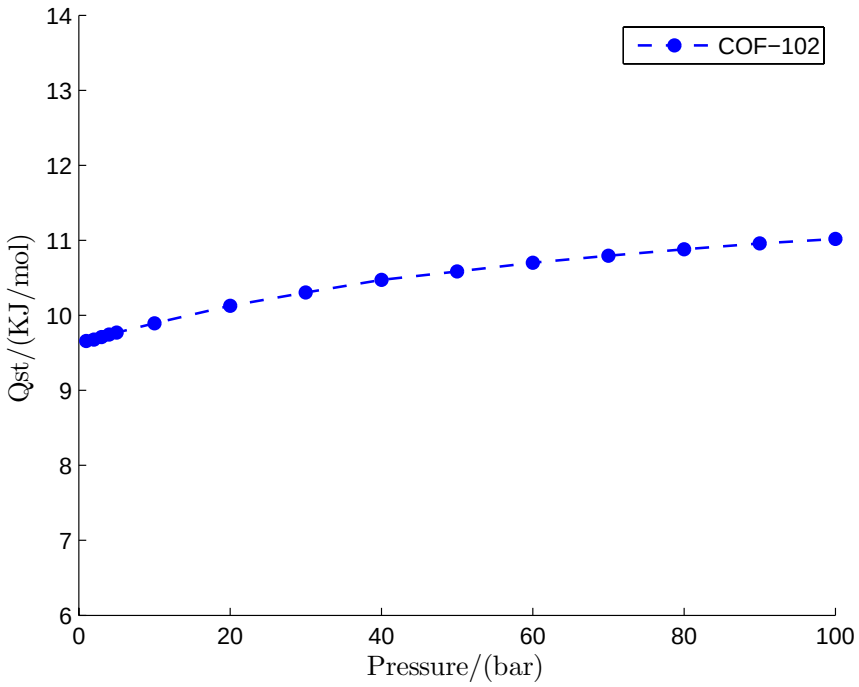

Figure 5.24: Qst values obtained from theory for COF-102

Sorption experimental data at high pressure is not currently available for COF-103, however this methodology can be applied to obtain this data.

Simulation data is presented in Table 5.11 and is graphed in Figure 5.25. At 100 bar saturation has not been reached yet and the maximum uptake of COF-103 is 26.6 wt % at 100 bar, the second best uptake for studied COFs, after COF-105 in gravimetric units. *In volumetric units is the best with an uptake of 138.0 g/L.*

5.7.2 Qst values for methane in COF-103

Qst values for COF-103 range from 9.85 to 11.05 KJ/mol. COF-103 values are slightly bigger than COF-102 but better than COF-105, COF-108 and COF-300. Even COF-103 has the best values for 3D-COFs of this study they can not compete with values of 2D-COFs (12-25 KJ/mol). The plot has the same shape as COF-1, COF-6, COF-8 and COF-102, where there is an increment in the sorption energy as the pressure increase, as it was mentioned before the pore diameter of COF-102 is 12 Å so the hypothesis that a pore diameter less than 20 Å is fulfill for this case. Thus COF-103 has a diameter that creates synergy between absorbed gas and accessible surface of the framework; there is not an explicit wasting space. The values obtained are shown in Table 5.12 and they are graphed in Figure 5.26.

Table 5.11: Theoretical data obtained for COF-103

Press /(KPa)	Press /(bar)	Total /(wt)%	Excess /(wt)%	Total /(g/L)	Excess /(g/L)
0	0	0.00000	0.00000	0.00000	0.00000
100	1	0.95351	0.87530	3.66156	3.35856
200	2	1.83417	1.68027	7.10655	6.50007
300	3	2.71605	2.48898	10.61882	9.70837
400	4	3.57457	3.27666	14.09975	12.88486
500	5	4.38091	4.01416	17.42606	15.90623
1000	10	8.19097	7.50962	33.93353	30.88168
2000	20	14.17565	12.96726	62.82201	56.66894
3000	30	18.64731	16.99533	87.18136	77.87648
4000	40	21.86705	19.80642	106.44747	93.93897
5000	50	24.27516	21.82131	121.92793	106.16268
6000	60	26.21939	23.38423	135.16361	116.08718
7000	70	27.87602	24.67007	147.00447	124.56102
8000	80	29.08006	25.48601	155.95756	130.08984
9000	90	30.10005	26.11463	163.78335	134.43264
10000	100	31.00273	26.62427	170.90207	138.00814

5.8 Studies in COF-105

COF-105 is produced by by co-condensation of triangular 2,3,6,7,10,11-hexahydroxytriphenylene and tetrahedral tetra(4-dihydroxyborylphenyl)silane. It has the **ctn** topology like COF-102 and COF-103 and space group $I\bar{4}3d$. All the theory developed before was applied into adsorption studies of methane into COF-105 pores. The pore diameter of COF-105 is about 20.5 Å . In the following sections data about sorption steps and Qst values (ΔH^{ads})are presented.

5.8.1 Methane adsorption in COF-105

COF-105 has the crystal structure shown in Figure 1.12. A snapshot was taken at the equilibration step of every pressure, the look like COF-102 and COF-103 steps so there is not need to show them again. GCMC simulations were performed with 3,000,000 steps using the Force Field developed in previous sections and explicitly shown in appendix A. Sorption experimental data at high pressure is not currently available for COF-105, however this methodology can be applied to obtain this data.

Simulation data is presented in Table 5.13 and is graphed in Figure 5.27. At 100

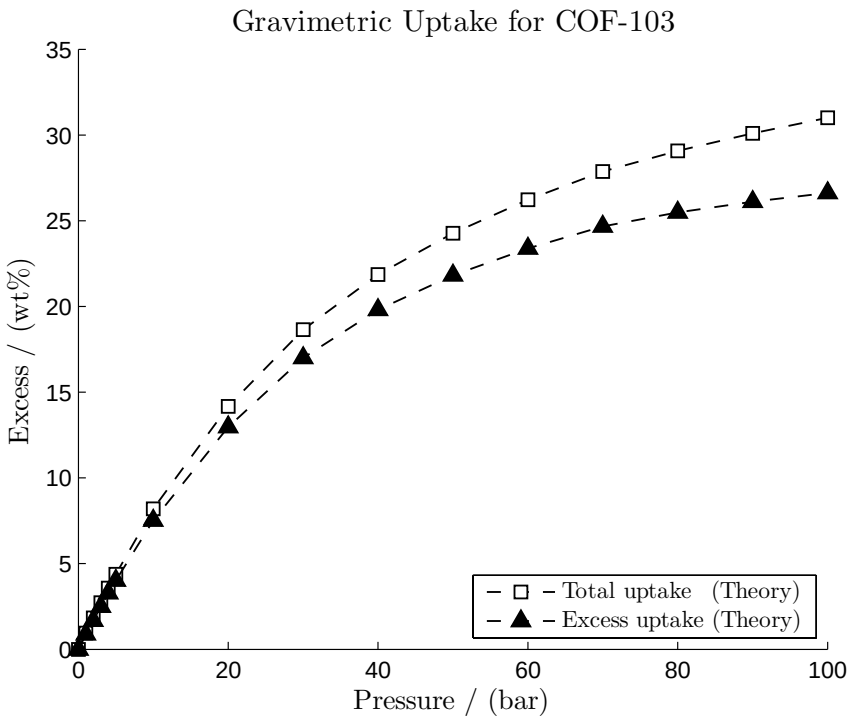

(a) Gravimetric uptake for COF-103

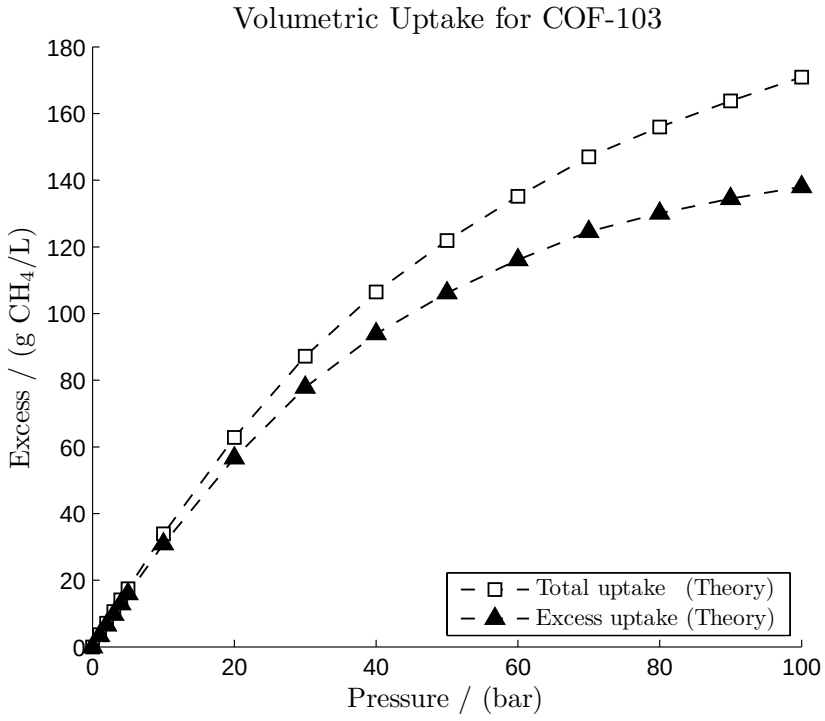

(b) Volumetric uptake for COF-103

Figure 5.25: Theoretical results for COF-103

Table 5.12: Qst values obtained from theory for COF-103

Pressure /(bar)	Qst /(Kcal/mol)	Qst /(KJ/mol)
1	2.35360	9.84746
2	2.36387	9.89043
3	2.36872	9.91072
4	2.37386	9.93223
5	2.37923	9.95470
10	2.40595	10.06649
20	2.45125	10.25603
30	2.49367	10.43352
40	2.52698	10.57288
50	2.55021	10.67008
60	2.57289	10.76497
70	2.59792	10.86970
80	2.61459	10.93944
90	2.62638	10.98877
100	2.64087	11.04940

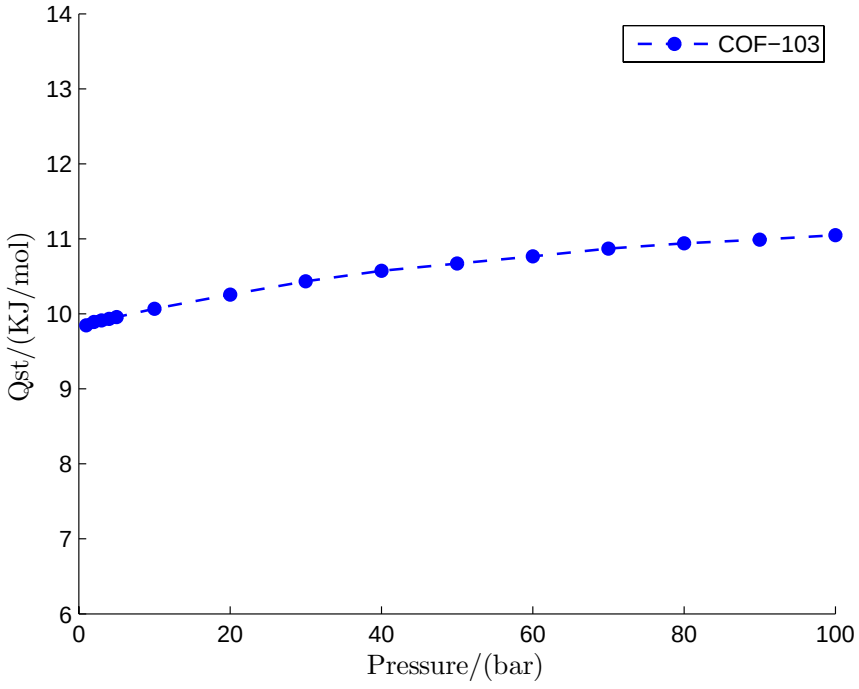

Figure 5.26: Qst values obtained from theory for COF-103

bar saturation has not been reached yet and the maximum uptake of COF-103 is 27.60

wt % at 100 bar, *the best uptake for studied COFs* in gravimetric units. In volumetric units is the sixth best after COF-103, COF-1, COF-102, COF-8 and COF-5 with an uptake of 69.5 g/L.

Table 5.13: Theoretical data obtained for COF-105

Press /(KPa)	Press /(bar)	Total /(wt)%	Excess /(wt)%	Total /(g/L)	Excess /(g/L)
0	0	0.00000	0.00000	0.00000	0.00000
100	1	1.11867	0.89206	2.06313	1.64145
200	2	2.19663	1.75121	4.09584	3.25051
300	3	3.22982	2.57276	6.08663	4.81569
400	4	4.22385	3.36178	8.04248	6.34395
500	5	5.23244	4.17268	10.06894	7.94082
1000	10	9.65154	7.68188	19.48119	15.17469
2000	20	16.59199	13.08533	36.27690	27.45561
3000	30	21.98511	17.18086	51.39142	37.83151
4000	40	26.15134	20.15709	64.57892	46.03954
5000	50	29.68466	22.58710	76.98774	53.20917
6000	60	32.50408	24.29477	87.82128	58.52296
7000	70	34.88318	25.54594	97.69278	62.57097
8000	80	37.06559	26.61219	107.40444	66.12963
9000	90	38.93635	27.30439	116.28188	68.49578
10000	100	40.51612	27.60153	124.21326	69.52535

5.8.2 Qst values for methane in COF-105

Qst values for COF-105 range from 8.42 to 8.19 KJ/mol. COF-105 values are second last Qst values for studied COFs, it is just better than COF-108. The plot has the same shape as COF-5 and COF-10, where there is an decrement in the sorption energy as the pressure increase, as it was mentioned before the pore diameter of COF-105 is 20.5 Å so the hypothesis that a pore diameter bigger than 20 Å generate this behaviour is fulfill again. The values obtained are shown in Table 5.14 and they are graphed in Figure 5.28.

5.9 Studies in COF-108

COF-108 is produced by co-condensation of triangular 2,3,6,7,10,11-hexahydroxytriphenylene and tetrahedral tetra(4-dihydroxyborylphenyl) methane.

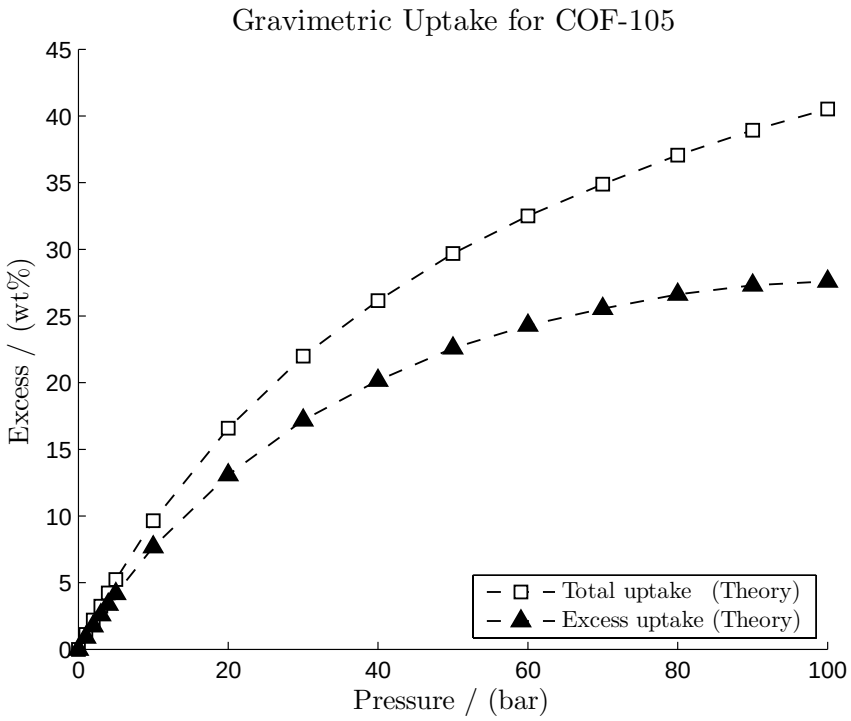

(a) Gravimetric uptake for COF-105

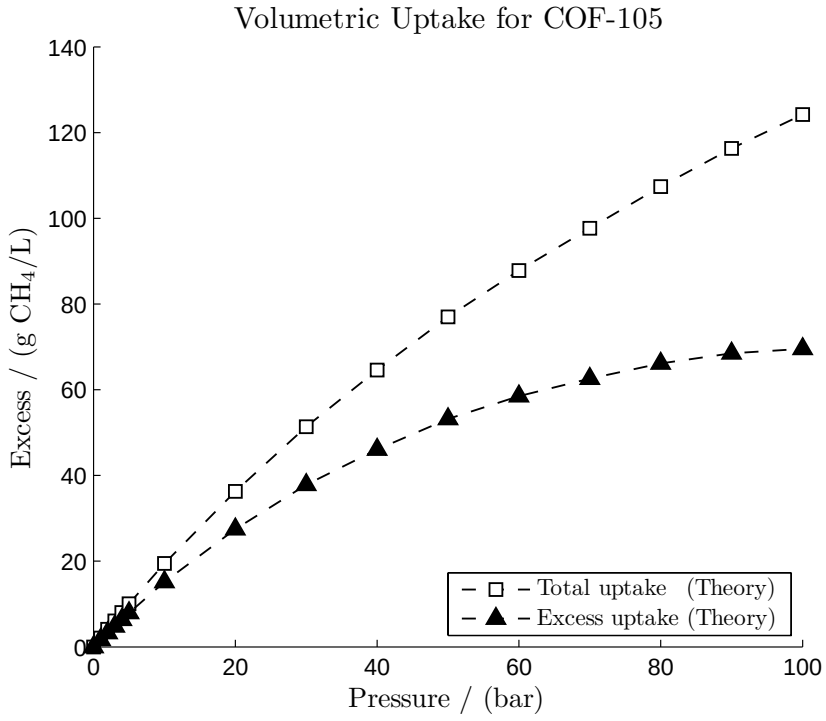

(b) Volumetric uptake for COF-105

Figure 5.27: Theoretical results for COF-105

Table 5.14: Qst values obtained from theory for COF-105

Pressure /(bar)	Qst /(Kcal/mol)	Qst /(KJ/mol)
1	2.01262	8.42080
2	2.01689	8.43867
3	2.01057	8.41222
4	2.00714	8.39787
5	1.99844	8.36147
10	2.00445	8.38662
20	1.99239	8.33616
30	1.99038	8.32775
40	1.98347	8.29884
50	1.97416	8.25989
60	1.96964	8.24097
70	1.96899	8.23825
80	1.96831	8.23541
90	1.96208	8.20934
100	1.95904	8.19662

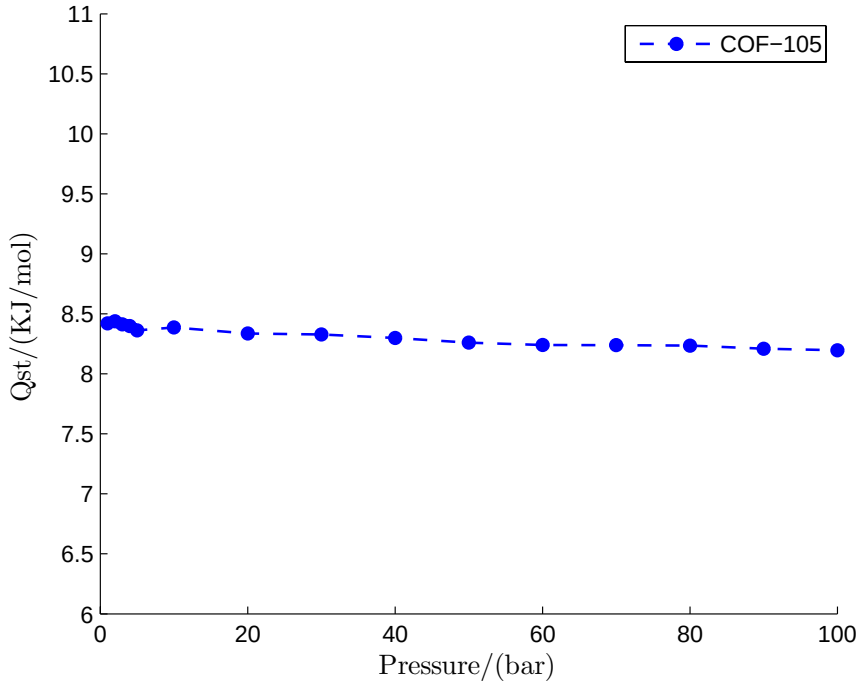

Figure 5.28: Qst values obtained from theory for COF-105

It is the only 3D-COF with the **bor** topology and space group $P\bar{4}3m$. All the theory

developed before was applied into adsorption studies of methane into COF-108 pores. COF-108 has two cavities, 11.34 and 19.56 Å, it should be noted that this are ideal spheres adn the pore is expected to larger (See Figure 5.29). Then COF-108 is a rare example of a fully crystalline mesoporous material. In the following sections data about sorption steps and Qst values (ΔH^{ads})are presented.

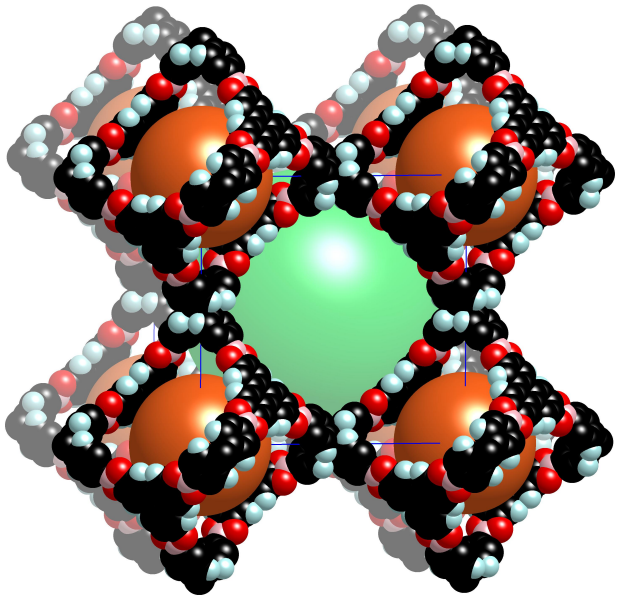

Figure 5.29: COF-108 pore aperture estimation. The green sphere represents the bigger pore (19.56 Å) and brown sphere the smaller pore (11.34 Å)

5.9.1 Methane adsorption in COF-108

COF-102 has the crystal structure shown in Figure 1.13. A snapshot was taken at the equilibration step of every pressure, these are exposed in Figure 5.30. GCMC simulations were performed with 3,000,000 steps using the Force Field developed in previous sections and explicitly shown in appendix A. Sorption experimental data at high pressure is not currently available for COF-108, however this methodology can be applied to obtain this data.

Simulation data is presented in Table 5.15 and is graphed in Figure 5.32. At 100 bar saturation has not been reached yet, this can also be observed in Figure 5.22 and Figure 5.31 graphically. The maximum uptake of COF-108 is 20.90 wt % at 100 bar, the third best uptake for studied COFs, after COF-105 and COF-103 in gravimetric units. However in volumetric units is the worst uptake. This is due the lowest density among COFs.

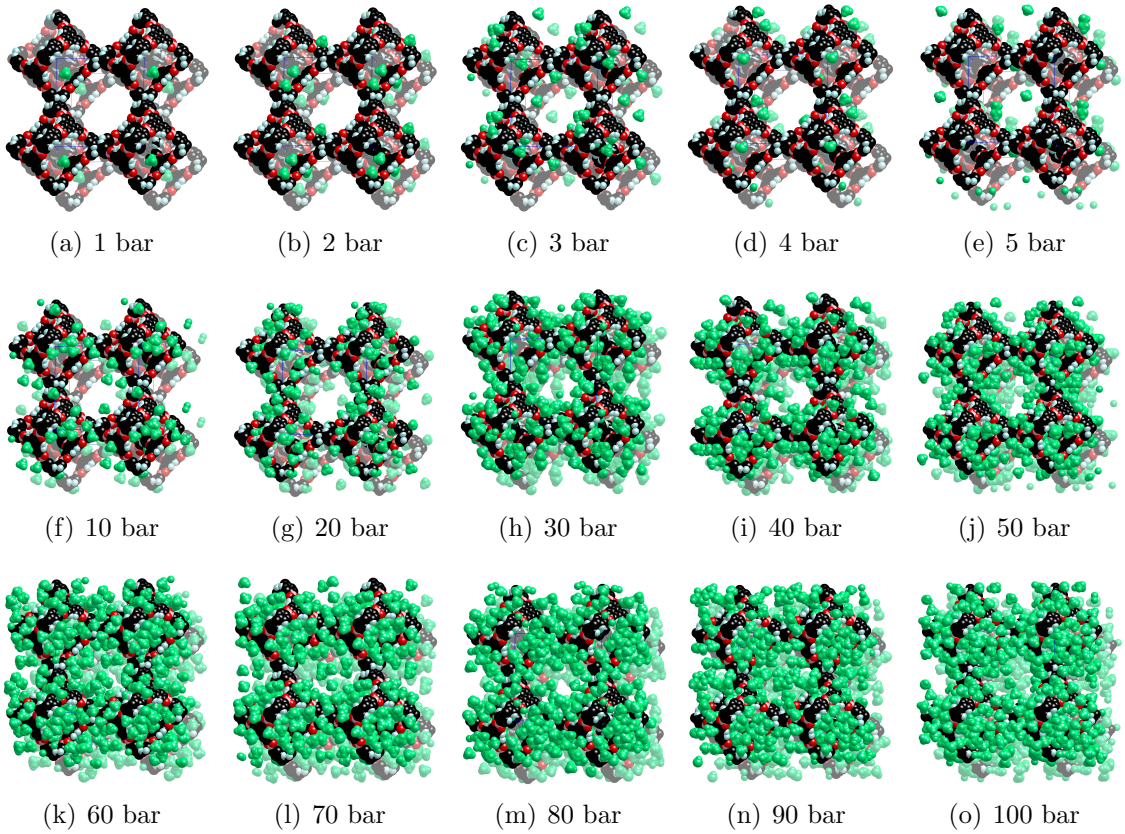

(a) 1 bar (b) 2 bar (c) 3 bar (d) 4 bar (e) 5 bar

(f) 10 bar (g) 20 bar (h) 30 bar (i) 40 bar (j) 50 bar

(k) 60 bar (l) 70 bar (m) 80 bar (n) 90 bar (o) 100 bar

Figure 5.30: COF-108 sorption steps

5.9.2 Qst values for methane in COF-108

Qst values for COF-108 range from 8.45 to 7.86 KJ/mol. COF-108 have the worst Qst values for studied COFs. The plot has the same shape as COF-5, COF-10, and COF-105 where there is an decrement in the sorption energy as the pressure increase, as it was mentioned before COF-108 has two cavities, 11.34 and 19.56 Å, so the hypothesis that a pore diameter bigger than 20 Å generate this behaviour is fulfill again. The values obtained are shown in Table 5.16 and they are graphed in Figure 5.33.

5.10 Studies in COF-300

COF-300 is an hypothetical structure formed from triangular and tetrahedral building blocks (see Figure 5.34). It is the **bor** topology and space group $P\overline{4}3m$. COF-300 has the crystal structure shown in Figure 5.35. Cerius^2 software was used to apply these concepts [33]. All the theory developed before was applied into adsorption studies of methane into COF-103 pores. The pore diameter of COF-103 is 12 Å , almost the

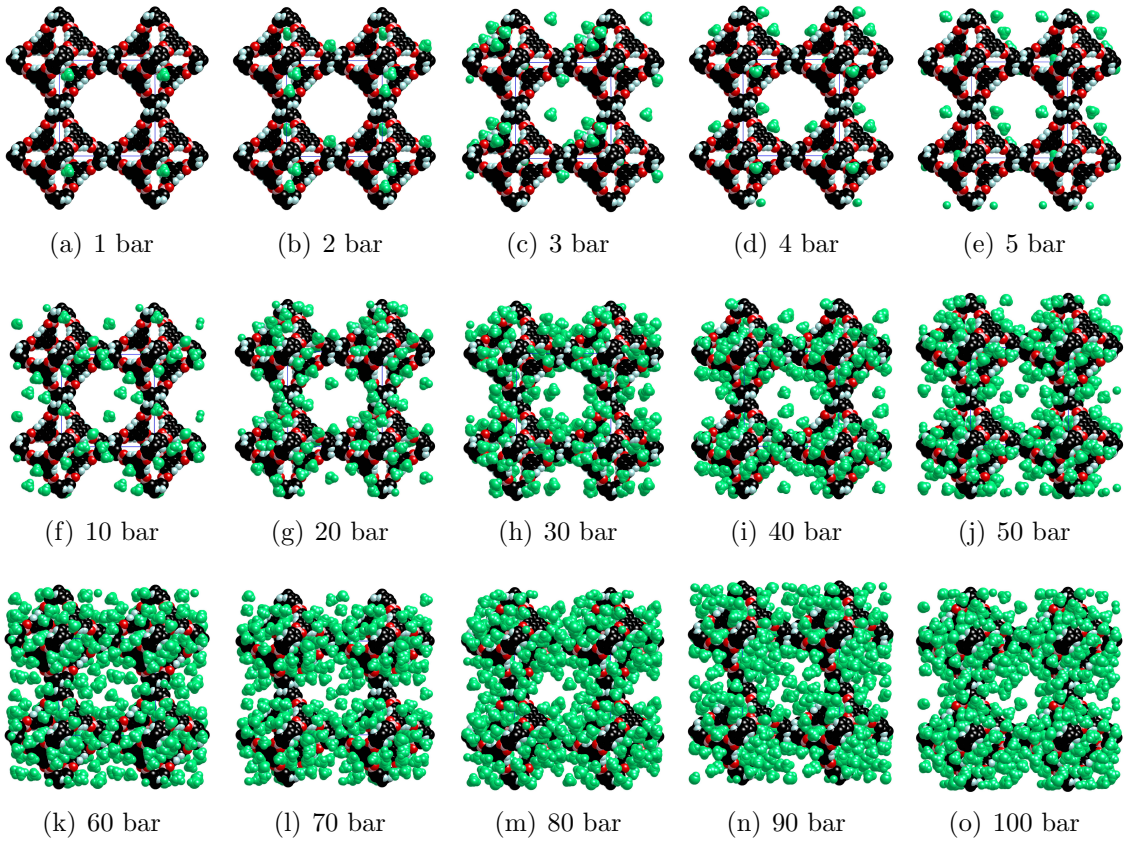

(a) 1 bar (b) 2 bar (c) 3 bar (d) 4 bar (e) 5 bar

(f) 10 bar (g) 20 bar (h) 30 bar (i) 40 bar (j) 50 bar

(k) 60 bar (l) 70 bar (m) 80 bar (n) 90 bar (o) 100 bar

Figure 5.31: COF-108 sorption in hkl plane = 001

same as COF-102. This makes COF-103 another beautiful example of microporous crystalline material. In the following sections data about sorption steps and Qst values (ΔH^{ads})are presented.

5.10.1 Methane adsorption in COF-300

A snapshot was taken at the equilibration step of every pressure, the look like COF-108 steps so there is not need to show them again. GCMC simulations were performed with 3,000,000 steps using the Force Field developed in previous sections and explicitly shown in appendix A. Sorption experimental data at high pressure is not currently available for COF-103, however this methodology can be applied to obtain this data. Simulation data is presented in Table 5.17 and is graphed in Figure 5.36. The maximum uptake of COF-300 is 18.8 wt % at 100 bar, the fifth best uptake for studied COFs. In volumetric units is the second worst with an uptake of 63.1 g/L.

Table 5.15: Theoretical data obtained for COF-108

Press /(KPa)	Press /(bar)	Total /(wt)%	Excess /(wt)%	Total /(g/L)	Excess /(g/L)
0	0	0.00000	0.00000	0.00000	0.00000
100	1	1.29978	1.02519	2.22197	1.74770
200	2	2.29384	1.75266	3.96122	3.00999
300	3	3.30336	2.50388	5.76412	4.33325
400	4	4.30039	3.25051	7.58203	5.66880
500	5	5.27912	3.98641	9.40380	7.00546
1000	10	9.67983	7.26436	18.08299	13.21715
2000	20	16.55049	12.19906	33.46374	23.44309
3000	30	21.96391	15.94153	47.48995	31.99897
4000	40	26.23679	18.66024	60.01481	38.70811
5000	50	29.86541	20.81318	71.84948	44.34789
6000	60	32.60757	21.97637	81.63845	47.52446
7000	70	35.20575	23.03198	91.67790	50.49035
8000	80	37.44819	23.64176	101.01328	52.24098
9000	90	39.52477	24.02304	110.27559	53.34990
10000	100	41.45607	24.16493	119.47960	53.76542

5.10.2 Qst values for methane in COF-300

Qst values for COF-300 range from 8.15 to 8.62 KJ/mol. COF-300 values are slightly bigger than COF-105 and COF-108. The shape of the plot is the same as for COF-1, COF-6, COF-8, COF-102 and COF-103 where there is an increment in the sorption energy as the pressure increase. The values obtained are shown in Table 5.18 and they are graphed in Figure 5.37.

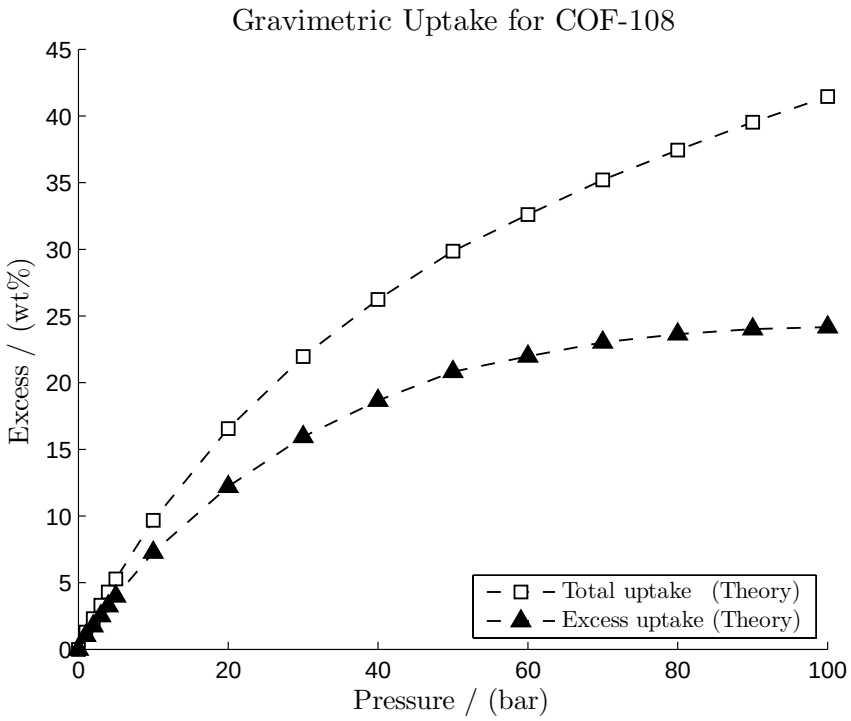

(a) Gravimetric uptake for COF-108

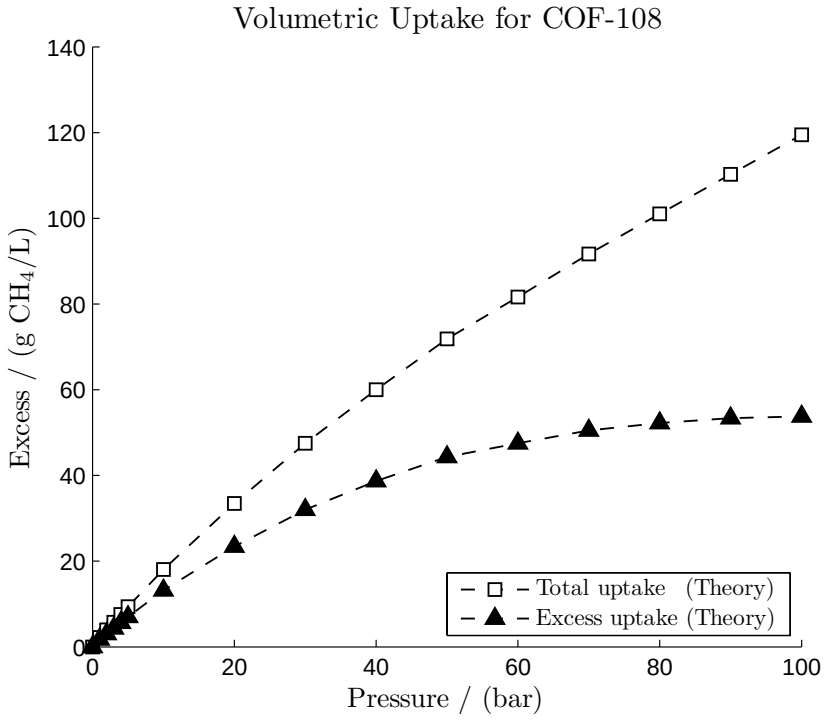

(b) Volumetric uptake for COF-108

Figure 5.32: Theoretical results for COF-108

Table 5.16: Qst values obtained from theory for COF-108

Pressure /(bar)	Qst /(Kcal/mol)	Qst /(KJ/mol)
1	2.02002	8.45176
2	2.02878	8.48842
3	2.01507	8.43105
4	2.01431	8.42787
5	2.00991	8.40946
10	1.9912	8.33118
20	1.95707	8.18838
30	1.94572	8.14089
40	1.92484	8.05353
50	1.91617	8.01726
60	1.90192	7.95763
70	1.89861	7.94378
80	1.89534	7.93010
90	1.88506	7.88709
100	1.87979	7.86504

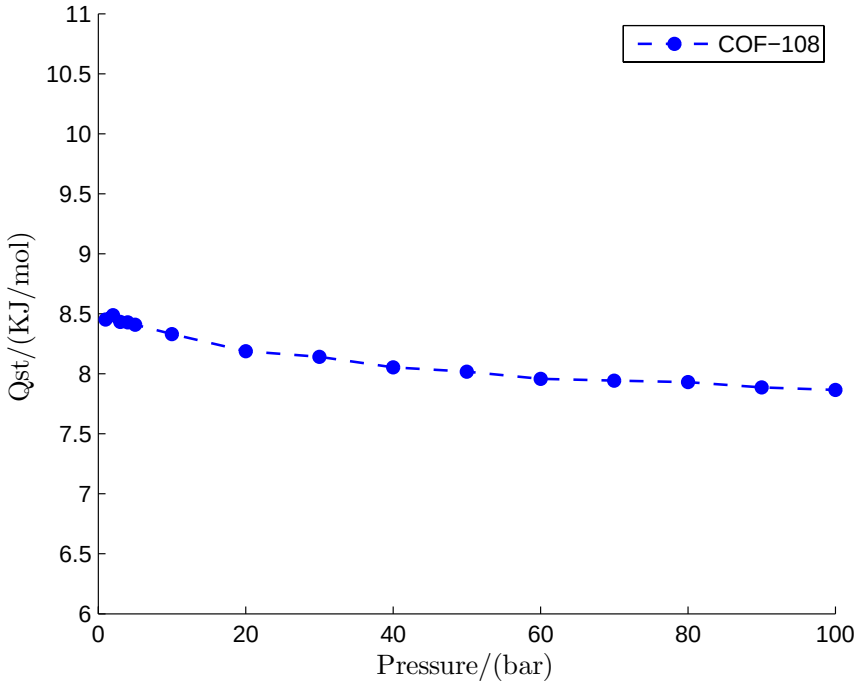

Figure 5.33: Qst values obtained from theory for COF-108

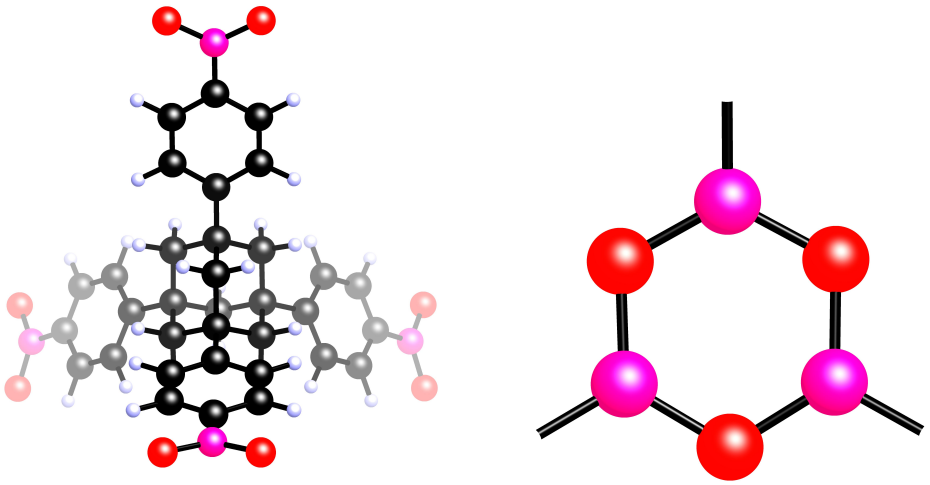

(a) Tetrahedral SBU for COF-300 (b) Triangular SBU for COF-300

Figure 5.34: Building blocks for COF-300

Table 5.17: Theoretical data obtained for COF-300

Press /(KPa)	Press /(bar)	Total /(wt)%	Excess /(wt)%	Total /(g/L)	Excess /(g/L)
0	0	0	0	0	0
0	0	0	0	0	0
100	1	1.074898585	0.882319038	2.959567167	2.424609104
200	2	1.705695105	1.323947379	4.726506517	3.654484886
300	3	2.329745644	1.762169449	6.497008029	4.885804872
400	4	2.95080326	2.200724975	8.281624272	6.129109076
500	5	3.612601653	2.684166295	10.20861985	7.512649452
1000	10	6.661961589	4.88696852	19.44064494	13.99480113
2000	20	11.98655817	8.708015455	37.09477204	25.98087401
3000	30	16.24903368	11.6245421	52.84512456	35.82707817
4000	40	19.8202527	13.95028373	67.33048114	44.15712726
5000	50	22.75655957	15.67931148	80.24393342	50.64773842
6000	60	25.18516677	16.89831472	91.69049822	55.38609888
7000	70	27.43361366	17.96638955	102.9709538	59.65353706
8000	80	29.26009863	18.54346462	112.6622835	62.00577778
9000	90	30.78243737	18.7330062	121.1306132	62.7856646
10000	100	32.23522069	18.8233154	129.56683	63.15853141

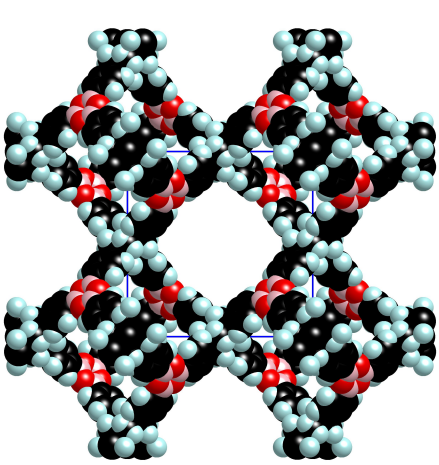

(a) COF300 structure in 001 plane

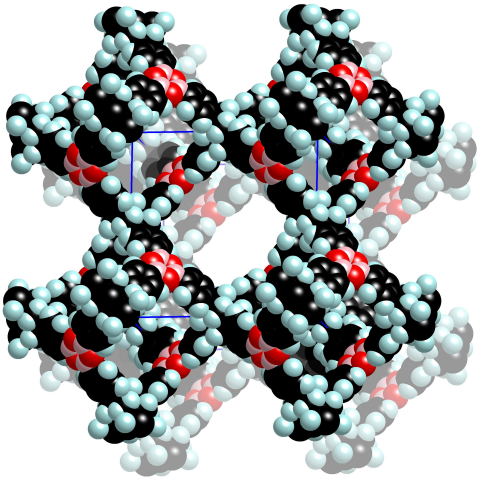

(b) COF300 structure in perspective

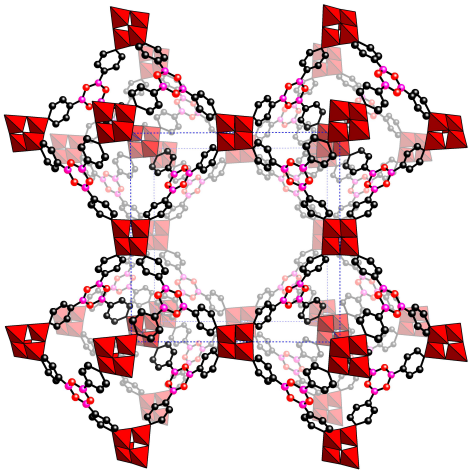

(c) COF300 with polyhedra

Figure 5.35: Structure of COF300 with different perspectives

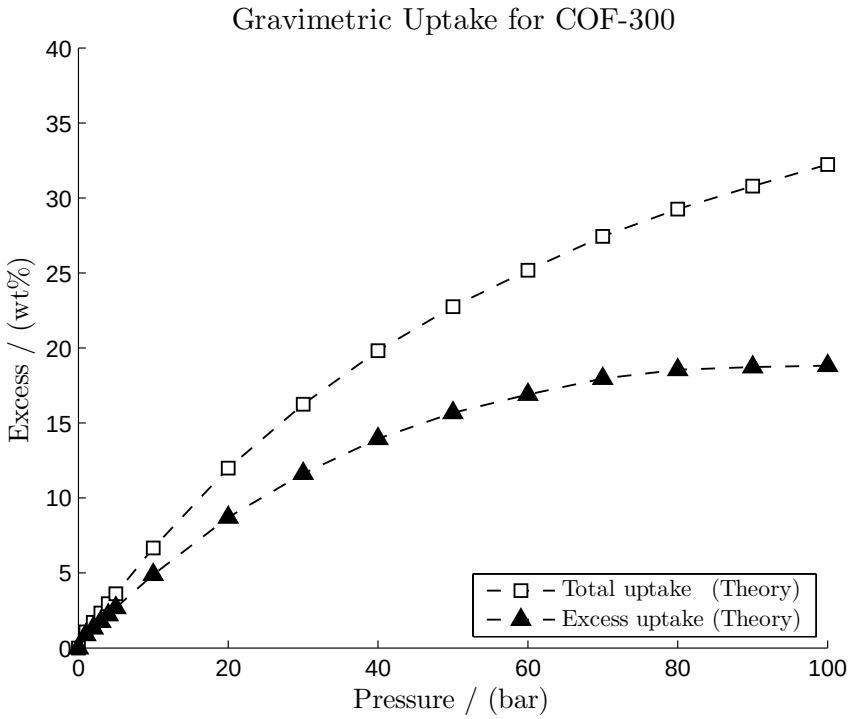

(a) Gravimetric uptake for COF-300

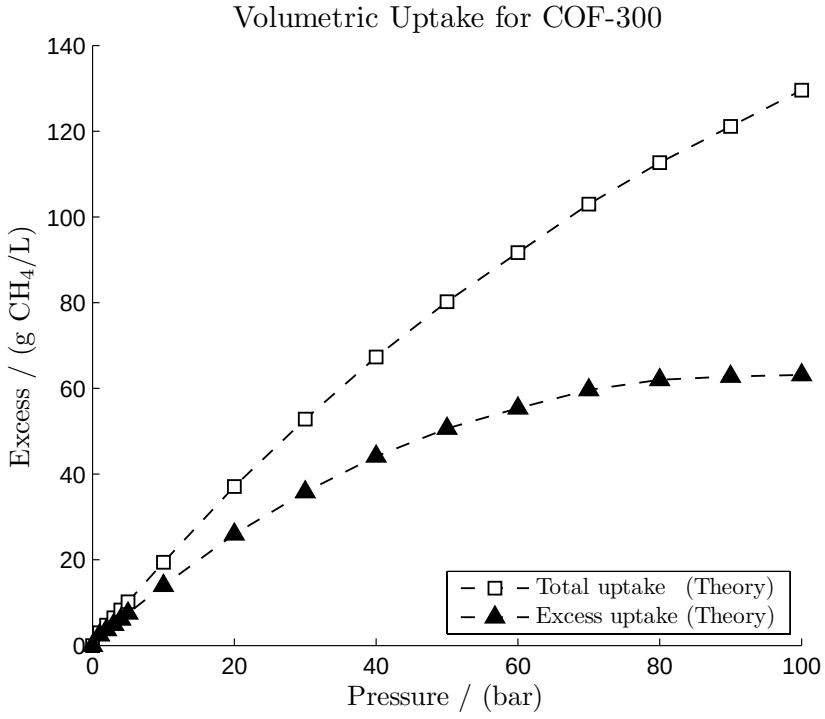

(b) Volumetric uptake for COF-300

Figure 5.36: Theoretical results for COF-300

Table 5.18: Qst values obtained from theory for COF-300

Pressure /(bar)	Qst /(Kcal/mol)	Qst /(KJ/mol)
1	1.94803	8.15056
2	1.94640	8.14374
3	1.95317	8.17206
4	1.95445	8.17742
5	1.95948	8.19846
10	1.96388	8.21687
20	1.97861	8.27850
30	1.99547	8.34905
40	2.00670	8.39603
50	2.01889	8.44704
60	2.02741	8.48268
70	2.03997	8.53523
80	2.05080	8.58055
90	2.05820	8.61151
100	2.06014	8.61963

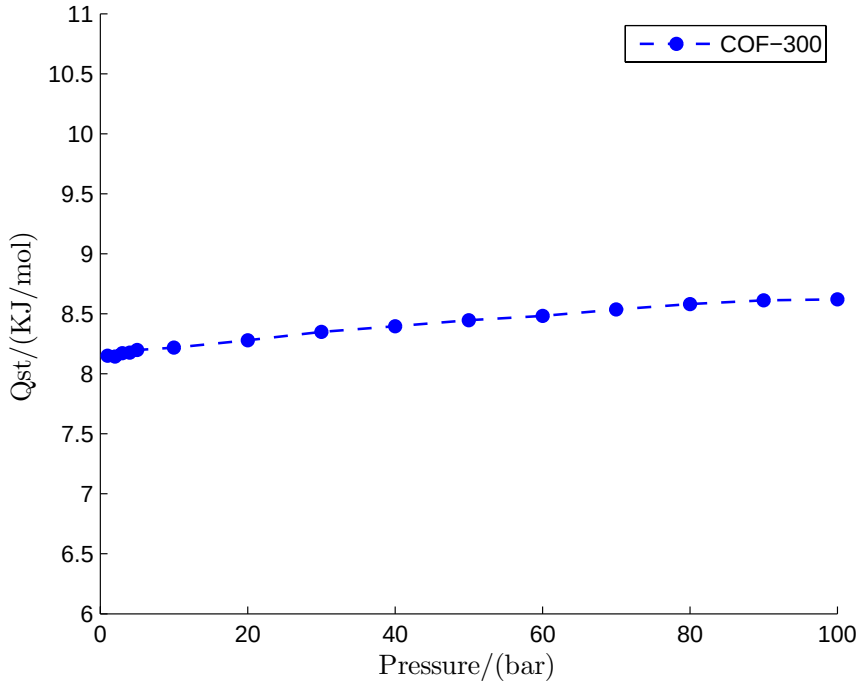

Figure 5.37: Qst values obtained from theory for COF-300

Chapter 6

Conclusions

A successful coupling of Quantum Mechanics and Statistical Mechanics has been achieved. This method has been applied to a new class of materials called Covalent Organic Frameworks. Our predictions are in complete agreement with experimental data. Hypothetical frameworks were built looking with the optimal pore size to store methane at room temperature that reaches the United States Department of Energy goal which is 180 v/v [34]. This methodology was applied to COF: 1, 5, 6, 8, 10, 102, 103, 105, 108 and 300. COF-103 and COF-105 were synthesized by the author of this thesis in the laboratory of Professor Omar Yaghi at UCLA. COF-300 is a hypothetical structure experimentally realizable and their sorption properties for methane were predicted. This method allows to test in theory any structure that it would be possible to realize, thus saving a lot of resources like time and funds when the objective it is to synthesis an structure for an optimal uptake. With this approach sorption steps were obtained so preferable sites were found.

The final goal was to test our first principles methodology against experiments. Sorption experiments were performed at low ($\leq$1bar) and high (1-80bar) pressure. The agreement with experiments is exceptionally good, when compared to optimal synthesized COF-5 and COF-8. With this comparison the method was validated. Gravimetric uptake experiments were performed in UCLA while the theoretical study was executed CALTECH. Theoretical uptake results of all studied COFs are shown in Figure 6.1(Gravimetric) and Figure 6.2 (Volumetric).

In gravimetric units the best total uptake at 100 bar is COF-105, after this COF-103, COF-108, COF-102, COF-300. 3D-COFs have the best performance with this condition. 2D-COFs are below with almost the same total uptake in the following order: COF-10, COF-5, COF-6, COF-1 and finally COF-8. This tendency has a strong correlation with pore diameter and surface area. Table 6.1 shows this trend. In these units 3D-COFs have the highest surface area and the highest gravimetric uptake; they also contain the highest pore volume for this group of materials.

However Qst values are important to reach the highest uptake value at the lowest

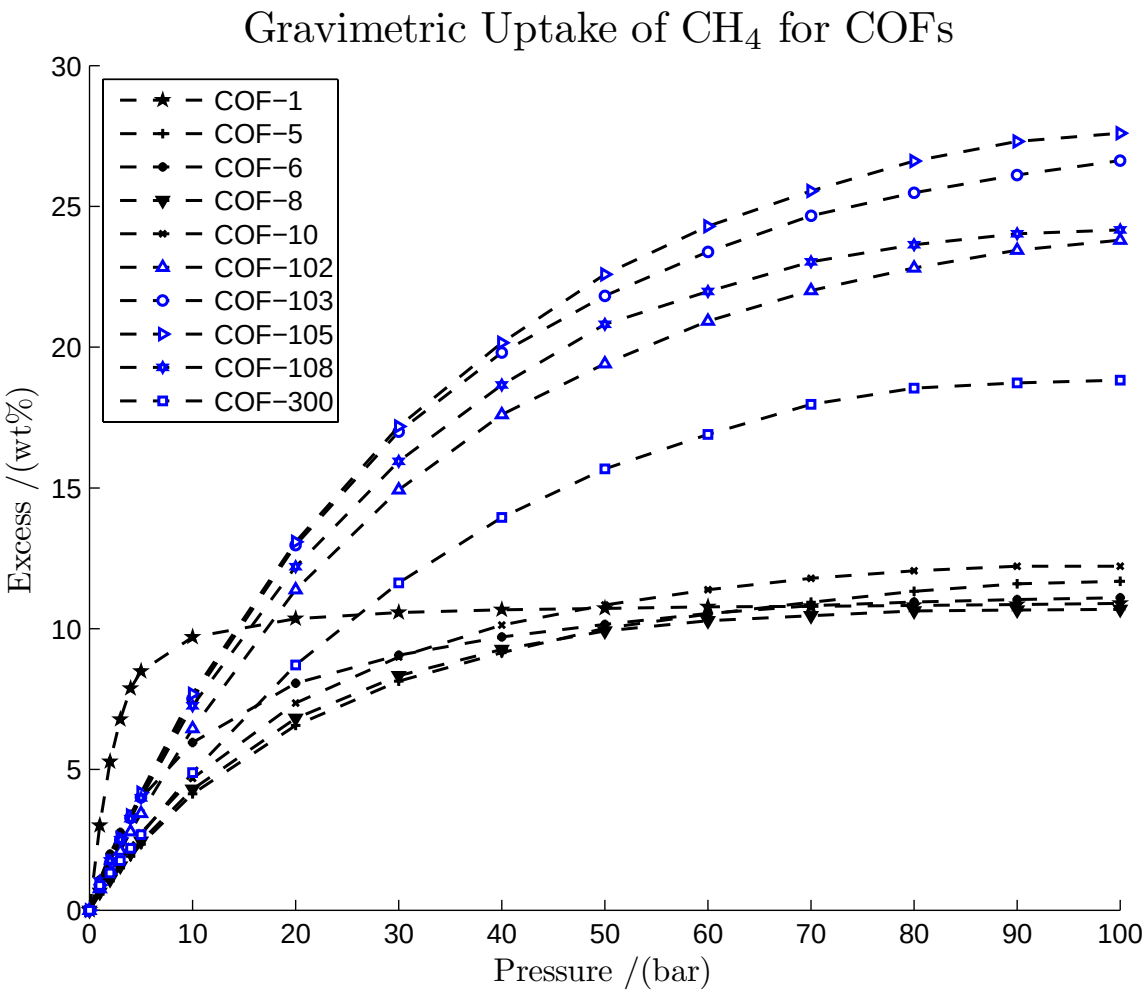

Figure 6.1: Gravimetric uptake for all studied COFs

pressure. This happens with COF-1, where the so high Qst (See Figure 6.3) makes to reach saturation at very low pressure (10 bar). It turns out that this makes COF-1 is a material that can reach DOE target in volumetric units. Even tough in volumetric units COF-103 is the best at 100 bar, COF-1 reaches its highest value at 10 bar. In volumetric unit something interesting happens, while COF-103 and COF-102 have the best values at 100 bar they do not have a good uptake at lower pressure while COF-1 and COF-8 does. This makes impractical 3D-COFs because machines usually work at most at 80 bar.

More studies are needed to find the perfect material for methane storage but some very important insights have been found: High Qst values are important; the pore diameter should be not more than 20 Å and density should not be so low as COF-108. Therefore materials were designed with the reticular chemistry approach to increase the values of affinity changing the chemical parameters. COF-28 and COF-350 are new hypothetical frameworks where the chemistry of the triangular building blocks has been changed. Since in this study it was found that Silica increase Qst slightly

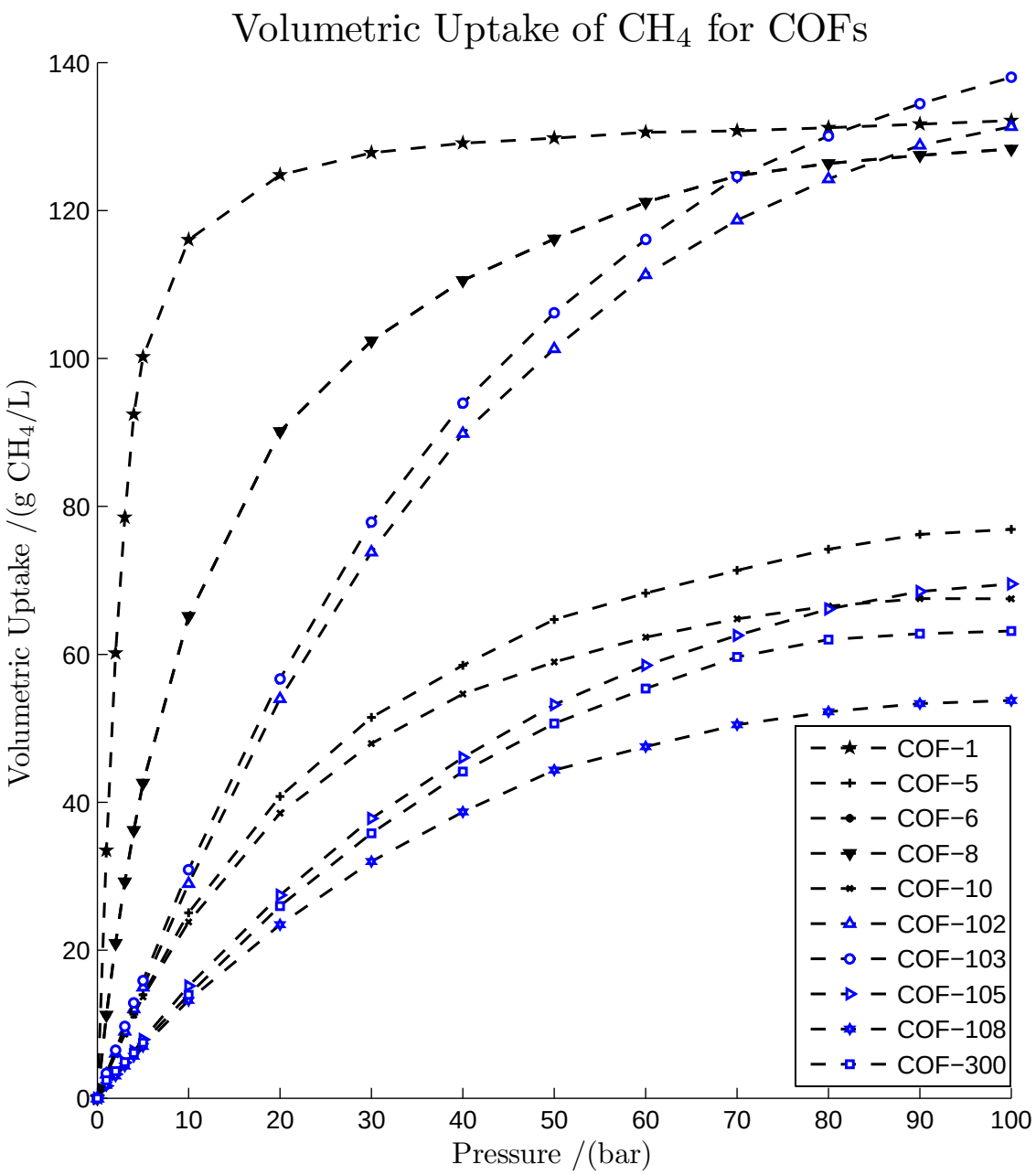

Figure 6.2: Volumetric uptake for all studied COFs

(i.e. COF-103 have better Qst than COF-102) these materials increase the number of Si atoms in the structure. COF-28 is proposed to have a **bnn** topology and hence a member of 2D-COFs (See Figure 6.4 and Figure 6.5). COF-350 is proposed to have a **ctn** topology and thus a member of 3D-COFs (See Figure 6.6 and Figure 6.7). These assumptions are based on that these topologies are the most probable to form since most of 2D-COFs synthesized so far have this structure and the same applies to synthesized 3D-COFs.

Table 6.1: General data for COFs

Material	Uptake at 30bar / (v (STP)/v)	SA / (m^2/g)	Vp / (cm^3/g)
COF-1	195.83	1229.98	0.07
COF-5	78.89	1681.99	0.86
COF-6	156.88	1052.70	0.20
COF-8	99.24	1540.37	0.54
COF-10	73.46	1828.24	1.21
COF-102	113.14	4941.48	1.03
COF-103	118.69	5231.65	1.03
COF-105	57.66	5565.94	1.05
COF-108	48.77	6280.85	4.50
COF-300	54.60	5165.94	4.15

In summary a method for designing new materials is proposed where quantum mechanics, statistical mechanics, reticular chemistry and sorption theory is used. For designing the solid state materials based on light elements, reticular chemistry was used to model the compound based on symmetry and probability arguments. Interactions parameters between the gas and framework were obtained from first principle quantum mechanics. These parameters were placed into a force field to reach thousand of atoms and statistical mechanics was used trough implementation of Grand Canonical Monte Carlo algorithm to find gas sorption sites and uptake. The atomistic approach of this model allows to the researcher figure out how the pores are been filled. From these insights pore volume filling was observed. This opens a broad range of new possibility of designing new materials making used of the versatility of organic chemistry construction of building blocks and testing the viability of these materials for storage.

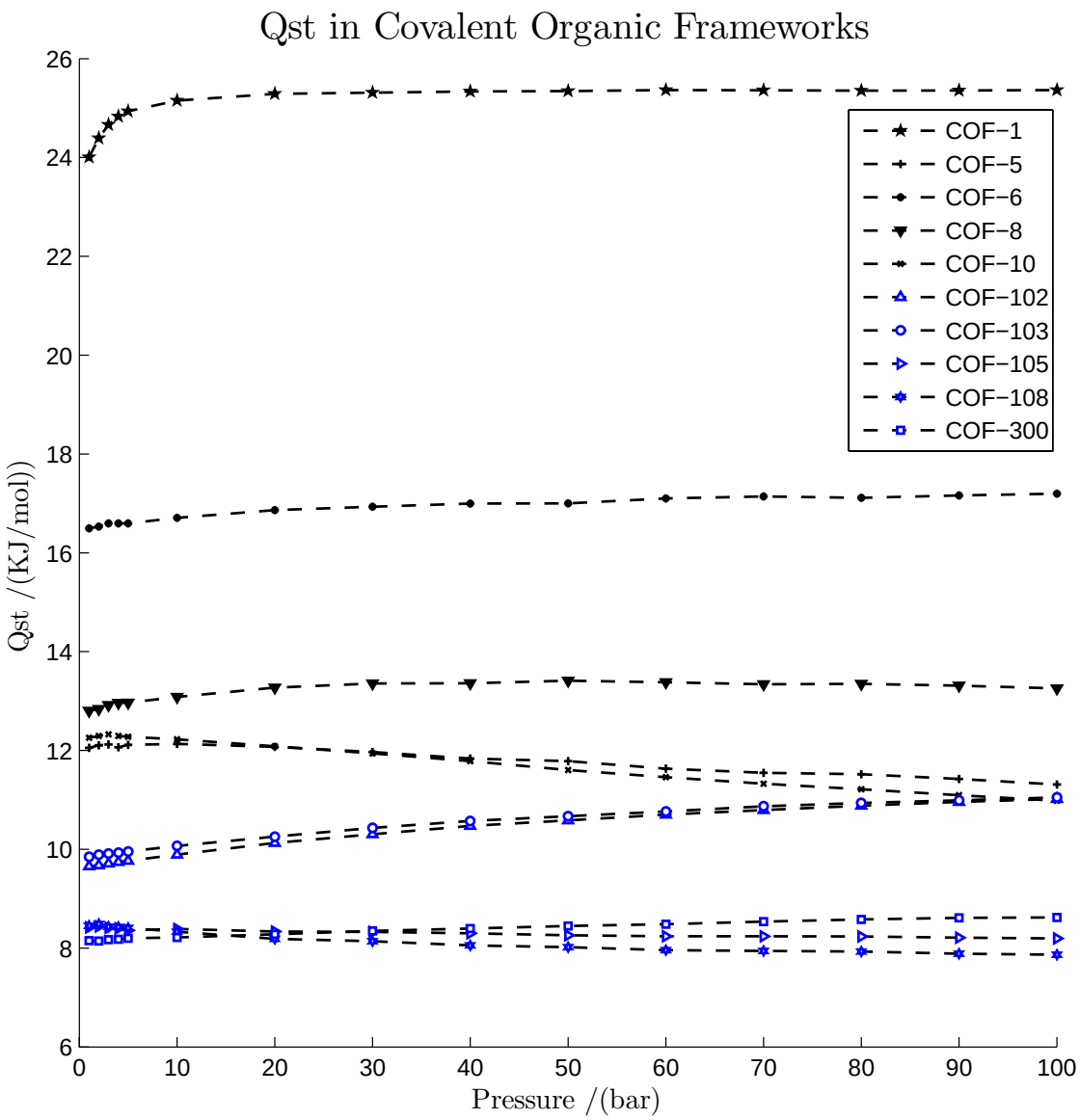

Figure 6.3: Qst values for all studied COFs

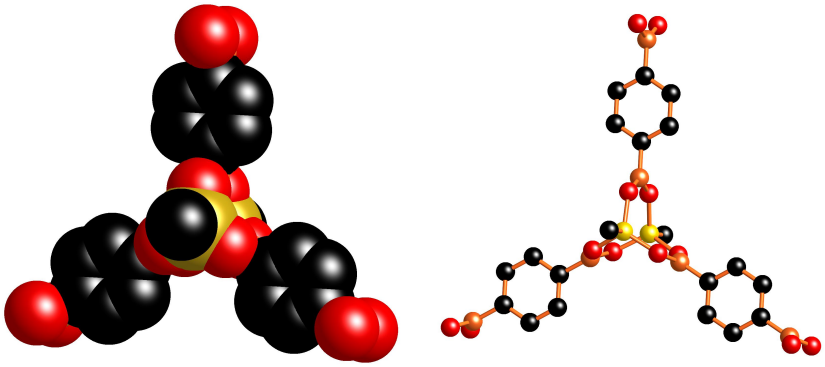

(a) SBU for COF-28 (b) SBU for COF-28/space filling

Figure 6.4: SBU for COF-28. Hydrogen atoms are not shown

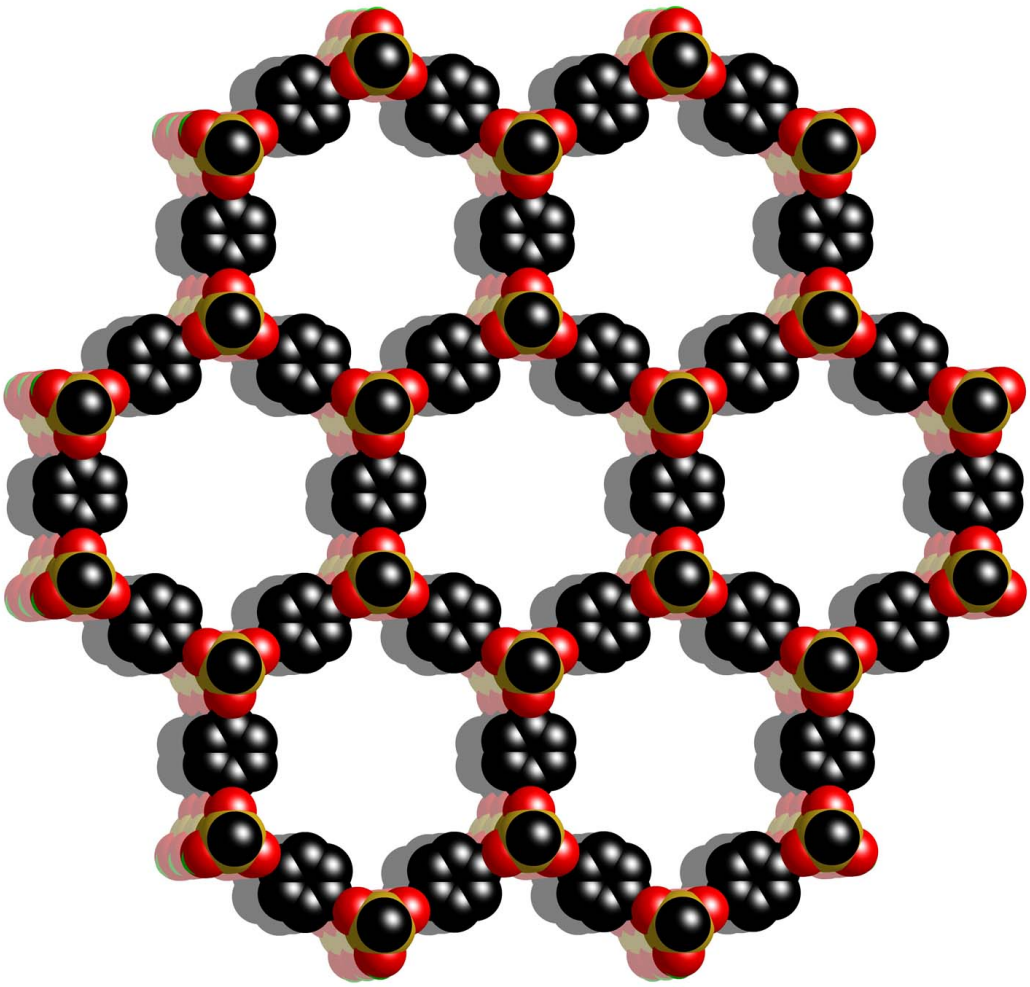

Figure 6.5: Design of COF-28. H atoms are not shown

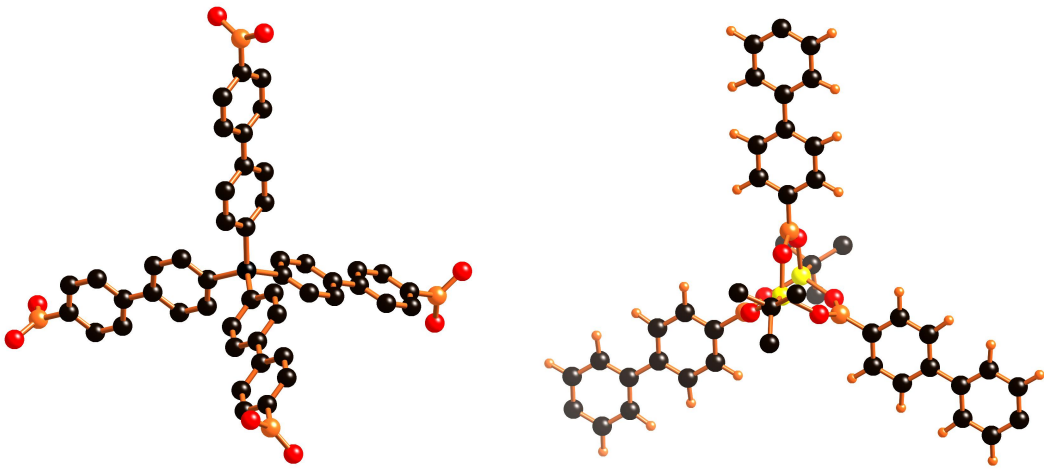

(a) Tetrahedral SBU for COF-350 (b) Triangular SBU for COF-350

Figure 6.6: Building blocks for COF-350

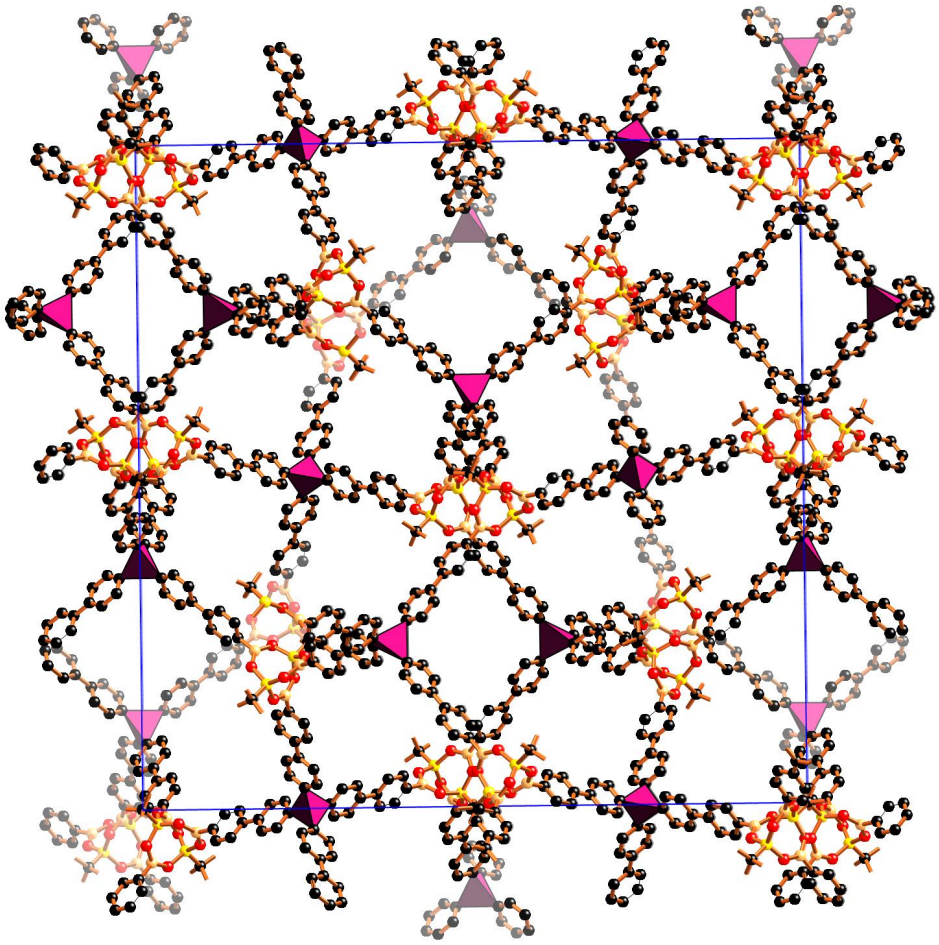

Figure 6.7: Design of COF-350

Appendix A

Developed FF from QM

```
PREFERENCES
 BONDS                                T
 ANGLES                               T
 COULOMB                              T
 INVERSIONS                           T
 TORSIONS                             T
 UREY_BRADLEY                         F
 STRETCH_STRETCH                      F
 SEPARATED_STRETCH_STRETCH            F
 STRETCH_BEND_STRETCH                 F
 BEND_BEND                            F
 TORSION_STRETCH                      F
 TORSION_BEND_BEND                    F
 BEND_TORSION_BEND                    F
 STRETCH_TORSION_STRETCH              F
 HYDROGEN_BONDS                       F
 DIAGONAL_VAN_DER_WAALS               T
 OFF_DIAGONAL_VAN_DER_WAALS           T
 GENERATE_UNDEFINED_TERMS             F
 IGNORE_UNDEFINED_TERMS               T
 NON-BONDED_3-BODY                    F
 SHRINK_CH_BONDS                      F
 SHRINK_CH_H_ATOM                     H__C
 SHRINK_CH_FACTOR                        0.91500
 SINGLE_TORSION                       F
 SCALE_TORSIONS_ABOUT_COMMON_BOND     T
 SCALE_BY_N_DEFINED_TORSIONS          T
 EXOCYCLIC_TORSIONS_SCALE_FACTOR         0.40000
 SINGLE_INVERSION                     F
```

```
H-BOND_METHOD                    SPLINE
H-BOND_LIST                      T
H-BOND_DIRECT_RCUT                  4.00000
H-BOND_SPLINE_DISTANCE_ON           4.00000
H-BOND_SPLINE_DISTANCE_OFF          4.50000
H-BOND_SPLINE_ANGLE_ON             65.00000
H-BOND_SPLINE_ANGLE_OFF            75.00000
H-BOND_LIST_DISTANCE_OFF            6.50000
H-BOND_LIST_ANGLE_OFF              90.00000
NON_BOND_LIST                    T
NON_BOND_BUFFER_DISTANCE            2.00000
H-BOND_BUFFER_DISTANCE              2.00000
COU_DIELETRIC_CONSTANT              1.00000
COU_INTER_CUT_OFF                 100.00000
COU_SPLINE_OFF                     10.00000
COU_SPLINE_ON                       8.00000
EWALD_SUM_COU_ACCURACY              0.01000
EWALD_SUM_COU_ETA                   2.50000
EWALD_SUM_COU_KCUT                  0.50000
EWALD_SUM_COU_RCUT                  6.00000
EWALD_SUM_COU_AUTO_OPT           F
COU_EXCLUDE_1-2                  T
COU_EXCLUDE_1-3                  T
COU_EXCLUDE_1-4                  F
COU_1-4_SCALE_FACTOR                1.00000
COU_METHOD                       DIRECT
COU_DIRECT_CUT-OFF                  8.00000
VDW_COMBINATION_RULE             GEOMETRIC
VDW_INTER_CUT_OFF                 100.00000
VDW_EXCLUDE_1-2                  T
VDW_EXCLUDE_1-3                  T
VDW_EXCLUDE_1-4                  F
VDW_1-4_SCALE_FACTOR                1.00000
VDW_METHOD                       SPLINE
VDW_SPLINE_ON                       8.00000
VDW_SPLINE_OFF                     10.00000
EWALD_SUM_VDW_AUTO_OPT           F
EWALD_SUM_VDW_ACCURACY              0.01000
EWALD_SUM_VDW_ETA                   2.90000
EWALD_SUM_VDW_KCUT                  0.35000
EWALD_SUM_VDW_RCUT                  6.60000
EWALD_SUM_VDW_REP_CUT               5.24000
FAST_EWALD_SUM_RATIO               10.00000
SLOW_EWALD_SUM_RATIO                5.00000
MINIMUM_IMAGE                    F
```

```
 ASSIGN_MASS                              T
 ASSIGN_CHARGE                            F
 ASSIGN_HYBRIDIZATION                     T
 ATOM_TYPE                                T
 ATOM_TYPE_ALL                            T
 CALCULATE_BOND_ORDER                     F
END
#
ATOMTYPES
 H___A      H       1.00800  0.0000   0   0   0
 H_         H       1.00800  0.0000   0   0   0
 H___3      H       1.00800  0.0000   0   0   0
 C_R        C      12.01100  0.0000   3   0   0
 C_3        C      12.01100  0.0000   4   0   0
 C_2        C      12.01100  0.0000   2   0   0
 O_3        O      15.99940  0.0000   3   0   2
 Li_        Li      6.94100  0.0000   0   0   0
 O_2        O      15.99940  0.0000   2   0   0
 Na         Na     22.98977  0.0000   0   0   0
 Si         Si     28.08550  0.0000   3   0   0
 K_         K      39.94800  1.0000   0   0   0
 Zn_        Zn     65.37700  0.0000   3   0   0
 Mg_        Mg     24.30500  0.0000   3   0   0
 Be_        Be      9.01200  0.0000   3   0   0
 B_         B      10.81000  0.0000   3   0   0
 Si         Si     28.08600  0.0000   3   0   0
 XX         XX      0.00000  0.0000   0   0   0
END
#
DIAGONAL_VDW
 O_3    VDW_MORSE  3.404600000  0.047850000    12.908700
 Zn_    VDW_MORSE  2.763000000  0.006200000    12.098300
 Mg_    VDW_MORSE  3.021000000  0.004520000    12.098300
 Be_    VDW_MORSE  2.745000000  0.000425000    12.098300
 O_2    VDW_MORSE  3.404600000  0.047850000    10.815000
 C_R    VDW_MORSE  3.898300000  0.047550000    12.615200
 H_     VDW_MORSE  3.195000000  0.007600000    10.812500
 H___A  VDW_MORSE  3.569800000  0.18145E-01    10.709400
 C_3    VDW_MORSE  3.922951000  0.076723947    12.691296
 H___3  VDW_MORSE  3.126601000  0.003205479    11.425494
 Na     IGNORE     0.000000000
 Si     IGNORE     0.000000000
END
#
ATOM_TYPING_RULES
```

```
 H_              H             0           0           1           1
                 C             2           0           0           1
 H_              H             0           0           1           1
                 B             0           0           0           1
 H_              H             0           0           1           1
                 Si            0           0           0           1
 H___3           H             0           0           1           1
                 C             3           0           0           1
 H___A           H             0           0           0           1
 C_R             C             2           0           1           1
                 **            2           0           2           1
                 **            2           0           0           1
                 **            2           0           0           1
 C_R             C             2           0           1           1
                 **            2           0           2           1
                 **            2           0           0           1
                 O             3           0           0           1
 C_R             C             2           0           2           1
                 **            2           0           0           1
                 **            2           0           0           1
 C_R             C             2           0           2           1
                 **            2           0           0           1
                 O             3           0           0           1
 C_3             C             3           0           0           1
END
#
BOND_STRETCH
 H___A H___A       HARMONIC     700.0000    0.6500
 C_R   H_          HARMONIC     700.0000    1.0200
 C_R   H___A       HARMONIC     700.0000    1.0200
 C_R   C_R         HARMONIC    1050.0000    1.3941
 C_R   O_3         HARMONIC     700.0000    1.4200
 C_R   O_2         HARMONIC     700.0000    1.4200
 C_3   C_3         HARMONIC     700.0000    1.5300
 C_3   O_3         HARMONIC     700.0000    1.4200
 C_3   H_          HARMONIC     700.0000    1.0900
 C_3   H___A       HARMONIC     700.0000    1.0900
 O_3   H_          HARMONIC     700.0000    0.9800
 O_2   H_          HARMONIC     700.0000    0.9800
 Zn_   O_3         HARMONIC     700.0000    1.9800
 Zn_   O_2         HARMONIC     700.0000    1.9800
END
#
```

```
ANGLE_BEND
 X    C_R      X    THETA_HARM   100.0000  120.0000
 X    C_3      X    THETA_HARM   100.0000  120.0000
 X    O_2      X    THETA_HARM   100.0000  120.0000
 X    O_3      X    THETA_HARM   100.0000  120.0000
 X    Zn_      X    THETA_HARM   100.0000  109.4710
 X    Mg_      X    THETA_HARM   100.0000  109.4710
 X    Be_      X    THETA_HARM   100.0000  109.4710
END
#
TORSIONS
 X    C_R      C_R      X  DIHEDRAL   25.0000    2.0000    1.0000
 X    O_3      C_R      X  DIHEDRAL    2.0000    3.0000   -1.0000
 X    O_2      C_R      X  DIHEDRAL    2.0000    3.0000   -1.0000
 X    O_2      Zn_      X  DIHEDRAL    2.0000    3.0000   -1.0000
END
#
INVERSIONS
 C_3  X        X        X  UMBRELLA   40.0000    0.0000
 C_R  X        X        X  UMBRELLA   40.0000    0.0000
 O_2  X        X        X  UMBRELLA   40.0000    0.0000
 O_3  X        X        X  UMBRELLA   40.0000    0.0000
END
#
OFF_DIAGONAL_VDW
 C_R  H___A   VDW_MORSE   3.120217000  0.100820000  12.00624600
 C_3  H___A   VDW_MORSE   3.024012000  0.052385600  14.90624600
 H_   H___A   VDW_MORSE   3.247217000  0.000868560  12.00624600
 O_2  H___A   VDW_MORSE   3.322487663  0.025153000  12.00187627
 O_3  H___A   VDW_MORSE   3.322487663  0.025153000  12.00187627
 B_   H___A   VDW_MORSE   3.493000000  0.048254000  10.56517559
 Si   H___A   VDW_MORSE   3.533500000  0.110138151  14.16508944
 C_3  H___3   VDW_MORSE   3.459219000  0.052117860  11.01981950
 C_R  C_3     VDW_MORSE   4.228357000  0.049834821  13.24926913
 H_   C_3     VDW_MORSE   3.250381000  0.000876318  12.01303763
 C_R  H___3   VDW_MORSE   3.083422000  0.114405621   9.07362292
 H_   H___3   VDW_MORSE   3.262296000  0.000876318  12.04534942
 B_   C_3     VDW_MORSE   4.112998000  0.046514037  12.28580471
 O_3  C_3     VDW_MORSE   3.593962000  0.048243612  11.26447603
 B_   H___3   VDW_MORSE   3.278983000  0.091736658  11.71867865
 O_3  H___3   VDW_MORSE   2.548639000  0.092128695   8.99321932
 Si   H___3   VDW_MORSE   4.061326000  0.132554628   7.15680369
 Si   C_3     VDW_MORSE   4.882844000  0.085740798  15.13490233
END
#
```

```
COULOMBIC
 X        X           LIN-R-EPS
END
```

Appendix B

Sorption Theory

B.1 BET surface area

The Brunauer-Emmett-Teller (BET) method [35] is the most widely used procedure for the determination of the surface area of solid materials and involves the use of the BET equation B.1. in which W is the weight of gas adsorbed at a relative pressure, P/P_0, and W_m is the weight of adsorbate constituting a monolayer of surface coverage. The term C, the BET constant, is related to the energy of adsorption in the first adsorbed layer and consequently its value is an indication of the magnitude of the adsorbent/adsorbate interactions.

$$\frac{1}{W((P_0/P)-1)} = \frac{1}{W_m C} + \frac{C-1}{W_m C}\left(\frac{P}{P_0}\right) \tag{B.1}$$

The standard multipoint BET procedure requires a minimum of three points in the appropriate relative pressure range. The weight of a monolayer of adsorbate W_m can then be obtained from the slope s and intercept I of the BET plot [36]. From equation B.1:

$$s = \frac{C-1}{W_m C} \tag{B.2}$$

$$i = \frac{1}{W_m C} \tag{B.3}$$

Thus, the weight of a monolayer W_m can be obtained by combining equations B.2 and B.3.

$$W_m = \frac{1}{s+i} \tag{B.4}$$

The second step in the application of the BET method is the calculation of the surface area. This requires knowledge of the molecular cross–sectional area A_{cs} of the adsorbate molecule. The total surface area S_t of the sample can be expressed as:

$$S_t = \frac{W_m N A_{cs}}{M} \tag{B.5}$$

where N is Avogadro's number ($6.023\text{x}10^{23}$ molecules/mol) and M is the molecular weight of the adsorbate. Nitrogen is the most widely used gas for surface area determinations since it exhibits intermediate values for the C constant (50-250) on most solid surfaces, precluding either localized adsorption or behavior as a two dimensional gas. Since it has been established [37] that the C constant influences the value of the cross–sectional area of an adsorbate, the acceptable range of C constants for nitrogen makes it possible to calculate its cross–sectional area from its bulk liquid properties. For the hexagonal close–packed nitrogen monolayer at 77 K, the cross–sectional area A_{cs} for nitrogen is 16.2 Å^2.

$$S = \frac{S_t}{m} \tag{B.6}$$

B.2 Langmuir surface area

In the absence of meso and/or macropores, a sample containing micropores will exhibit a Type I or Langmuir isotherm. The Langmuir equation B.7 is a limiting case of the BET equation for the adsorption of a single molecular layer of adsorbate [36].

$$\frac{W}{W_m} = \frac{C\frac{P}{P_0}}{1 + C\frac{P}{P_0}} \tag{B.7}$$

W and W_m are the weight of adsorbate at some P/P_0 and the weight in a monolayer, respectively. C is a constant associated with the energy of adsorption.

B.3 Dubinin-Radushkevich (DR) method

Based on the Polanyi potential theory of adsorption [38] Dubinin and Radushkevich [39] postulated that the fraction of the adsorption volume V occupied by liquid

adsorbate at various adsorption potentials ϵ can be expressed as a Gaussian function:

$$V = V_0 \exp\left[-\left(\frac{A}{\beta E_0}\right)^2\right] \tag{B.8}$$

where A is the free energy of adsorption which in the early Dubinin's works was called adsorption potential ϵ

$$A = \epsilon = RT \ln \frac{P_0}{P} \tag{B.9}$$

In equation B.8 V_0 represents micropore volume, E_0 is the so-called characteristic energy of adsorption and β is the affinity coefficient which can be approximated [40] by a ratio of the liquid molar volumes v of a given adsorbate and benzene used as the reference liquid:

$$\beta = \frac{v}{v_{\text{benzene}}} \tag{B.10}$$

Equation B.8 can be written in the following linear form:

$$\log V = \log V - 2.303 \left[\frac{RT}{\beta E_0}\right]^2 \log\left[\frac{P_0}{P}\right]^2 \tag{B.11}$$

which shows that micropore volume V_0 and E_0 parameter can be calculated from the linear fit of the isotherm data plotted as $\log(V)$ vs. $[\log(P_0/P)]^2$. Intercept of the fitted straight line gives $\log(V_0)$ while its slope m can be used to calculate E_0

$$E_0 = \sqrt{\frac{2.303}{m}} \frac{RT}{\beta} \tag{B.12}$$

The linear range for these plots is usually found at relative pressures of less than 10^{-2} [36].

Bibliography

[1] Dinca, M.; Long. J. R. *J. Am. Chem. Soc.*, **129**, 11172, (2007).

[2] Seo, J. S.; Whang, D.; Lee, H.; Jun, S. I.; Oh, J.; Jeon, Y. J.; Kim, K *Nature*, **404**, 982, (2000).

[3] Hayashi, H.; Côté, A. P.; Furukawa, H.; O´Keeffe, M.; Yaghi, O. M. *Nature Materials*, **6**, 501, (2007).

[4] Schumacher, K.; Ravikovitch, P. I.; Du Chesne, A.; Neimark, A. V.; Unger, K. K. *Langmuir*, **16**, 4648, (2000).

[5] Velev, O. D.; Jede, T. A.; Lobo, R. F.; Lenhoff, A. M. *Nature*, **389**, 447, (1997).

[6] Li, H.; Eddaoudi, M.; O'Keeffe, M.; Yaghi,O. M. *Nature*, **402**, 276, (1999).

[7] Bernstein, J. *ACA Transactions*, **39**, 14, (2004).

[8] Yaghi, O. M.; O'Keeffe, Michael; Ockwig, N. W.; Chae, H. K.; Eddaoudi, M.; Kim, J. *Nature*, **423**, 705, (2003).

[9] Wong-Foy, A. G.; Matzger A. J.; Yaghi O. M. *J. Am. Chem. Soc.*, **128**, 3494, (2006).

[10] Fletcher, A. J.; Thomas, K. M.; Rosseinsky, M. J. *J. Solid State Chem.*, **178**, 2491, (2005).

[11] Davis, M. E.; Lobo, R. F. *Chem. Mater.*, **4**, 756, (1992).

[12] Corma, A. *Chem. Rev.*, **97**, 2373, (1997).

[13] Hunter, C. A.; Sanders, J. K. M. *J. Am. Chem. Soc.*, **112**, 5525, (1990).

[14] Côté, A. P.;Benin, A. I.; Ockwig, N. W.;O'Keeffe, M.; Matzger, A. J.; Yaghi, O. M. *Science*, **310**, 1166, (2005).

[15] Zhang, W.; Brombosz, S. M.; Mendoza, J. L.; Moore, J. S. *J. Org. Chem.*, **70**, 10198, (2005).

[16] El-Kaderi, H. M.; Hunt, J. R.; Mendoza-Cortés, J. L.; Côté, A. P.; Taylor, R. E.; O'Keeffe, M.; Yaghi, O. M. *Science*, **316**, 268, (2007).

[17] Delgado-Friedrichs,O. ;O'Keeffe, M.; Yaghi, O. M. *Acta Crystallogr. A*, **62**, 350, (2006).

[18] Delgado-Friedrichs,O. ;O'Keeffe, M.; Yaghi, O. M. *Acta Crystallogr. A*, **59**, 22, (2003).

[19] Côté, A. P.;El-Kaderi, H. M.; Furukawa, H.;Hunt, J. R.; Yaghi, O. M. *J. Am. Chem. Soc.*, **129**, 12914, (2007).

[20] a) Boys, S. F.; Bernardi, F. *Mol. Phys.*, **19**, 553, (1970); b) Meunier, A.; Levy, B.; Berthier, G. *Theor. Chim. Acta*, **29**, 49, (1973); c) Jansen, H. B.; Ross, P. *Chem. Phys. Lett.*, **3**, 40, (1969).

[21] Simon, S.; Duran, M.; Dannenberg, J. J., *J. Chem. Phys.*, **105**, 11024, (1996).

[22] Morse, P. M. *Phys. Rev.*, **34**, 57, (1929).

[23] Hättig, C. *Phys. Chem. Chem. Phys.*, **7**, 59, (2005).

[24] Ahlrichs, R.; Bär, M.; Häser, M.; Horn, H.; Kölmel, C. *Chem. Phys. Lett.*, **162**, 165,(1989).

[25] Weigend, F.; Häser, M. *Theor. Chem. Acc.*, **97**, 331, (1997).

[26] Weigend, F.; Häser, M.; Patzelt, H.; Ahlrichs, R. *Chem. Phys. Letters*, **294**, 143, (1998).

[27] Adams, D. J. *Mol. Phys.*, **28**, 5, (1974).

[28] Soto, J. L. "Statistical Thermodynamics of Sorption in Molecular Sieves". *PhD Thesis, University of Pennsylvania*, (1979).

[29] Mayo, S. L.; Olafson, B. D.; Goddard III, W. A. *J. Phys. Chem.*, **94**, 8897, (1990).

[30] National Institute of Standards and Technology "Thermophysical Properties of Fluid Systems" *NIST Standard Reference Database*, (2005).

[31] Roswell, J.; Yaghi, O. M.*J. Am. Chem. Soc.*, **128**, 1304, (2006).

[32] Tilford, W. R.; Gemmil, W. R.; zur Loye, H.-C.; Lavigne, J. J.*Chem. Mater.*, **18**, 5296, (2006).

[33] Cerius^2 Modeling Environment, version 4.2, Molecular Simulations Incorporated, San Diego, CA (1999).

[34] Wang, X.-S.; Ma, S.; Rauch, K.; Simmons, J. M.; Yuan, D.; Wang, X.; Yildirim, T.; Cole, W. C.; López, J. J.; de Meijere, A.; Zhou, H.-C. *Chem. Mater.*, **20**, 3145, (2000).

[35] Brunauer,S.; Emmett, P.; Teller, E. *J. Amer. Chem. Soc.*, **60**, 309, (1938).

[36] OPERATING MANUAL, Quantachrome Instruments, P/N 05061 Rev G (2006).

[37] Lowell, S.; Shields, J.; Charalambous, G.; Manzione, J. *J. Colloid Interface Sci.*, **86**, 191, (1982).

[38] Polanyi, M. *Verh. Dtsch. Phys. Ges.*, **16**, 1012, (1914).

[39] Dubinin, M.M.; Radushkevich, L.V. *Dokl. Akad. Nauk. SSSR*, **55**, 331, (1947).

[40] Dubinin, M.M. "Chemistry and Physics of Carbon", **2**, 51, P. L. Walker (Ed.), Marcel Dekker, New York (1966).